UNIVERSITY OF OKLAHOMA

GRADUATE COLLEGE

SEISMIC ATTRIBUTE ANALYSIS OF UNCONVENTIONAL RESERVOIRS, AND STRATIGRAPHIC PATTERNS

A DISSERTATION

SUBMITTED TO THE GRADUATE FACULTY

in partial fulfillment of the requirements for the

Degree of

DOCTOR OF PHILOSOPHY

By

KUI ZHANG
Norman, Oklahoma
2010

SEISMIC ATTRIBUTE ANALYSIS OF UNCONVENTIONAL RESERVOIRS, AND STRATIGRAPHIC PATTERNS

A DISSERTATION APPROVED FOR THE
CONOCOPHILLIPS SCHOOL OF GEOLOGY AND GEOPHYSICS

BY

Dr. Kurt J. Marfurt, Chair

Dr. Roger M. Slatt

Dr. Heloise B. Lynn

Dr. Larry Grillot

Dr. Katie Keranen

Dr. Deepak Devegowda

Acknowledgements

The completion of this work would not be possible without the help, support, patient guidance, and continuous input of my principal supervisor, Kurt Marfurt. Through the four years, he has tremendously enhanced the level I look at geophysics problems and his help on my life side has been even greater. It is him that always stood beside and tried his best to encourage, and support me in those stressful days.

I would like to extend my sincere gratitude to the members of my committee: Heloise Lynn, Roger Slatt, Katie Keranen, Larry Grillot, and Deepak Devegowda for their commitment to serve on my committee and their inspiring comments on my research. Thanks to Tim Kwiatkowski and Marcilio Matos for discussion of those intriguing mathematical and geophysical problems.

I also would like to acknowledge fellow students and friends in AASPI team including Bradley Wallet, Supratik Sarkar, Roderick Perez, Oswaldo Davogustto, Victor Pena, Miguel Angelo, Xavier Refunjol, Bo Zhang, Ha Mai, Malleswar Yenugu, Atish Roy, Ozan Elis, Sunday Amoyedo, Amanda Thompson and many others not listed for their great help. My sincere thanks also go to Donna Mullins, Nancy Leonard, Adrianne Fox, Teresa Hackney, and Niki Chapin who provided key help during these years.

Thanks to Devon Energy and to the industry sponsors of the University of Oklahoma Attribute-Assisted Seismic Processing and Interpretation (AASPI) Consortium for providing financial support. I also thank the Society of Exploration Geophysics and Charlie and Jean Smith foundation for offering me the scholarship during the last three consecutive years.

Finally, I am deeply indebted to my beloved one, Yanxia Guo for all her support and personal sacrifice in family. I owe her everything.

Table of Contents

List of Tables

List of Figures

Seismic azimuthal anisotropy analysis of post-hydraulic fracturing

Quantitative correlation of fluid flow to curvature lineaments

Seismic attribute illumination of an igneous reservoir in China

Extension of spectral-decomposition into mapping stratigraphic patterns

Abstracts

Seismic volumetric attributes have become one of the key components in aiding interpretation and investigation of the hydrocarbon reservoirs. These reservoirs can be either conventional or unconventional. The application of seismic attributes in conventional reservoirs with mapping bright spots, faults, and channels has been quite successful. Now we face challenges in mapping unconventional reservoirs such as shales, tight gas sands, and carbonates as well as igneous reservoir. This dissertation focuses on developing new workflows to map unconventional reservoirs in a qualitative or quantitative fashion using seismic attributes. The unconventional reservoirs under study include shales, carbonates and volcanic build-ups.

A common challenge with many unconventional reservoirs is that they have low permeability, such that fractures are critical to economic success. I apply a different workflow measuring azimuthal anisotropy in the Barnett Shale of the Fort Worth Basin after hydraulic fracturing. The resulting anisotropy is not only heterogeneous, but compartmentalized by previous (Pennsylvanian) deformation. I also develop a workflow to correlate production with proximity of the well to curvature lineaments by scanning hypothesized open fractures as a function of azimuth. I calibrate this workflow to a previously studied Mississippian limestone reservoir from Kansas prior to application to the Woodford Shale of the Arkoma Basin. My final study is a volcanic extrusive reservoir from the Songliao Basin, Northeast China. Volcanic are usually avoided, while I hope that this example may serve as an analogue for others.

As part of my analysis, I also document the extension of the previous workflow and development of new algorithm related to spectral-decomposition.

Chapter 1: Introduction

During last decade, the exploration targets in oil and gas industry have moved radically from conventional reservoirs to unconventional reservoirs with the advent of the advanced drilling and stimulation treatment techniques. These unconventional reservoirs majorly include tight gas sands, coal bed methane, gas hydrate deposits, heavy oil, tar sands, gas shales, and igneous reservoir. However, seismic attribute delineation of unconventional reservoirs remains challenging in most cases. The goal of this dissertation is to develop new workflow and attributes to map unconventional reservoirs.

This dissertation combines the work of six published SEG expanded abstracts and one submitted TLE paper with two major focuses: unconventional reservoir study and spectral decomposition illumination of stratigraphic patterns. I have developed new algorithm, as well as modified algorithm of OU's Attribute-Assisted Seismic Processing and Interpretation (AASPI) research team. These algorithms include prestack Kirchhoff time migration, prestack structure-oriented filtering, azimuthal anisotropy analysis, azimuthal intensity calculation, and statistical analysis of seismic spectra. In addition to algorithms, I developed unique seismic data processing and attribute analysis workflows. My dissertation is organized in a form of a list of scientific papers.

In Chapter 2, I present the seismic azimuthal anisotropy analysis of post-hydraulic fracturing in the Barnett Shale with the objective of recognizing the signature of gas- or water-charged fractured reservoir, and identifying any bypassed pay. I develop and apply three workflows that condition the prestack migrated gathers facilitating the evaluation of three alternative anisotropy measures: AVAz, impedance vs. azimuth, and

tuning frequency vs. azimuth. I investigate structural control of what I interpret to be induced fractures by comparing azimuthal anisotropy images to curvature maps. This Chapter is a paper to be submitted for publication in *Geophysics*.

In Chapter 3, I extend a previously-developed, interpreter intensive workflow to generate a suite of new azimuthally-limited attribute volumes based on structural curvature maps that can be directly correlated to hydrocarbon production sensitive to fracture orientation and intensity. This workflow is established by hypothesizing that production will be a function of the well's distance to "fractures" correlated with curvature. I then apply this workflow to a Mississippian carbonate reservoir in Kansas and the Woodford Shale in Oklahoma. This Chapter is also a paper to be submitted for publication in *Geophysics*.

In Chapter 4, I apply volumetric seismic attributes to an extrusive igneous reservoir in the Songliao Basin, Northeast China with the goal of evaluation of the role of amplitude-related and geometric attributes in illumination of the volcanic architectural elements. This Chapter has been submitted for publication in *The Leading Edge.*

In Chapter 5, I present the new developed statistical spectral attributes based on the non-Gaussian spectra after spectral flattening. These attributes show great potential to map channel features in two surveys acquired over the Central Basin Platform, west Texas, and the Anadarko Basin, Oklahoma. I also evaluate the sensitivity of spectral attributes to sequence stratigraphy through investigation of a suite of synthetic models, and find peak frequency and mean frequency to be potential tools allowing one to differentiate upward fining, upward coarsening, and blocky patterns. This chapter is the

combination of two SEG abstracts. The results of these algorithms are used in Chapter 2 and 4.

Each of the above Chapters is followed by the appropriate references.

Although I am the first author of these papers, I have preserved the “we” form as it will appear in publication with my coauthors.

Chapter 2: Seismic azimuthal anisotropy analysis of post-hydraulic fracturing

Kui Zhang[1], Kurt J. Marfurt[1], and Amanda M. Thompson[1,2]

[1] *University of Oklahoma, School of Geology and Geophysics,* [2]*Devon Energy*

Email: kui.zhang-1@ou.edu, kmarfurt@ou.edu, and Amanda.Thompson@dvn.com

Paper presented at the 80th Annual Society of Exploration Geophysicists International Exposition meeting in Denver, Colorado, USA

SEG Expanded Abstracts 29, 273-277 (2010)

This paper will be submitted to GEOPHYSICS journal for publication.

Chapter 2: Seismic azimuthal anisotropy analysis of post-hydraulic fracturing

Abstract

Tight sandstone, limestone, and shale reservoirs require hydraulic fracturing to provide pathways that allow hydrocarbons to reach the well bore. Most of these tight reservoirs are now produced using multiple stages of fracturing through horizontal wells drilled perpendicular to the present-day azimuth of maximum horizontal stress. In a homogeneous media, the induced fractures will propagate perpendicularly to the well, parallel to the azimuth of maximum horizontal stress, thereby efficiently fracturing the rock and draining the reservoir.

In this paper, we report the results of what may be the first anisotropy analysis of a shale-gas reservoir after extensive hydraulic fracturing. In our study area, the organic-rich Barnett Shale reservoir has been extensively hydro-fractured by high pressure fluids to stimulate production using 308 vertical or directional wells and 127 horizontal wells prior to the acquisition of the 3D seismic survey. The objective of the survey was to recognize the signature of gas- or water-charged fractured reservoir, and to identify any bypassed pay.

We migrate the seismic data into four azimuth sectors using a new azimuth binning prestack time migration, followed by residual moveout (RMO) correction, and prestack conditioning on each azimuth to provide high-quality images for subsequent fracture analysis. We find that azimuthal variation in acoustic impedance provides very similar images with amplitude vs. azimuth (AVAz). Both of these methods were less

noisy than tuning frequency as a function of azimuth (FVAz). All three methods provide greater vertical resolution within the target area than velocity vs. azimuth (VVAz).

Contrary to conventional assumptions, the measured anisotropy, and hence the inferred direction of fractures, is not parallel to the regional maximum horizontal stress direction. Furthermore, the anisotropy is highly compartmentalized, with the compartment edges being defined by ridges and domes delineated by the most positive principal curvature k_1. Microseismic work by others in the same survey indicates that these ridges contain healed natural fractures that form fracture barriers. We hypothesize that the first hydraulically fractured well modifies the local stress field, with subsequent wells in the same compartment following, or further modifying the stress field initiated by the previous wells. Mapping such heterogeneous anisotropy field could be critical in planning the location and direction of any future horizontal wells to restimulate the reservoir as production drops.

Introduction

In shale gas reservoirs, natural fractures, induced fractures, and azimuthal variation of the horizontal stress will cause azimuthal anisotropy. Seismic P-waves travelling through such media exhibit azimuthal variation in travel time, amplitude, and tuning. If these signatures are measured, valuable information related to either fractures and/or the stress field can be inferred. Knowledge of natural fracture orientation and intensity is critical for appraisal, development, and hydrocarbon production. Knowledge of induced fracture orientation and intensity can help evaluate the success of the

completion project, the possible need for restimulation, and identify by-passed pay. Undestanding the maximum stress field is helpful in the choice of drilling direction, and cost-effective completion.

The most straightforward model to describe azimuthal anisotropy consists of a set of aligned vertical cracks embedded in an isotropic, homogeneous matrix (Thomsen, 1995). This horizontal transverse isotropy (HTI) model forms the basis for almost all of the current fracture characterization workflows. Although most shale gas reservoirs are characterized by orthorhombic symmetry (flat layers and one set of vertically-aligned fractures), these workflows still work effectively.

The first azimuthal anisotropy workflow measured the variation of velocity with azimuth (VVAz). VVAz requires picking the top and bottom of the reservoir at different azimuths thereby providing measures of the elliptical behaviour of the phase velocity as seismic energy propagates along different azimuths through the fractured system. VVAz provides a robust measure of the average fracture properties of a relatively thick formation (Sicking et al., 2007; Roende et al., 2008; Jenner, 2001; Xu and Tswankin, 2007; Treadgold et al., 2008). A more recently introduced competing method is amplitude variation vs azimuth (AVAz), which is applied to phantom horizons through the offset- and azimuth-limited amplitude data volumes and provides more localized, higher-resolution information about the fractured reservoir (Rüger, 1998; Luo and Evans, 2004; Goodway et al., 2006, Xu and Tsvankin, 2007). Both techniques have advantages and disadvantages. Effective VVAz analysis requires accurately picking the far-offset seismic events from different azimuths. These large-offset events are often corrupted by noise, suffer from migration stretch, and may not be avalaible at all if the target is too

deep. Effective AVAz analysis requires a uniform, high-fold acquisition; non-uniform distribution of fold in different azimuths introduces errors such that a wise normalizaion needs to be applied.

Since velocity is azimuthally anisotropic in the presense of natural or induced fractures, acoustic impedance (AI), the product of velocity and density, will also be azimuthally anisotropic. Model-based AI inversion is tightly coupled to geology by wells, and removes most of the seismic wavelet and thin-bed tuning effects, thereby increasing vertical resolution.

Marfurt and Kirlin (2001) analyzed the Green's function response of thin beds, and noted that spectral decomposition estimation of the tuning frequency can be an effective thin-bed thickness estimator. Chapman and Liu (2004) performed a synthetic study of oriented fractures and found that tuning effects give rise to frequency dependent behavior.

The Barnett Shale is an important unconventional resource play in the Fort Worth Basin, Texas, where it serves as source rock, seal, and trap. Since it has very low permeability, Devon Energy launched a program that hydraulically fractured the rocks in the field in recent years, which was previously considered to be marginal, by injecting high pressure fluid with 10 wells per square mile, thereby significantly improving the production rates. The wide-azimuth seismic survey under our study was acquired after hydraulic fracturing, such that our focus is on mapping the orientation and intensity of induced rather than natural fractures, with the objective being the identification of reservoir compartmentalization and by-passed pay. Our paper builds on Thompson's work (2010b) on the same survey who reported that none of eight microseismic

experiments conducted in the survey area breached the overlying Marble Falls and underlying Viola Limestone fracture barriers. Anisotropy estimated using a dominant frequency method showed a rather uniform E-W trending anisotropy in both the upper and lower fracture barriers. In contrast, the anisotropy in the Lower Barnett Shale, Forestburg Limestone, and Upper Barnett Shale are highly heterogeneous, indicating fractures propagating in almost all directions. In this work, we perform a more detailed analysis of the Lower Barnett Shale, the primary exploration target, and evaluate the benefit of data conditioning and alternative anisotropy measures.

We begin our paper with data conditioning, including azimuthal binning based on midpoint to image point azimuth, RMO correction, and prestack structure-oriented filtering. Then we evaluate and compare three alternative means of estimating azimuthal anisotropy – AVAz, impedance vs. azimuth, and tuning frequency vs. azimuth all of which involve fitting sinusoids to attributes computed from azimuthally-limited volumes. Next, we investigate structural control of induced fractures by comparing our azimuthal anisotropy images to most-positive and most-negative principal curvature and Sobel-filter similarity. We conclude with a summary of our findings.

Data processing

Careful and successful data processing is a key to azimuthal anisotropic analysis, albeit challenging. The very high-fold wide azimuth land seismic survey under study was acquired in 2009 and was discussed by Thompson et al. (2010a). The early stage processing of the seismic data includes standard statics correction, coherent noise

attenuation, amplitude conditioning and deconvolution. After preprocessing, we apply three additional processes to better condition the data: azimuthal binning into four sectors internal to prestack time migration, application of residual moveout (RMO) correction on each azimuthal sector to account for vertical transverse isotropy, and prestack structure-oriented filtering to suppress noise cross-cutting reflectors of interest. These components are critical to preserving amplitude and phase amenable for the subsequent anisotropic analysis.

Azimuthal binning internal to prestack migration

Unlike conventional azimuthal sorting computing using the vector connecting surface source and receiver locations, Perez and Marfurt (2008) proposed an azimuth binning algorithm which places each migrated sample into an azimuth bin computed from the source-receiver midpoint to the image point (Figure 2-1a). This new binning method has proven to be effective in improved illumination of faults and fractures for two reasons: first, it separates the weak side-scattered component caused by fault terminations, fractures, and steep reflectors from the stronger near vertical reflections that fall within the sagittal plane, and second, it avoids mixing events with different residual moveout if azimuthal velocity anisotropy is present. We migrate the data into different azimuth and offset bins as shown in Figure 2-1b. In our study, the data were migrated into four azimuthal sectors with central azimuths of 0^o (N-S), 45^o (NE-SW), 90^o or -90^o (E-W), and 135^o or -45^o (NW-SE). Since a single migration velocity is used and velocity variation

with azimuth is ignored, the residual moveout in the CRP gathers is azimuthally variant, requiring different RMO corrections for each azimuth.

Vertical transverse isotropy correction

Recent trends in seismic aquisition of large offset data make nonhyperbolic moveout corrections indispensably in most scenarios. Effective anisotropy due to thin beds and intrinsic anisotropy associated with mineral alignment are often well-represented by a vertical transverse isotropy (VTI) model. As one of the classic VTI media, shale typically gives rise to the well-know "hockey stick" at the far offsets seen on migrated gathers (Figure 2-2a) which needs to be adressed before we search for HTI anomalies. Ignorance of VTI effects will result in image degradation or totally misleading results. Weak VTI anisotropy can be quantified by estimating the three Thomsen's parameters epsilon (ε), delta (δ), and gamma (γ). Currently, most processing shops are readily able to handle VTI anisotropy by iterative use of TI anisotropic reflection tomography and prestack depth migration. Since our dips are less than 2^o, we take the faster and more straightforward two-step flow shown in Figure 2-3. This RMO correction flow is based on the principle that, after isotropic prestack time migration, (1) the short-spread is quite flat, and (2) the large offset beyond (offset/depth > 1.0) can be fit by a fourth-order polynomial: $\Delta T=a+bx^2+cx^4$, where ΔT is residual time, and x is the offset. A representative CRP gather after residual moveout anslysis is shown in Figure 2-2b.

Prestack data conditioning

There are many ways to perform prestack data conditioning. Our approach (Figure 2-4) is similar to one described by Singleton (2009) who used the structural dip and azimuth computed from migrated, stacked data as the structural control in 3D structure-oriented filtering of each common offset and azimuth volumes. Alternative structural-oriented filters include principal component and alpha-trim mean filters. Our data conditioning method is edge-preserving smoothing, preserves the AVO signature of gathers, and enable effective signal-noise-ratio (SNR) enhancement. Figures 2-5a and 2-5b show representative CRP gathers from four different azimuths before and after two passes of edge preserving principal component structural-oriented filtering; the improvement in gather quality is readily apparent on the conditioned data. Figures 2-6a and 2-6b show representative azimuthally-limited stacks before and after conditioning along line AA'. The location of line AA' is shown in Figure 2-10. Note that some undesirable, random, uncorrelatable energy component is diminished after conditioning, even though the filters are applied in the inline/crossline domain.

Figure 2-7 portrays four representative azimuthal stacked sections AA' from 0^o, 45^o, 90^o, and 135^o respectively after the above described step-by-step processing and FX deconvolution. In addition to variation of two-way travel time and amplitude as a function of azimuth, we also note subtle change in focusing as mentioned by Roende at al. (2008).

Alternative approaches to measure anisotropy

If an otherwise homogeneous horizontal layer contains vertically aligned parallel fractures (the HTI model), seismic velocity will vary with azimuth. In addition, many other P-wave seismic attributes such as travel time, reflection amplitude, attenuation coefficient, and spectra will also exhibit azimuthal anisotropy. The azimuthal variation can be represented by a sinusoid that has a periodicity of 180^o. Our survey was acquired with anisotropy analysis in mind, with fold approximating 400 and isotropic source-receiver spider diagrams (Thompson et al., 2010a). We evaluate three commonly-used seismic attributes: acoustic impedance, AVO gradient and tuning frequency that we find are sensitive to azimuthal variation in the Barnett Shale.

Figure 2-8 describes our workflow. We start by migrating the data into azimuth-offset bins as depicted in Figure 2-1. Next, we condition the CRP gathers using structure-oriented filtering. We then compute seismic attributes (AVO gradient, impedance, and peak frquency) from each azimuthally-limited volume and flatten them along the picked horizon from the associated azimuth. Assuming azimuthal variation of a particular seismic attribute caused by a set of cracks aligned with a preferred azimuth (or alternatively, nonuniform horizontal stresses), we can represent the attribute by an ellipse. The objective function for ellipse fitting is defined as:

$$\min \quad E = \sum_{j=1}^{J} \left[(a_j - \overline{a}) - \varepsilon \cos^2(\varphi_j - \psi) \right]^2 \ , \ (1)$$

where

$$\bar{a} = \frac{1}{J}\sum_{j=1}^{J} a_j \qquad (2)$$

is the average of the attribute a_j measured along azimuth φ_j, ψ is the azimuth corresponding to the maximum attribute value, and ε is a measure of the degree of ellipticity. The confidence, c, of the elliptical fit is

$$c = 1 - \left[\frac{E}{\sum_{j=1}^{J} (a_j - \bar{a})^2 + r} \right] \quad , \qquad (3)$$

where r is a small number to avoid division by zero. Note in equation 3 that if $a_j = \bar{a}$ for all azimuths, φ_j, c=1.0, implying that we are confident that we have a locally isotropic media, with ε=0.

If the geology can be represented by HTI symmetry or orthorhombic symmetry (flat layers and one set of vertically-aligned fractures), ψ will represent the fracture strike, while ε will be a measure of the fracture intensity. This approach provides similar anisotropic measures with the one proposed by Thompson et al. (2010a).

AVAz

Rüger (1998) parameterized amplitude vs azimuth (AVAz) by expressing the HTI symmetry with the Christoffel equation. Eigenvector solution of the P-wave polarization vectors gives the reflection coefficient R_p as a function of incident angle, θ, and azimuth, φ as

$$R_p(\theta, \phi) = A + B(\varphi)\sin^2\theta + C(\varphi)\sin^2\theta\tan^2\theta. \qquad (4)$$

Equation 4 has a form similar to Shuey's (1985) equation, commonly used for isotropic AVO analysis,

$$R_p(i) = A^{iso} + B^{iso}\sin^2\theta + C^{iso}\sin^2\theta\tan^2\theta \qquad (5)$$

where, $A=A^{iso}$, $B \neq B^{iso}$, and $C \neq C^{iso}$. A and A^{iso} are normal-incident reflectivity, B *and* B^{iso} are the gradient, controlling R_p from intermediate angles (15^o-30^o), and C and C^{iso} are third order term. In Rüger's (1998) equation, $B(\varphi)$ can be expressed as:

$$B(\phi) = B^{iso} + B^{ani}\cos^2(\phi - \psi) \qquad (6)$$

where B^{iso} is Shuey's (1985) isotropic gradient, B^{ani} is the anisotropic gradient associated with fracture intensity, and ψ is the azimuth of the symmetry axis plane of the HTI media associated with fracture strike. Note that equation 6 has the same form as equation 1 and is therfore amendable to least-squares sinusoidal fitting to solve an over-determined system to find B^{ani} and ψ.

Figure 2-9 shows the AVO gradient term, B, in equation 6, computed from azimuthally-limited volumes at azimuth 0^o, 45^o, 90^o, and 135^o along line BB'. The location of line BB' is shown in Figure 2-10. We see the evident variation in AVO responses for different azimuths.

Acoustic impedance anisotropy

Since it can be directly tied to well-logs, acoustic impedance is one of the most useful seismic attributes to investigate lithology, porosity, and fluid type. In our study, we compute model-based AI from azimuthally-limited stacks obtained by stacking amplitude

from incident angle of 0^o to 35^o, and find that AI in the Barnett Shale shows strong azimuthally anisotropic behavior. The AI anisotropy based on impedance inversion reduces the impact of the seismic wavelet (each azimuthal stack needs to be tied and has its own wavelet), somewhat broadens the spectrum, and is tightly coupled to geology by wells, giving reliable internal resolution to the shales. Since each azimuthally-limited volume has its own wavelet (Appendix A), AI anisotropy compensates the azimuthal variations of fold and offset that can negatively impact AVAz analysis.

Figure 2-10 shows the picked time structure maps of the Ordovician unconformity about (a) 0^o, (b) 45^o, (c) 90^o, and (d) 135^o. Figure 2-11 shows the acoustic impedance 10 ms above the Ordovician unconformity computed from azimuthally-limited sectors about (a) 0^o, (b) 45^o, (c) 90^o, and (d) 135^o. The low impedance trend in the North and high impedance trend in the South of the maps vary significantly. Figure 2-12a and 2-12c are the predicted anisotropy strike and anisotropic intensity estimated from acoustic impedance anisotropy. Figure 2-12b and 2-12d are the same measures from AVAz. Note that the anisotropy strike and anisotropic intensity estimated from the two approaches show striking similarity, which verifies the presence of acoustic impedance anisotropy in the Barnett Shale. The drilling program consisted of horizontal wells oriented NW-SE since the maximum horizontal stress orients along NE-SW direction. These results refutes the widely-accepted hydraullic fracture model and shows that the induced fractures have widely variable orientations, and we interpret the zones with the consistent orientation to be “fracture compartments” .

Tuning frequency vs. azimuth (FVAz)

Marfurt and Kirlin (2001) analyzed the reflection impulse response of a thin layer embedded in a homogeneous medium, and pointed out that, the spectra maxima occurs when $f \approx 4/T$, f is frequency, T is the thickness of thin-bed in time. After flattening the spectra of the source wavelet, they then showed that the peak frequency measured from spectral decomposition can be employed to map thin-bed thickness. Chapman and Liu (2004) found the frequency dependence on azimuth in the fracture layer by synthetic studies. We can exploit these observations and use peak frequency to measure anisotropy. Since velocity varies with azimuth, so will the time thickness, and hence the peak frequency of each of the thin beds composing the target formation. We provide a simple description of tuning frequency anisotropy as Appendix B.

To compute such anisotropy we first calculate the time-frequency spectra for the entire volume using a matching pursuit approach described by Liu and Marfurt (2007). Next, we assume the reflectivity is random with a white spectra within a 500 ms window over the entire survey:

$$s(t, f) = \frac{1}{N(2K+1)} \sum_{k=-K}^{k=+K} \sum_{x,y} a(t + k\Delta t, f, x, y) \qquad (7)$$

where $a(t, f, x, y)$ is the spectral magnitude at time t, frequency f, and trace location (x, y). With this assumption, the reflectivity spectra can be approximated by

$$\bar{a}(t, f, x, y) = \frac{a(t, f, x, y)}{s(t, f) + \beta MAX[s(t, f)]} \qquad (8)$$

where β is a small whitening factor that prevents boosting unacceptably small source spectral components.

Figure 2-13 shows phantom horizon slices 10 ms above the Ordorvician unconformity through the peak spectral frequency volume from four different azimuths. We see the correlation of peak frequency shown here with the AI slices in Figure 2-11. The lower Barnett Shale is not a homogeneous matrix and can be divided into different parasequences (Singh, 2008) according to different rock types and mineral composition. In Figure 2-14, we interpret event X that might correspond to the top of a parasequence right above Ordorvician unconformity. We find that the thickening of this parasequence from south to north seems to control the change in peak frequency shown in Figure 2-13. Figure 2-15 shows the anisotropy strike in the lower Barnett Shale corresponding to peak frequency anisotropy. Although the result is fuzzy due to the high sensitivity of frequency to noise, the result shows two main trends that can be easily identified in Figures 2-12a and 2-12c.

The processing workflow, advantages, and drawbacks of all four approaches are summarized in Table 1. Hunt et al. (2010) directly correlated natural fractures seen on horizontal image logs and measured by microseismic experiments with VVAz, AVAz and curvature in the Nordegg chert/carbonate formation, and found AVAz has the stronger correlation with image log fracture density and microseismic events than VVAz and curvature. Acoustic impedance anisotropy is more robust than AVAz because AI is calculated from azimuthally-limited stacked data while AVAz is often negatively affected by noise in prestack data.

Correlation with curvature and coherence

In 2D, curvature is defined as the reciprocal of the radius of a circle tangent to a surface. Anticlinal, synclinal, and planar features are represented by positive, negative, and zero values of curvature. In 3D, we fit each point in a surface with two orthogonal tangent circles. Together, these circles define domes, ridges, saddles, valleys, bowls, and planes. Curvature can not only map structural deformation, but also predict azimuth and intensity of paleo fractures. With the passage of time and the change in stress direction, these paleo fractures can be cemented, otherwise diagenetically altered, closed, or open. Coherence seeks for detection of dissimilarity in seismic amplitude, which is only sensitive to discontinuities with relatively large wavelength.

Nelson (2001) stated that, the zones of greater curvature are related to zones with greater strain, such that fractures often occur in folded rocks, especially near the structural hinge line. Hart (2002) and Nissen et. al. (2009) used curvature to map fractures in tight gas sands and shale reservoir respectively. While anisotropiy measures and curvature are mathematically indepedent, both provide indirect inference about fractures; we therefore anticipate crosscorrelations between them through the underlying geology.

Figure 2-16 shows the k_1 most-positive curvature maps from azimuthally-limited stacks of (a) 0^o, (b) 45^o, (c) 90^o, and (d) 135^o. The four maps provide slightly different imaging of structual lineaments with better focusing in some directions, and more smearing in other directions. Figure 2-17 shows k_2 most-negative curvature maps from azimuthally-limited stacks of (a) 0^o, (b) 45^o, (c) 90^o, and (d) 135^o. Other than illumination

issues, we do not expect or observe any difference in curvature with azimuth. Figure 2-18 shows the Sobel filter coherence maps from azimuth (a) 0^o, (b) 45^o, (c) 90^o, and (d) 135^o. Apparently, the geologic discontituities from the four azimuths are illuminated differently in coherence maps, especially the circular karstification features denoted by red arrows. We do expect subtle differences of coherence with azimuth, with subtle fractures perpendicular to the illumination azimuth being somewhat better defined. (Sudhakar and Chopra et al., 2000)

In Figure 2-19a, we co-render the strike from AI anisotropy with k_1 most-positive principal curvature. Note that structural highs seem to form the boundary of different reservoir compartments each of which has a distinct azimuth, implying that azimuthal anisotropy and hence fracture orientation is independent, but consistent within a reservoir compartment delineated by structure highs. In Figure 2-19b, we co-render anisotropic intensity with the same curvature map, and find those structurally highs also correlate to high anisotropic intensity. Thompson et al. (2010a) show that microseismic events generated by hydraulic fracturing avoids these ridges. They postulate that these ridges were fractured during the deformation process and subsequently calcite filled, making these zone harder, and hence serving as barrier to hydraulic fracturing. Rich (2008) found in a different area of the Fort Worth Basin that hydraulic fracturing of wells drilled through such ridges resulted in microseismic events propagating linearly paralell to the ridges with a simultaneous drop in pressure, suggesting that it was easier to pop open the weaker calcite-filled fractures than virgin rock. In summary, the two maps suggest:

1. Hydraulic fracturing is controlled by hetergeneities in the rock due to prior deformation, and

2. the present-day stress regime is modified by hydraulic fracturing, such that subsequent fractures result in a locally uniform anisotropy strike.

We also co-rendered the anisotropic measures with k_2 most-negative curvature, and found very little correlation between them. Figures 2-19c and 2-19d show the composite images of coherence with predicted fracture strike and anisotropic intensity respectively. It is readily apparent that, the discontinuities mapped by coherence is also correlated to the hydraulic fracturing of the lower Barnett Shale, with rocks in vicinity of coherence anomalies (dark lineaments) tend to have greater anisotropy.

In Figure 2-20, we display the polygons of microseismic events from six experiments on the anisotropy intensity map. We expect to see microseismic events occuring in high anisotropy zones. Supprisingly, the observation is oppsite: microseismic events appear in the low anisotropy area, which suggests that good hydaullic fracturing will cause multiple induced fracture orientaions. This finding is consistent with the study made by Thompson (2010b). However, we believe there is still one induced fracture set along a particular orientation having dominant intensity, otherwise the strike of the anisotropy would not give good compartmentalization.

Discussions and conclusions

We demonstrate that, the azimuthal anisotropic measures derived from model-based acoustic impedance provide insight into the induced fractures and stress field in the Barnett Shale. Acoustic impedance reduces the impact of seismic wavelet interference and thin-bed tuning effects, and broadens the spectrum through inclusion of frequency

components from the wells, giving rise to improved vertical resolution within the Barnett Shale, providing results consistent with AVAz.

In the survey under study, the maximum horizontal stress is known to be northeast. The strike of anisotropy shows strong spatial variability but interesting "compartmentalization" with each compartment having the same strike of anisotropy. These compartments are strongly correlated to ridges and domes given by most positive principal curvature, implying that these structural highs either serve as fracture barrier or modify the local stress regime. Correlation of anisotropy measures to microseismic data suggests the existence of multiple azimuth directions in the fractured rocks, but fractures along a particular orientation still dominate.

Multi-linear regression or cluster analysis of anisotropy measures, curvature, and other effective attributes may yield a reliable characterization of induced-fractures and by-passed pay, help us to understand the behavior of bashed and refractured vertical wells and better guide and stimulate horizontal wells.

Acknowledgements

The authors would like to thank Devon Energy for funding, encouragement, and the authorization to publish this work, and particulaly to Mike Ammerman of Devon Energy for conceiving and designing the 3D post hydraulic fracture seismic survey. The first author thanks Heloise B. Lynn for her insight and technical advice.

Appendix A

Wavelet as a function of azimuth

Acoustic impedance anisotropy assumes that impedance varies as azimuth. In the impedance inversion, every azimuthally-limited seismic stack is treated separately and seismic wavelet for different azimuthally-limited stack should also be extracted individually. Figure A-1 shows the seismic wavelets and frequency amplitude and phase spectra extracted from azimuthally-limited data about (a) 0^o, (b) 45^o, (c) 90^o, and (d) 135^o respectively. Two wells are used to extract these constant phase wavelets. Overall, the four wavelets are very similar, but the location of peaks is slightly different in time. The wavelet from azimuth 135^o is quite different from other three.

Appendix B

Tuning frequency anisotropy

When a set of aligned fractures dominates along one direction in the media with horizontal transverse isotropy or orthorhombic symmetry, the velocity differences between the fracture-parallel direction and fracture-perpendicular direction will result in changes in travel time of seismic waves propagating along the two directions. Figure B-1 shows a fracture shale layer with the thickness h in depth overlain by an isotropic, homogeneous limestone layer. Two hypothetical seismic lines are acquired: C-C' parallel to the fractures, and D-D' perpendicular to the fractures. The interval velocity, $V(\psi)$, in section C-C' is greater than the one, $V(\psi+90)$, in section D-D', such that

$$\Delta T(\psi) < \Delta T(\psi+90) \qquad \text{(B-1)}$$

According to Marfurt and Kirlin (2001), $\Delta T \approx 4/f_{peak}$, where f_{peak} is the peak frequency such that

$$f_{peak}(\psi) > f_{peak}(\psi+90) \qquad \text{(B-2)}$$

To illustrate tuning frequency anisotropy, we generate synthetics from a 25m thick shale layer parallel and perpendicular to fractures in Figure B-2a and B-2b, and extract peak frequency from the synthetics (B-2c and B-2d). The synthetic in Figure B-2d from the fracture-perpendicular direction shows push-down effects in the fracture zones caused by the velocity decrease, resulting in a frequency decrease in the peak frequency shown in Figure B-2f. The sensitivity of peak frequency to fractures can be further illustrated by the peak frequency difference (Figure B-2g) obtained by subtracting the

values displayed in B-2f from those in B-2e. Figure B-3 shows the results from a similar model with a shale thickness of 12m, where the same conclusion can be drawn.

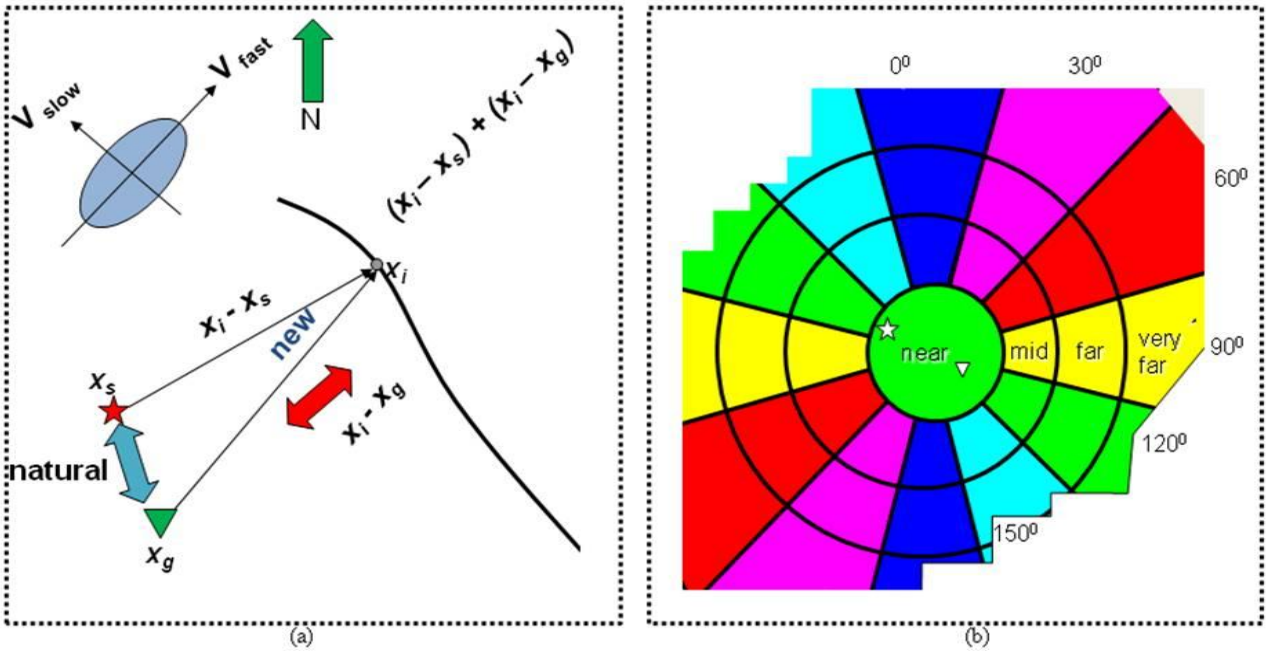

Figure 2-1. Diagrams showing (a) the geometry of side scattered signal, and (b) the output of the migration divided into different offset and azimuth sectors. The new image point azimuth binning approach embedded in our PSTM algorithm sorts the data by azimuth as it is imaged in the subsurface. (after Perez and Marfurt, 2008)

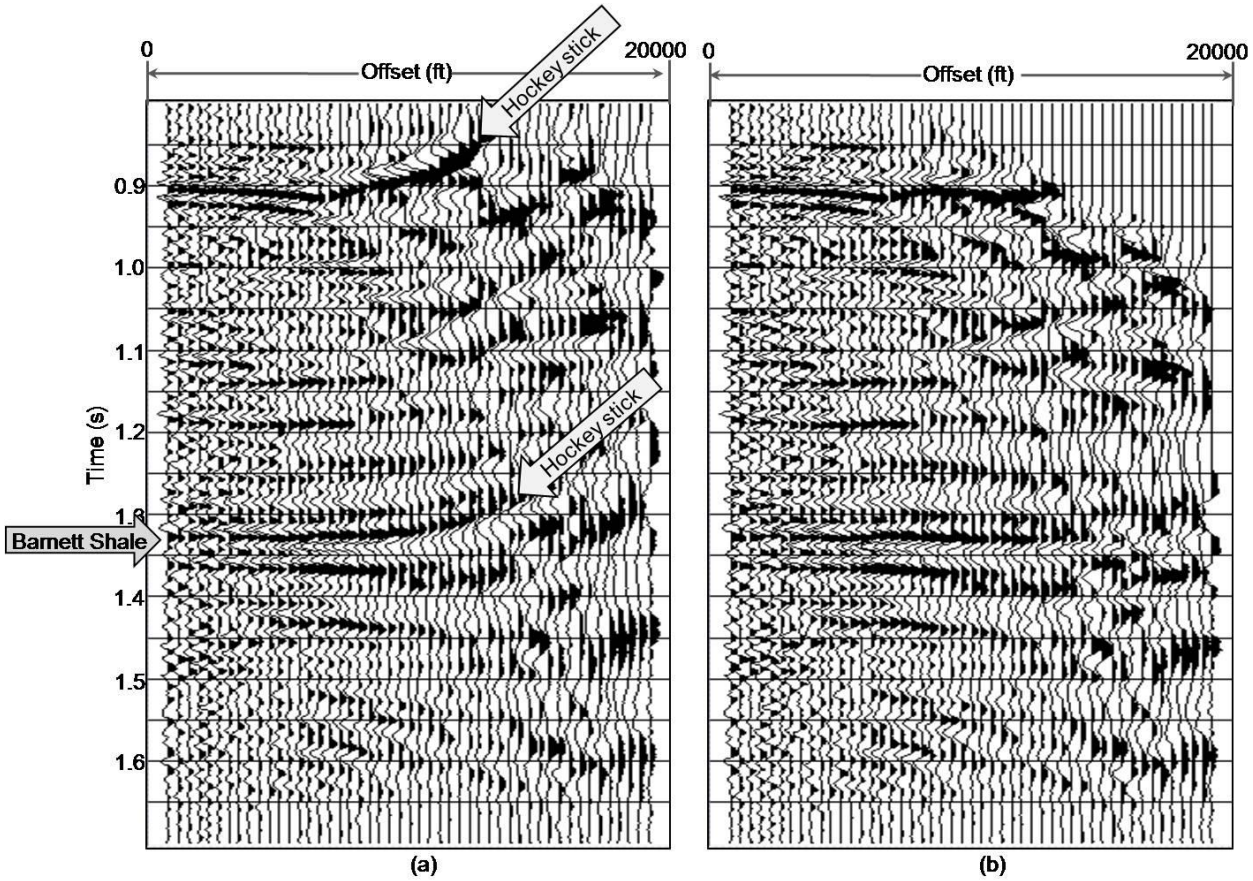

Figure 2-2. A representative common reflection point gather (a) before, and (b) after RMO analysis. Yellow arrows indicate "hockey sticks". The large offset residual moveout (or "hockey stick") beyond 7000 ft is corrected to be flat after RMO analysis, which is critical to later fracture characterization. The depth to the Barnett Shale target is about 7000 ft.

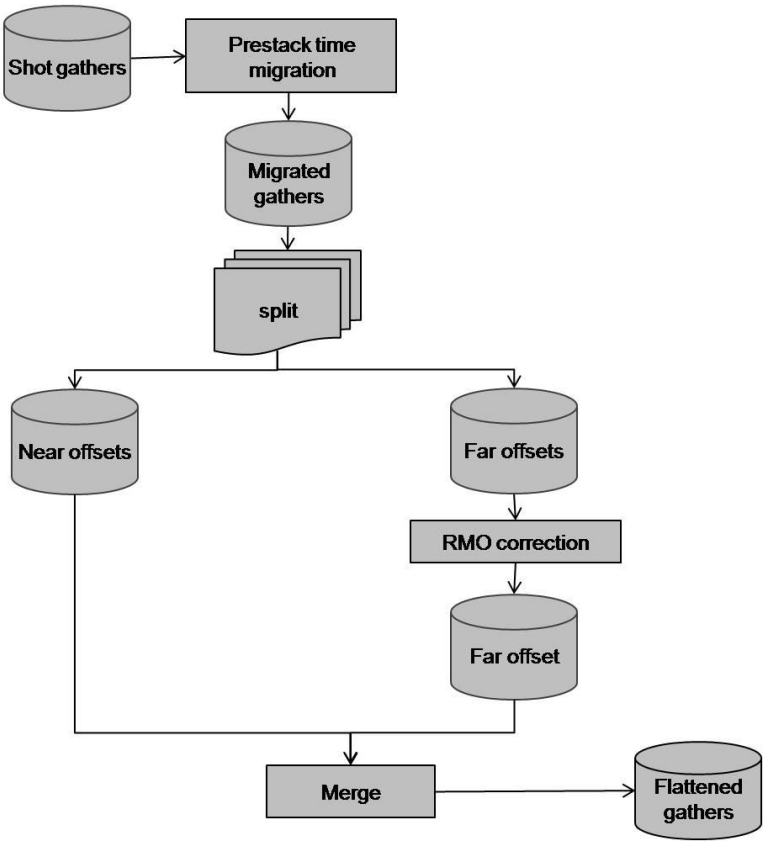

Figure 2-3. Two-step RMO correction workflow.

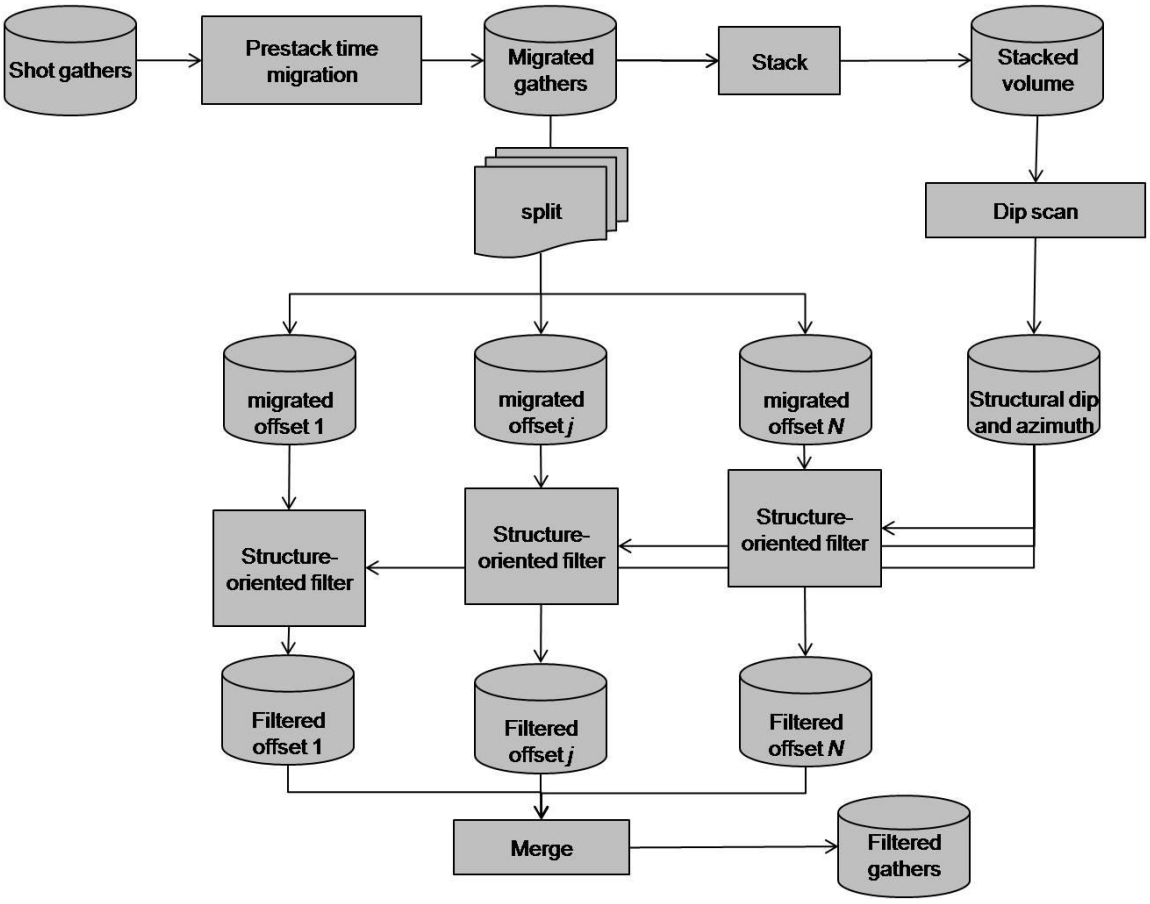

Figure 2-4. Workflow used to condition the prestack migrated gathers.This process is both edge- and AVO-preserving.

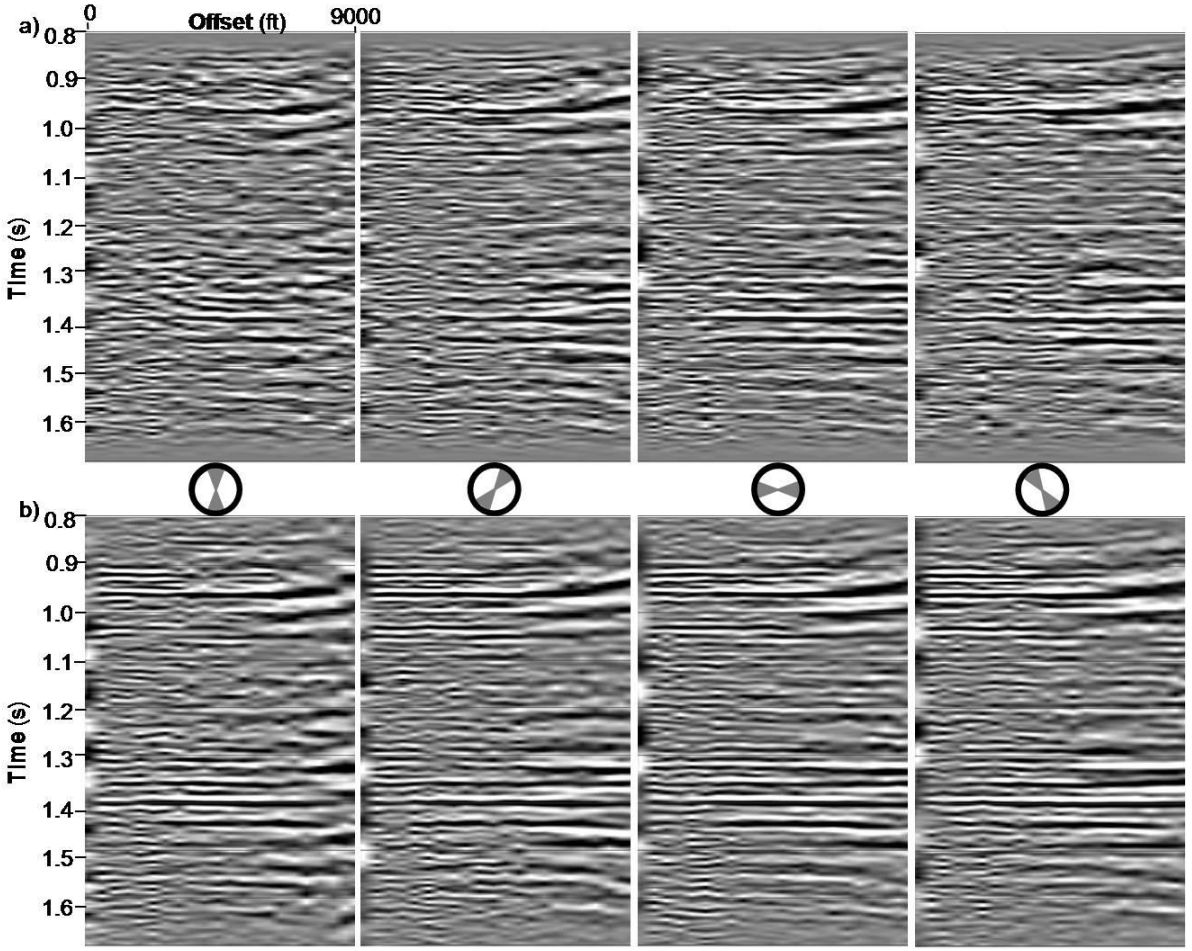

Figure 2-5. Representative migrated CRP gathers from four different azimuths (a) before, and (b) after the pre-stack structure oriented filtering. Notice the great enhancement of signal-noise-ratio.

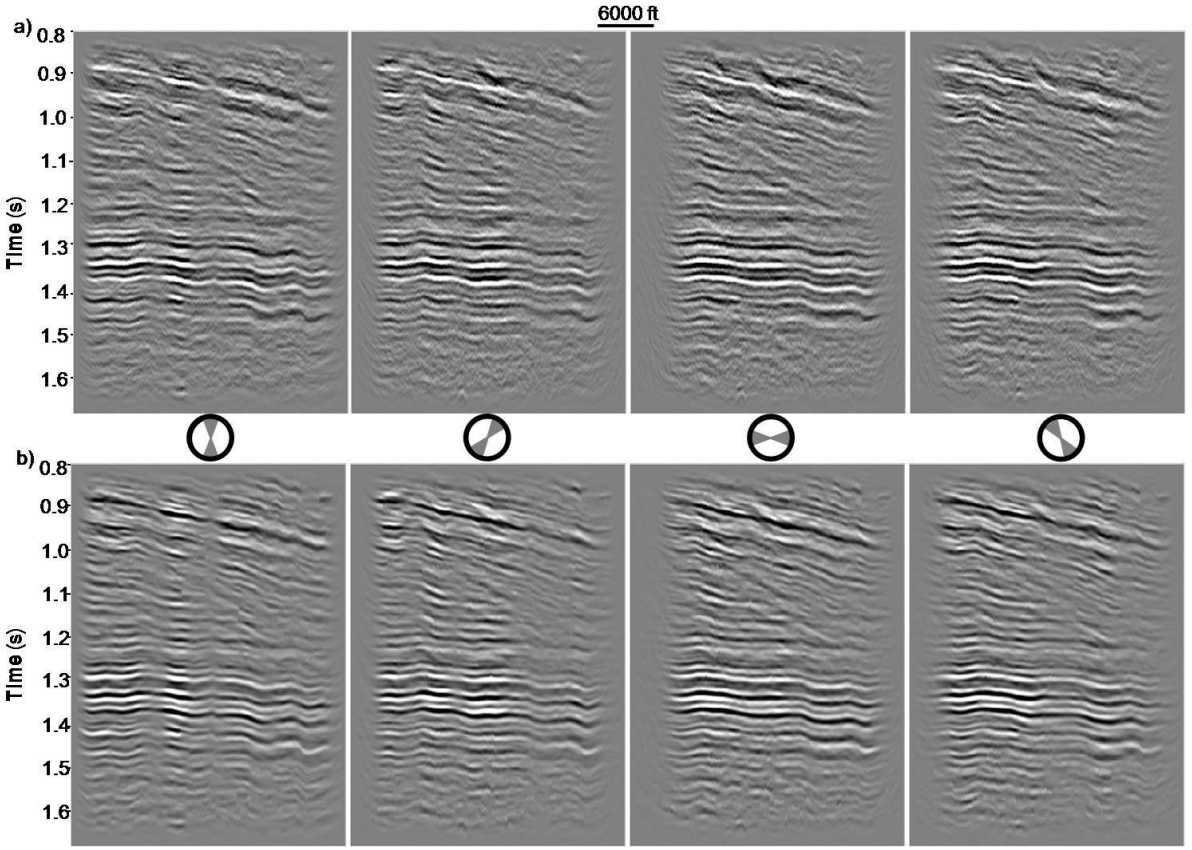

Figure 2-6. Representative stacks from four different azimuths along line AA' (a) before, and (b) after the pre-stack structure oriented filtering. Location of line AA' is shown on Figure 2-10. The random, uncorrelatable energy component is attenuated after conditioning.

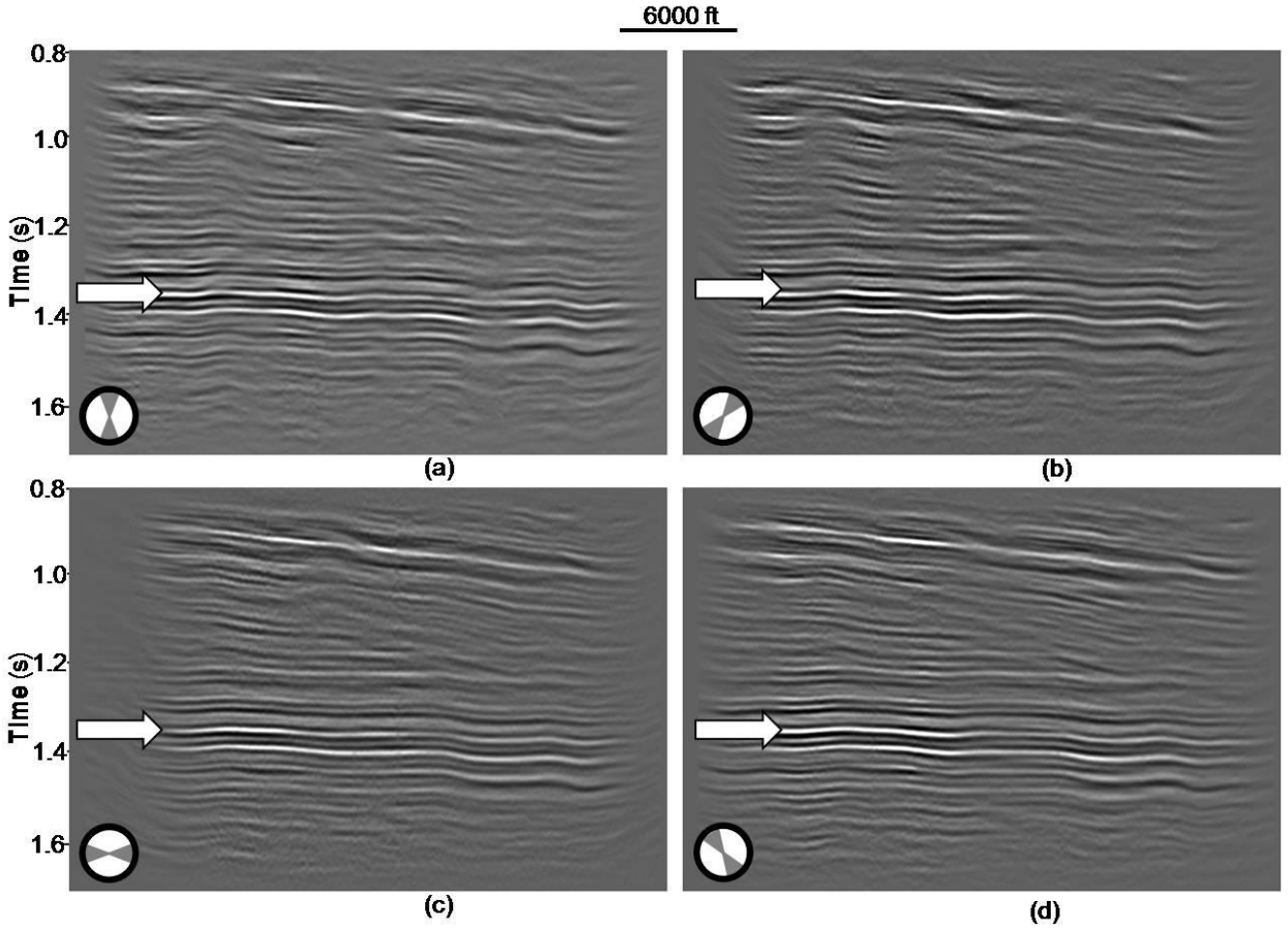

Figure 2-7. The representative azimuth stacked sections after all processing along AA' about 0^{o}, 45^{o}, 90^{o}, and 135^{o}. Note that illumination changes slightly with azimuth. Block arrows indicate the Lower Barnett Shale horizon.

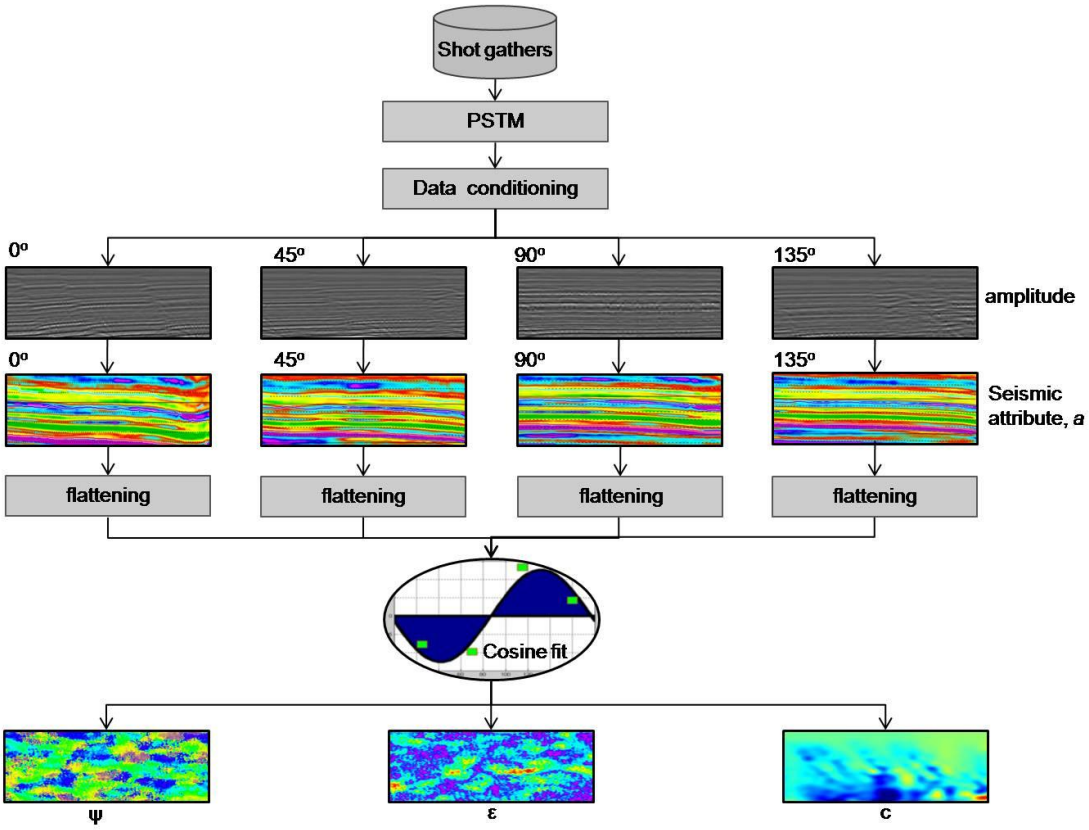

Figure 2-8. Workflow to calculate azimuthal anisotropy from a seismic attribute, *a*. In this example, the seismic attribute is acoustic impedance. A cosine of azimuth, Ψ, and amplitude, ε, is fit to the value of corresponding samples (represented by green squares) from each azimuthally-limited input volume. Ψ is the strike of the largest value of *a*, ε is anisotropic deviation from a constant value, and *c* is the confidence of the least-squares fit.

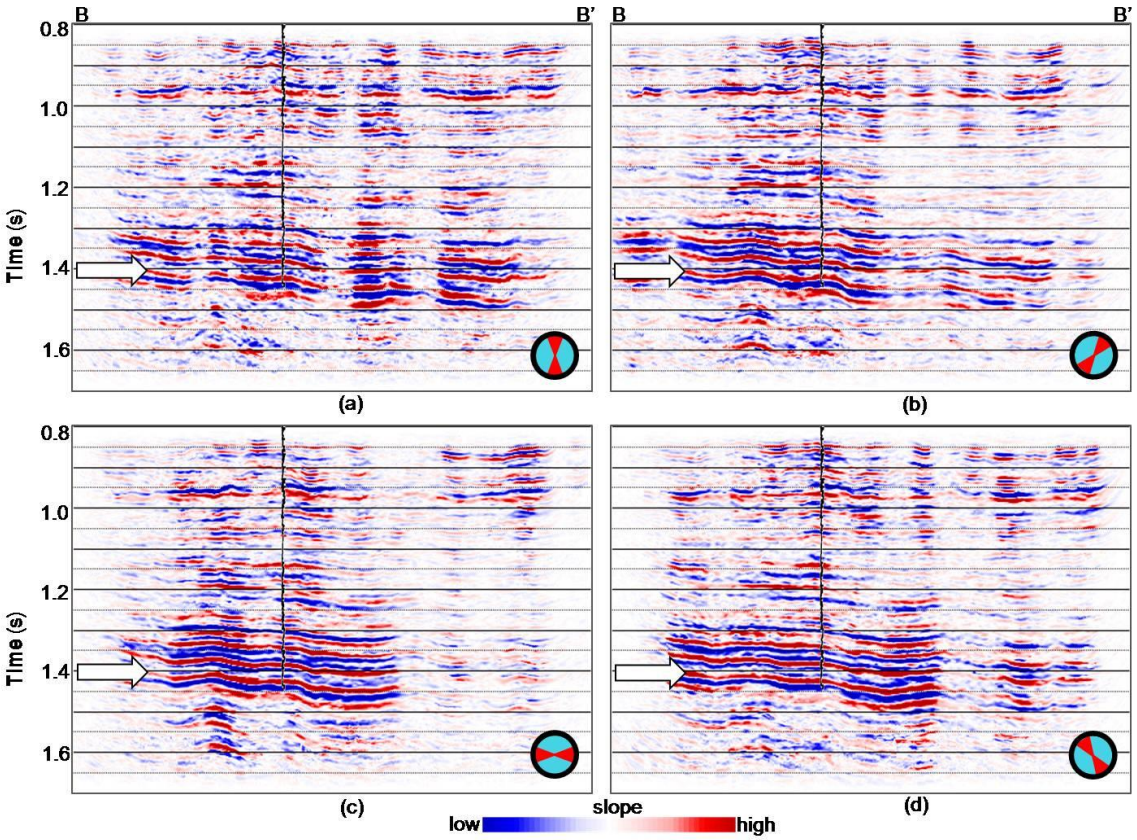

Figure 2-9. Line BB' through the AVO gradient computed from azimuthally-limited volumes at (a) 0^{o}, (b) 45^{o}, (c) 90^{o}, and (d) 135^{o}. Note the variation in AVO response for different azimuths. Location of line is shown on Figure 2-10. Black curve represents Gamma ray log. Block arrows indicate the Lower Barnett Shale horizon.

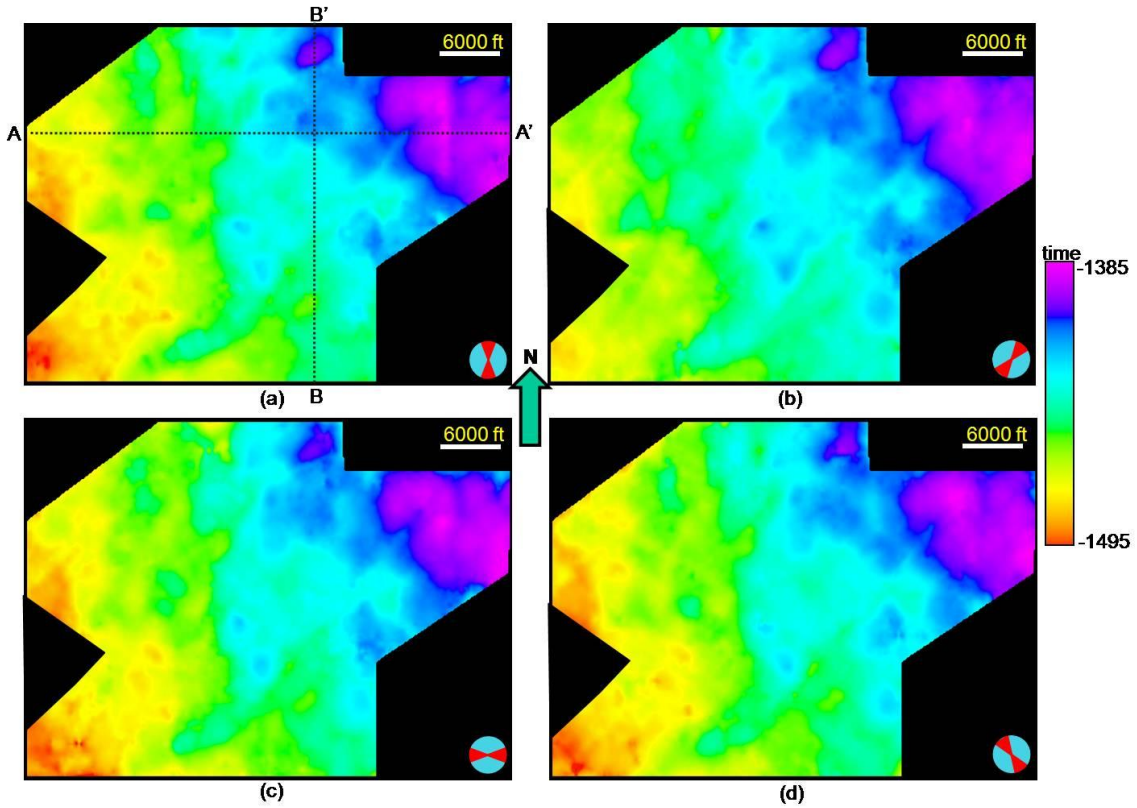

Figure 2-10. Time structure maps of the Ordovician unconformity about (a) 0^{o}, (b) 45^{o}, (c) 90^{o}, and (d) 135^{o} respectively.

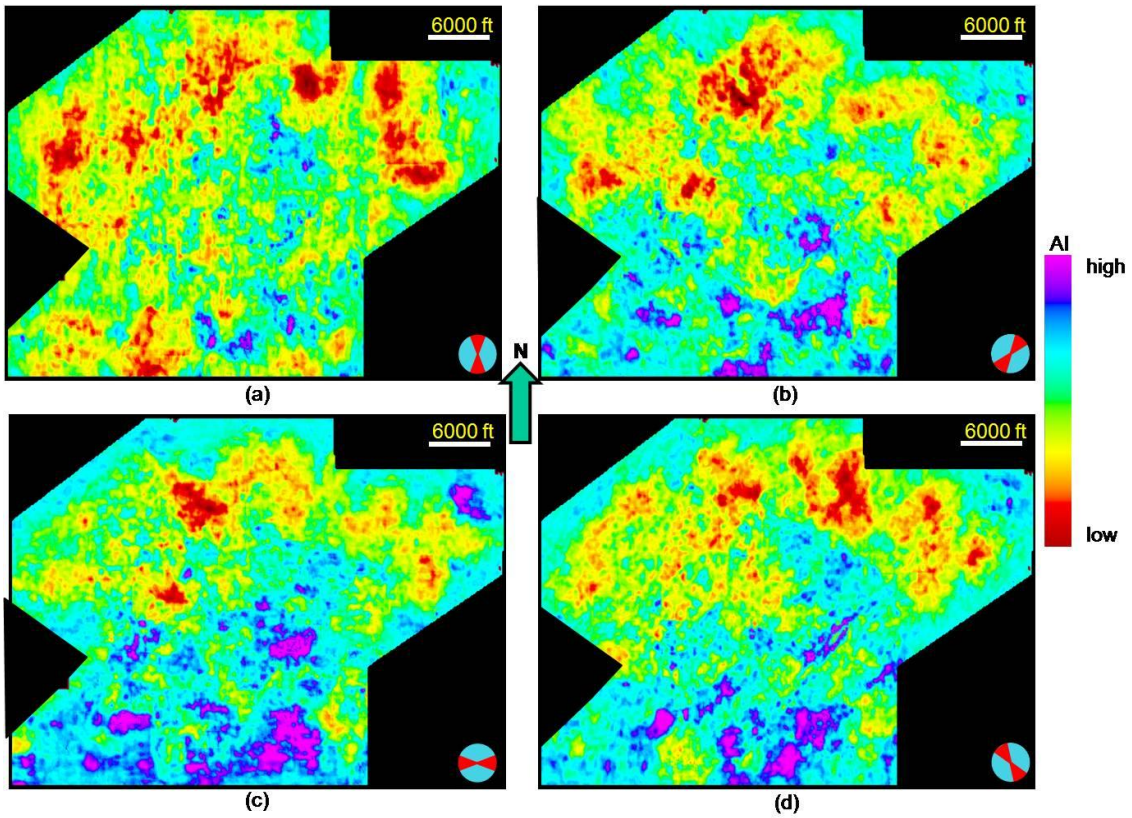

Figure 2-11. Phantom horizon slices 10 ms above the Ordovician unconformity through acoustic impedance volumes computed from azimuthally-limited data about (a) 0^{o}, (b) 45^{o}, (c) 90^{o}, and (d) 135^{o} respectively. Note the low impedance trends in the North, and high impedance trends in the South vary considerably across the four different azimuths.

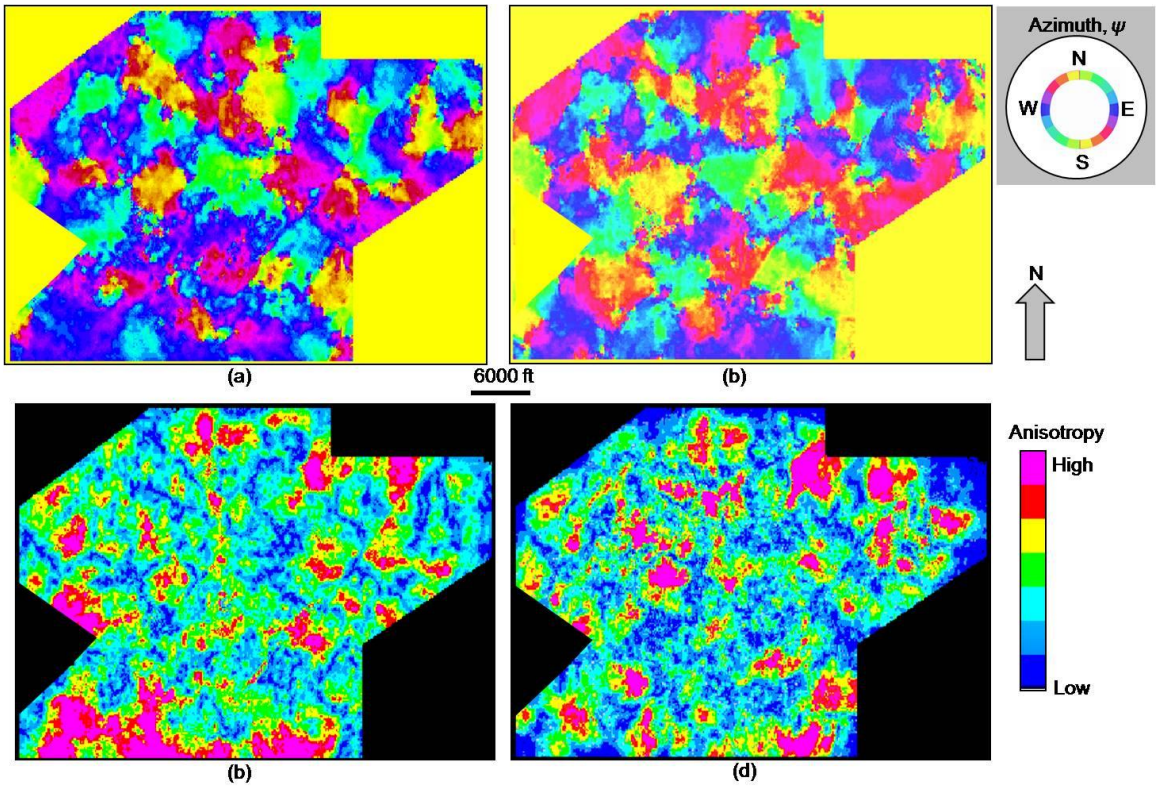

Figure 2-12. Phantom horizon slices 10 ms above the Ordovician unconformity of the azimuth of anisotropy, ψ, computed from (a) acoustic impedance and (b) AVAz. Phantom horizons at the same level through the intensity of anisotropy, ε, computed from (c) acoustic impedance and (d) AVAz. Overall, the results are similar. The drilling program consisted of horizontal wells oriented NW-SE to better generate fractures parallel to the maximum horizontal stress oriented NE-SW. This image refutes the widely-accepted hydraulic fracture model and shows the fractures with widely variable orientations, though these orientations remain consistent in what we interpret to be ”fracture compartments”.

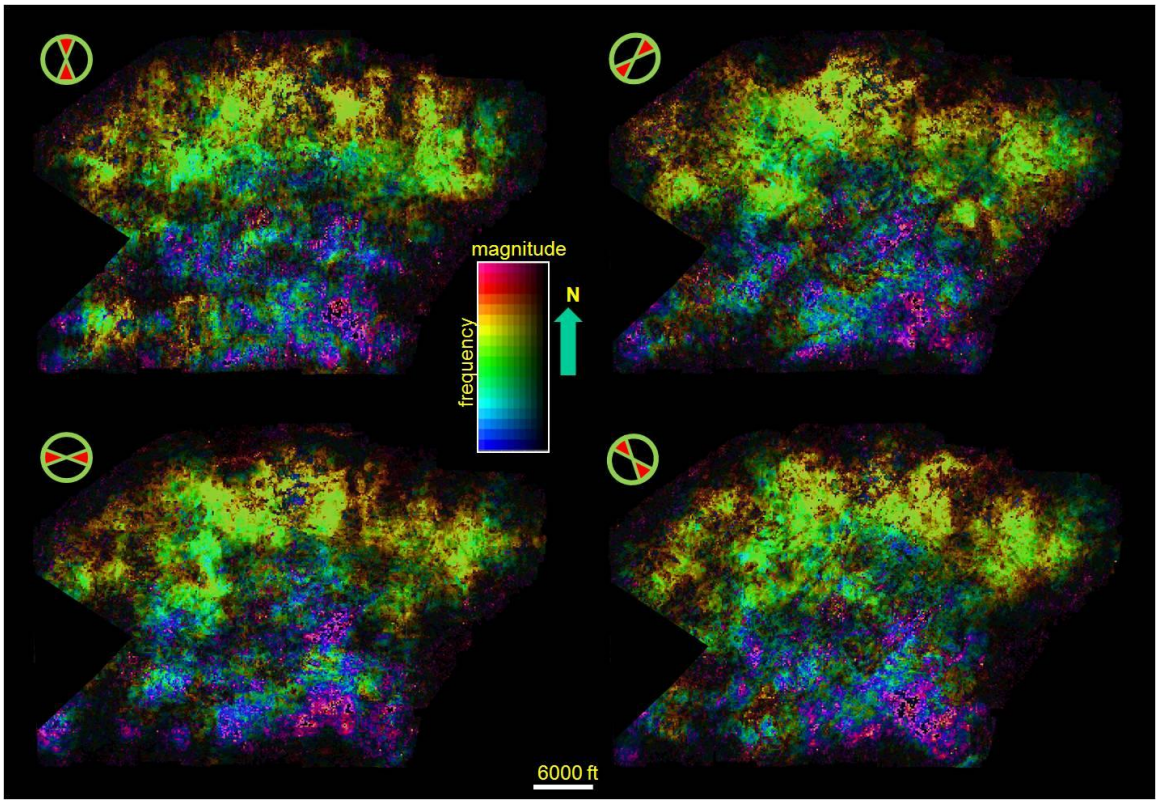

Figure 2-13. Phantom horizon slices through the four peak frequency volumes 10 ms above the Ordovician unconformity computed from azimuthally-limited volumes about (a) 0^o, (b) 45^o, (c) 90^o, and (d) 135^o. We interpret the overall trend of higher peak frequency (yellows and greens) in the north and lower peak frequency (magenta) in the south to be associated with layering and the azimuthal variation to be associated with induced fractures. Also notice the correlation of peak frequency shown here with the AI slices in Figure 2-11.

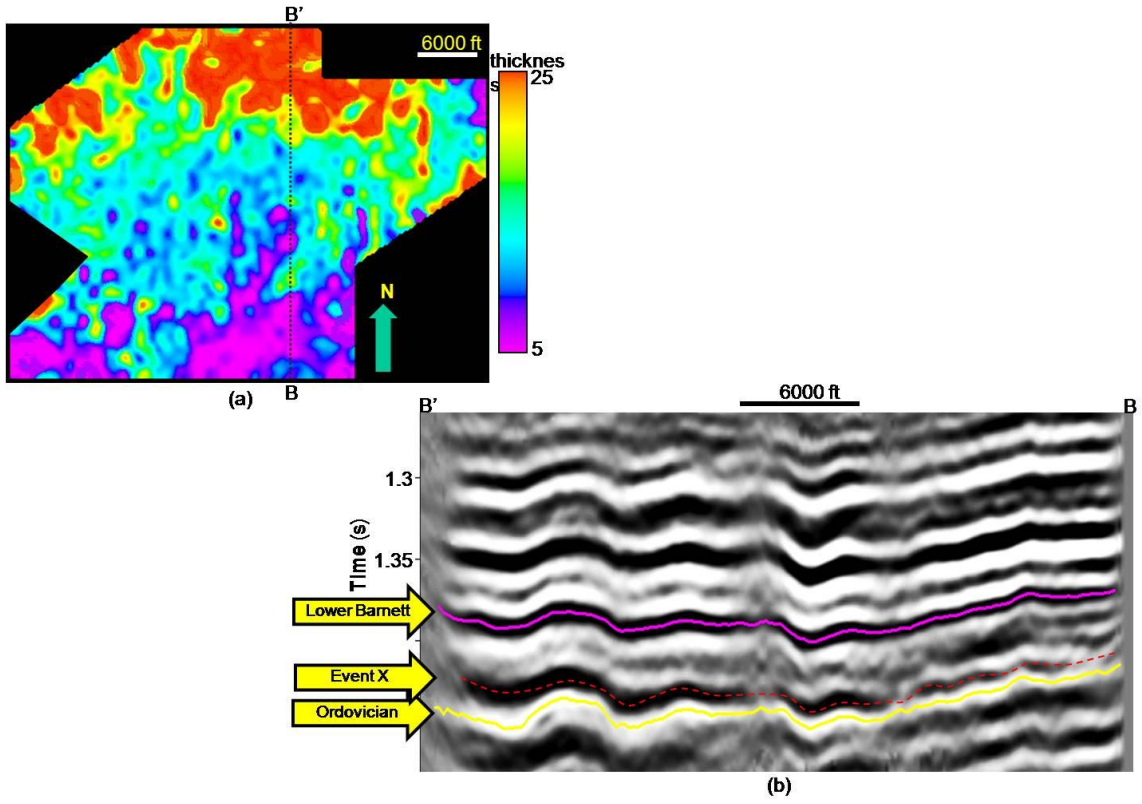

Figure 2-14. (a) Isochron extracted from Ordovician unconformity and event X above interpreted using azimuthally-limited seismic volume of 0^{o}. (b) Vertical seismic section BB' with interpreted Lower Barnett Shale, Ordovician unconformity and event X. The thickening of the isochron from south to north explains the decrease of dominant frequency shown in Figure 2-13.

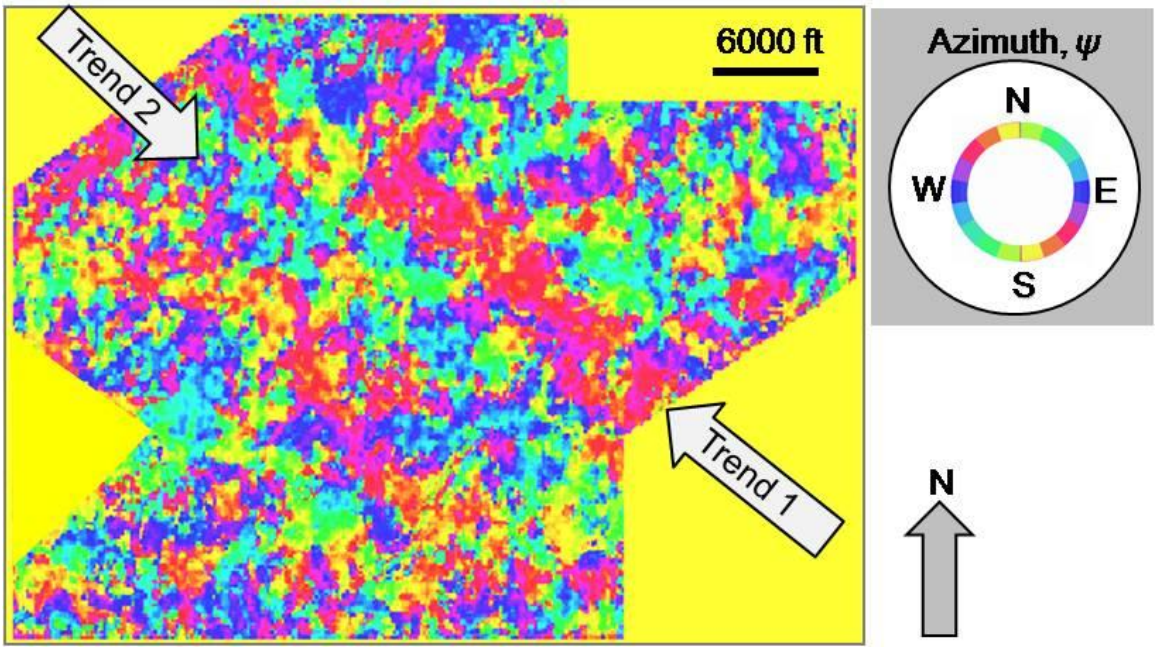

Figure 2-15. Phantom horizon slice 10 ms above the Ordovician unconformity through the azimuth of anisotropy volume, ψ, computed from the peak spectral frequency. The two NW-SE trends denoted by arrows are also easily identifiable in Figures 2-12a and 2-12b, but overall, this image seems to have significantly less lateral resolution.

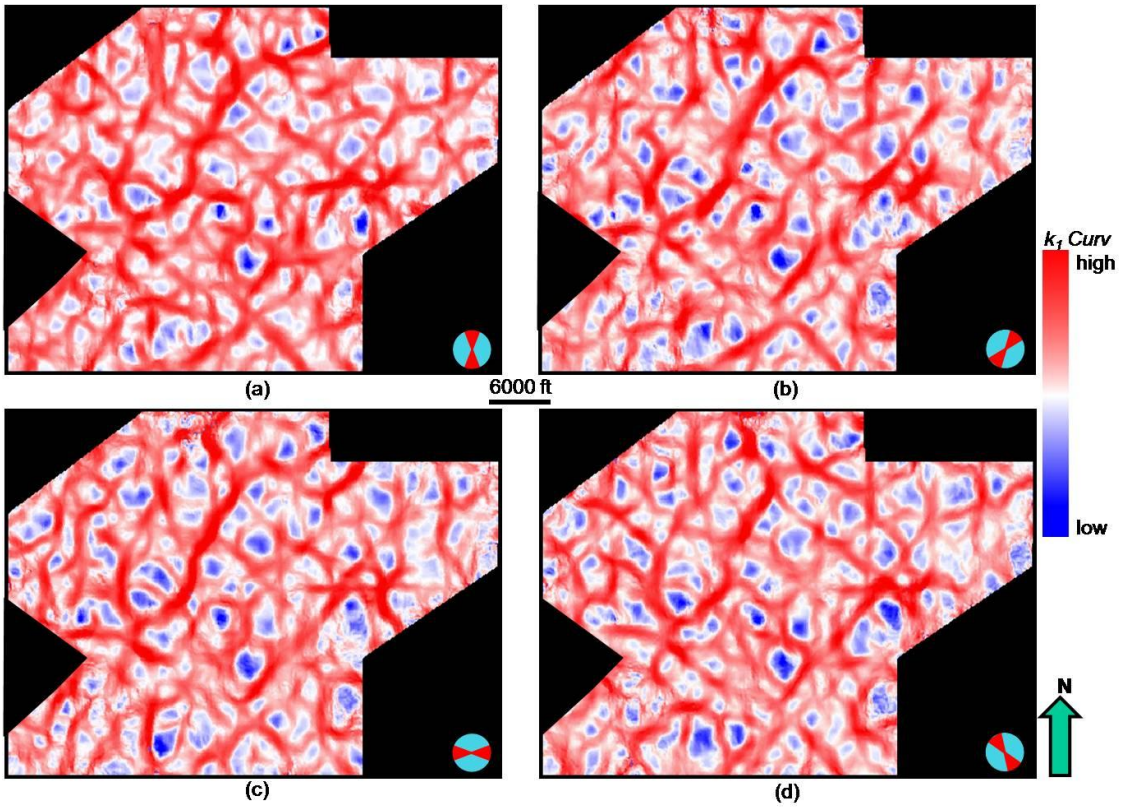

Figure 2-16. Phantom horizon slices 10 ms above Ordovician unconformity through k_1 most-positive principal curvature computed from azimuthally-limited volumes of (a) 0^o, (b) 45^o, (c) 90^o, and (d) 135^o respectively. The images are very similar, since hydraulic fracturing does not change the structure, but rather only the velocity.

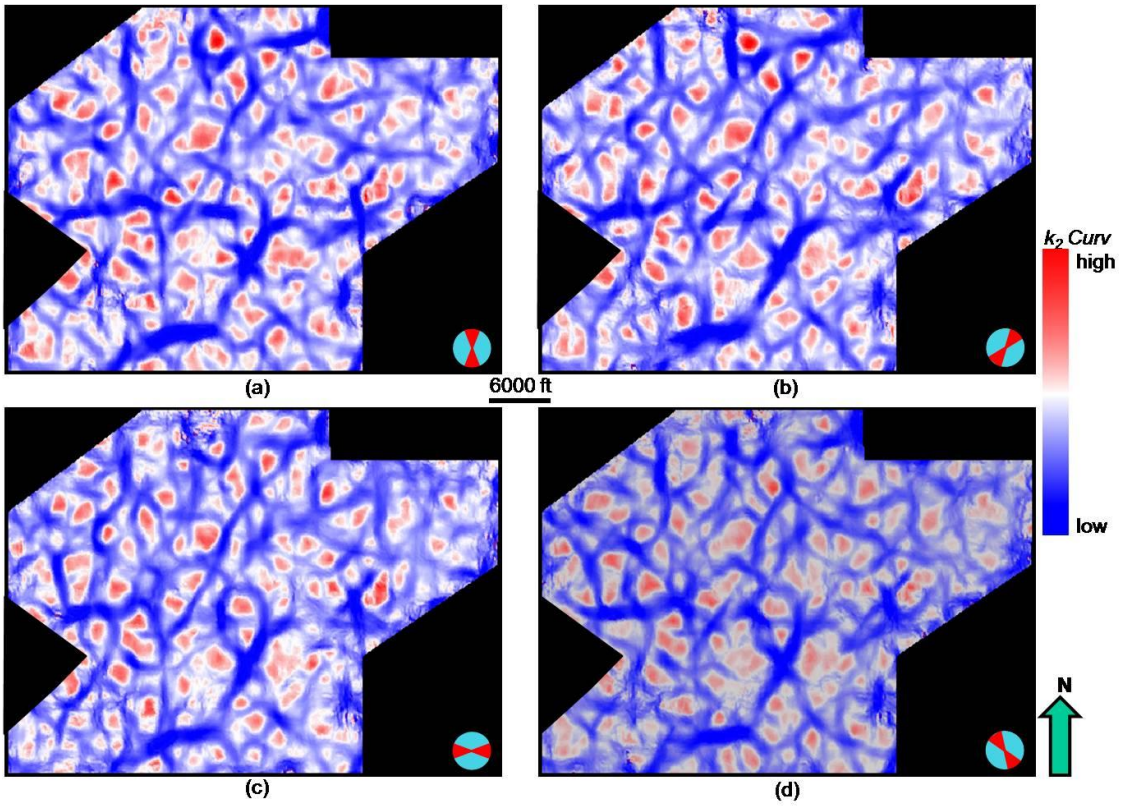

Figure 2-17. Phantom horizon slices 10 ms above Ordovician unconformity through k_2 most-negative principal curvature computed from azimuthally-limited volumes about (a) 0^o, (b) 45^o, (c) 90^o, and (d) 135^o.

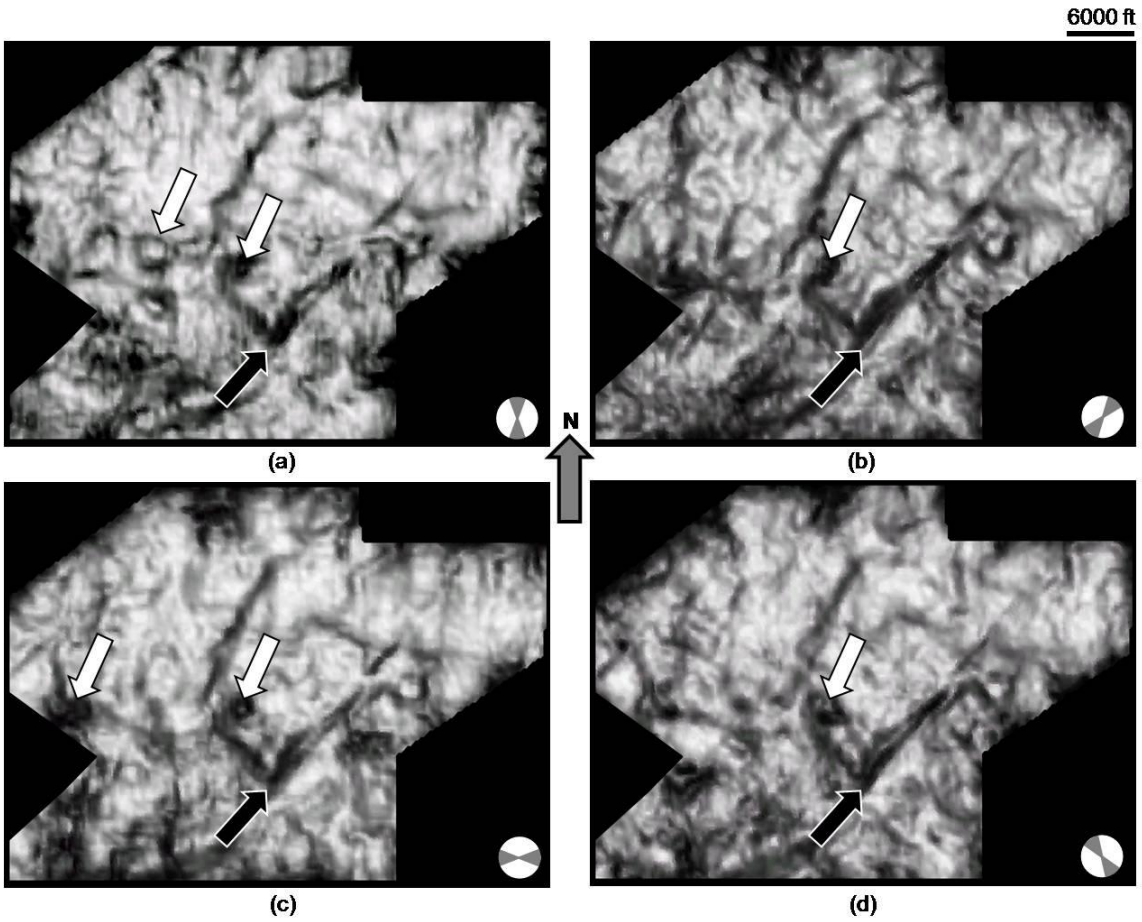

Figure 2-18. Phantom horizon slices 10 ms above Ordovician unconformity through the Sobel filter similarity computed from azimuthally-limited seismic volumes about (a) 0^o, (b) 45^o, (c) 90^o, and (d) 135^o. Note how the collapse features indicated by the block white arrows and the NE-SW-trending fault indicated by the block black arrows are illuminated differently at the four azimuths.

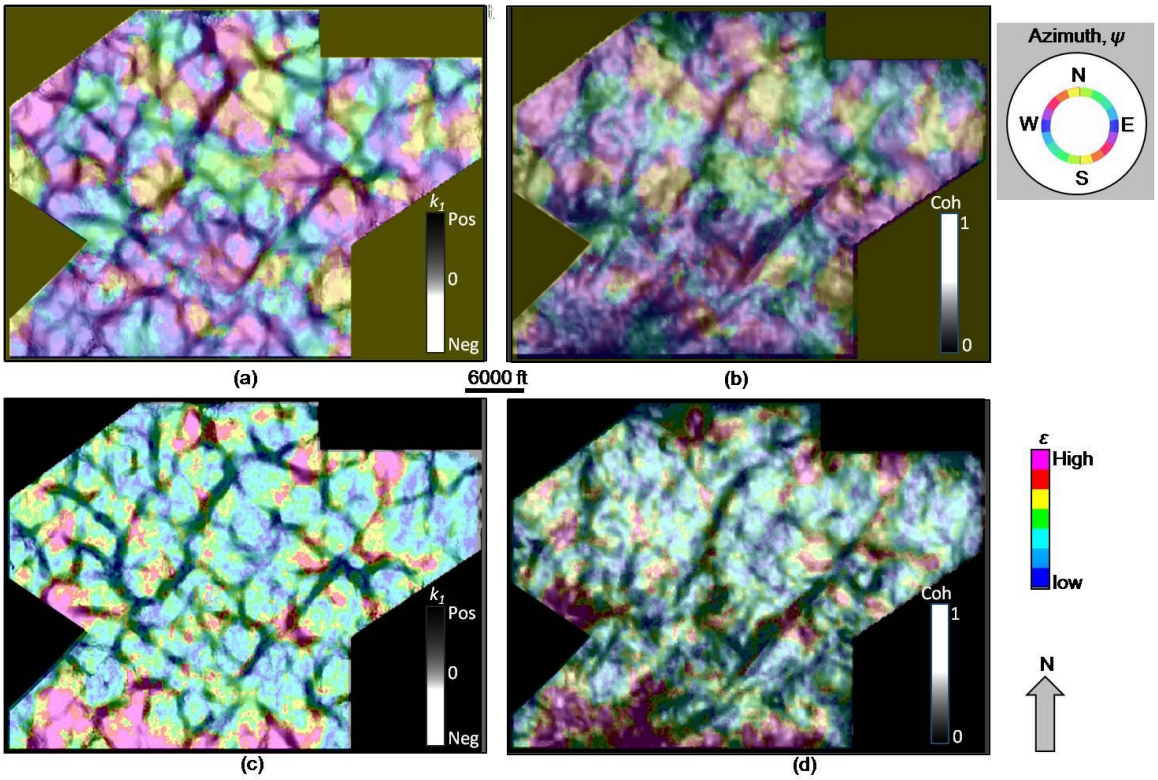

Figure 2-19. Composite images of anisotropy strike, ψ, co-rendered with (a) k_1 curvature, and (b) Sobel-filter similarity. Composite images of anisotropic intensity, ε, co-rendered with (c) k_1 curvature, and (d) Sobel-filter similarity. The curvature and similarity maps are obtained from the azimuthally-limited migrated stack about 45^{o}. Notice that limits of zones having the same strike of anisotropy are highly correlated to the structural ridges and domes delineated by the k_1 curvature. The Sobel filter similarity shows similar trends, but only of the larger, more discontinuous features.

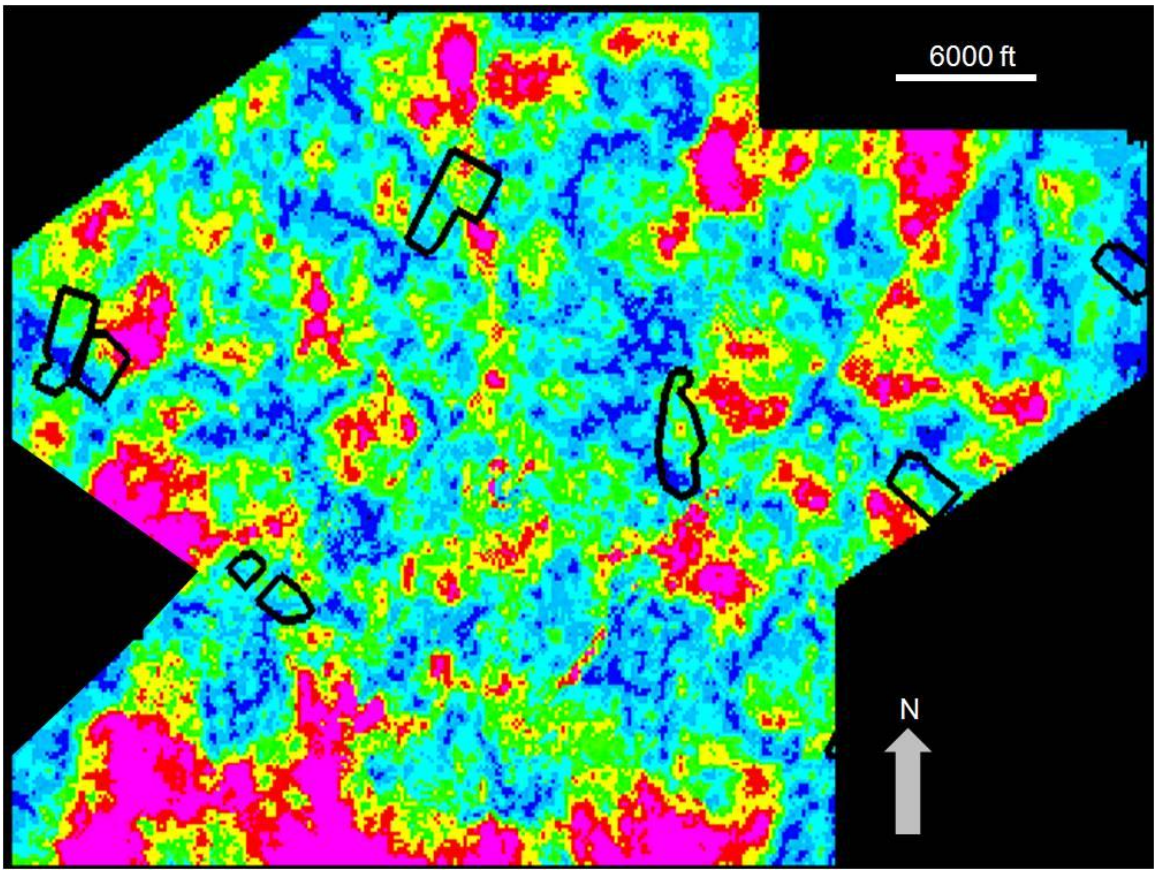

Figure 2-20. Anisotropy intensity with polygons of microseismic events from six experiments. Notice the micro-seismic events appear in areas of low anisotropy intensity.

	workflow	advantages	drawbacks
VVAz	▪ Generate long-offset 'tiles' at different azimuths, φ, typically of unmigrated data ▪ At discrete picked horizons, compute V_{RMS} as a function of azimuth, φ ▪ Compute interval velocities $V_{int}(\varphi)$ using Dix's equation ▪ Fit a sinusoidal curve to $V_{int}(\varphi)$ to obtain the magnitude and azimuth of anisotropy	▪ Easy to generate azimuthally-binned data ▪ Uses conventional velocity analysis software ▪ Computation is fast and simple, providing a level of confidence ▪ Requires phase- but not amplitude-preservation	▪ Suffers from vertical resolution problems associated with Dix's equation ▪ Provides results only on picked interfaces
AVAz	▪ Generate long-offset 'tiles' at different azimuths, φ, typically of migrated data ▪ Pick discrete upper and lower horizons and generate either flattened or stratal slices throughout the volumetric zone of interest ▪ Compute AVO gradient B(φ) ▪ At every time or depth sample, fit a sinusoid to the AVO gradient as a function of azimuth, φ	▪ Easy to generate azimuthally-binned data ▪ Computation is fast and simple, providing a level of confidence in the estimates ▪ Computations are volumetric within the (properly registered) zone of interest	▪ Requires amplitude-preserving processing and migration ▪ Suffers from wavelet side lobes and thin bed tuning
Acoustic impedance anisotropy	▪ Generate long-offset 'tiles' at different azimuths, φ, typically of migrated data ▪ Estimate a wavelet for each azimuth at key wells ▪ Compute model-driven inversion using commercial software ▪ Pick discrete upper and lower horizons and generate either flattened or stratal slices throughout the volumetric zone of interest ▪ At every time or depth sample, fit a sinusoid to the impedance as a function of azimuth, φ	▪ easy to generate azimuthally-binned data ▪ Impedance inversion removes wavelet side lobes and thin-bed tuning effects ▪ Computation is fast and simple, providing a level of confidence in the estimates ▪ Computations are volumetric within the (properly registered) zone of interest	▪ Requires amplitude-preserving processing and migration ▪ computation requires familiarity with commercial impedance inversion software
Tuning frequency anisotropy	▪ Generate long-offset 'tiles' at different azimuths, φ, typically of migrated data ▪ Pick discrete upper and lower horizons and generate either flattened or stratal slices throughout the volumetric zone of interest ▪ At every time or depth sample, fit a sinusoid to the peak, dominant , or response frequency as a function of azimuth, φ	▪ Easy to generate azimuthally-binned data ▪ Methodology uses the tuning effects as signal rather than as artifact ▪ Computation is fast and simple, providing a level of confidence in the estimates ▪ Computations are volumetric within the (properly registered) zone of interest ▪ Requires phase- but not amplitude-preservation	▪ Unclear how the method works when there are composite reflectors rather than a simple thin-layer two-reflector model

Table 2-1. Comparison of workflow, advantages, and drawbacks of VVAz, AVAz, acoustic impedance anisotropy, and tuning frequency anisotropy.

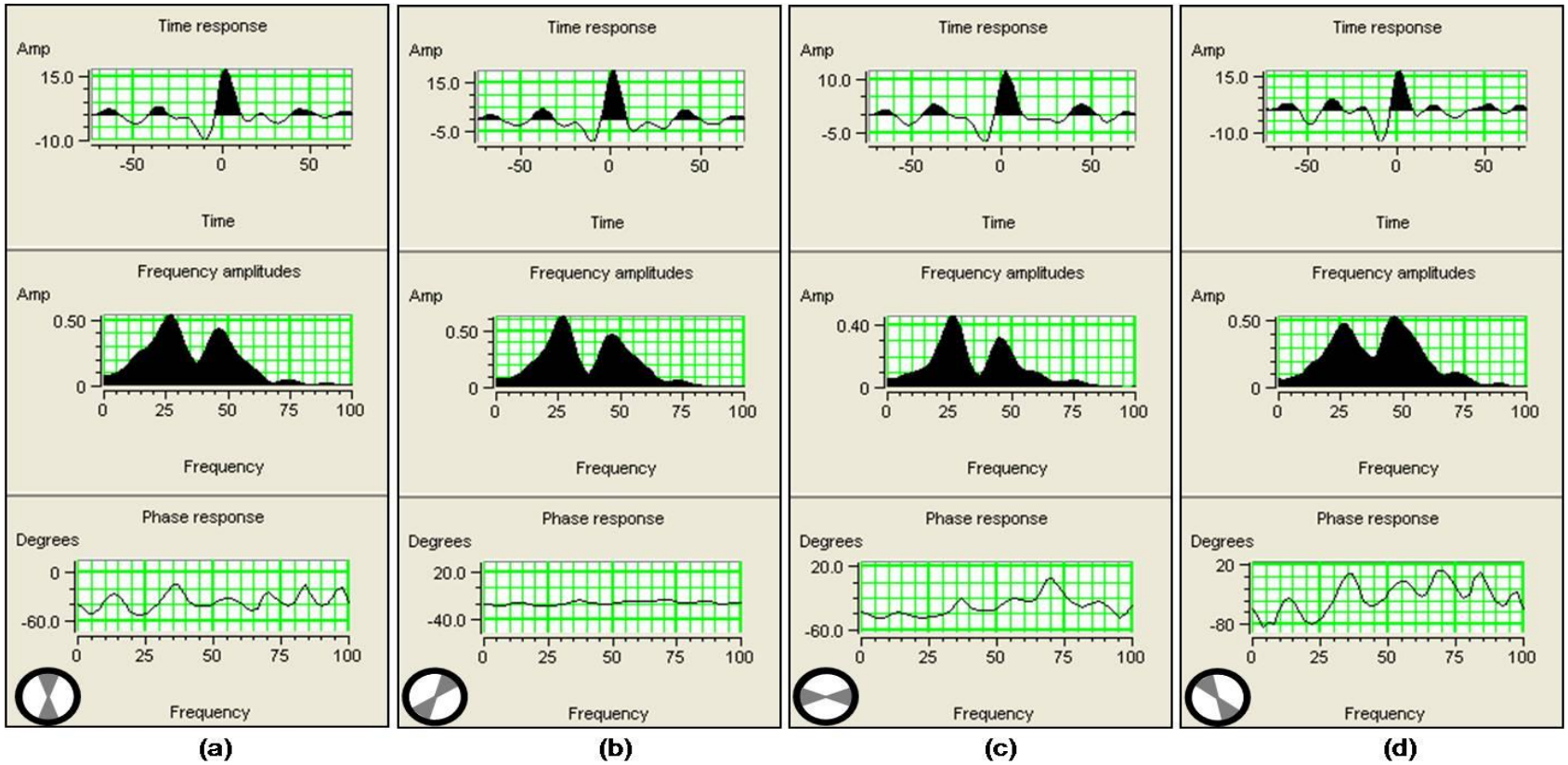

Figure A-1. Seismic wavelets and frequency amplitude and phase spectra extracted from azimuthally-limited data about (a) 0^o, (b) 45^o, (c) 90^o, and (d) 135^o respectively. The four wavelets have similar shape in time domain and peak amplitude has slightly different time-lag. Note that the bi-modal behavior of amplitude spectrum of the wavelet in (d) is different from that of other three wavelets.

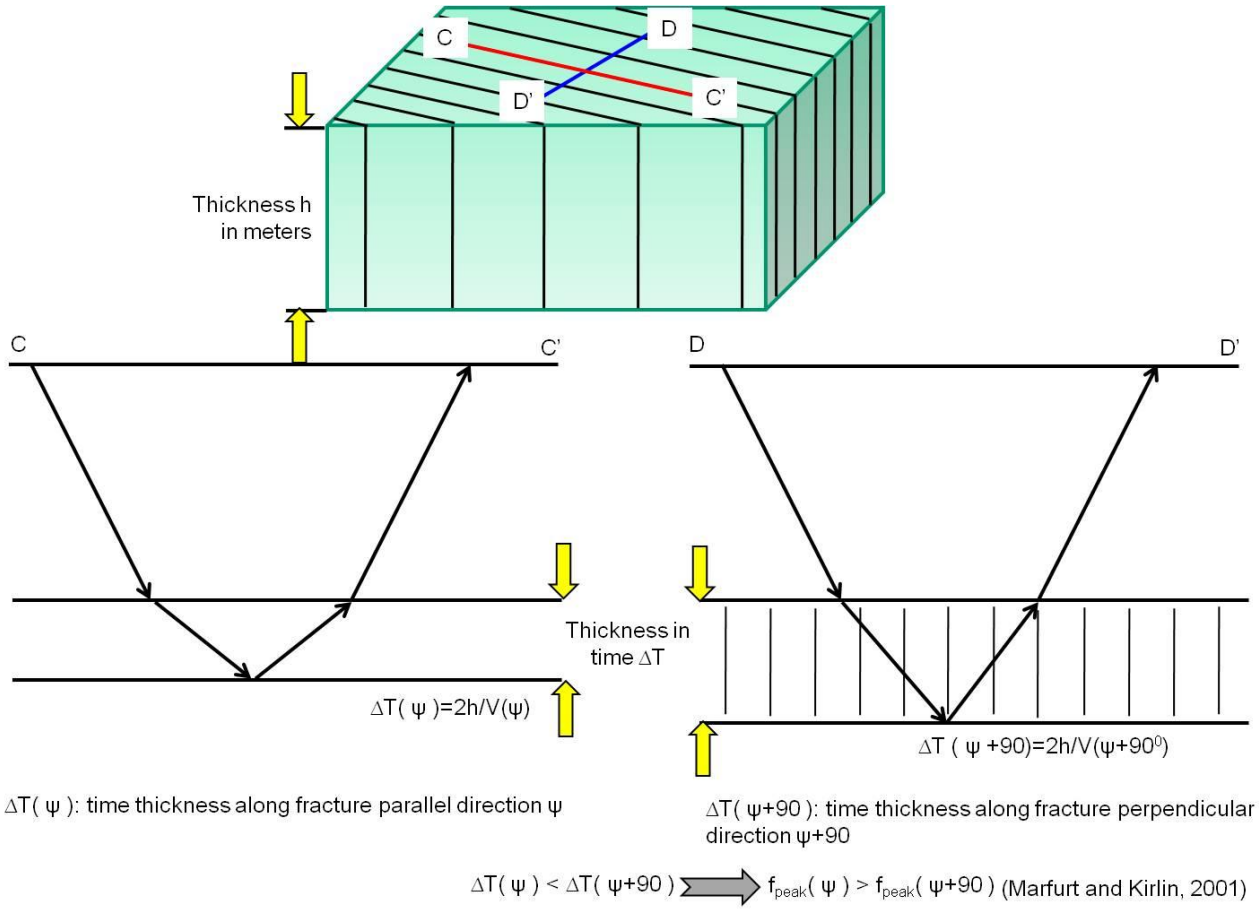

Figure B-1. The fracture model shows the time-domain thin-bed thickness difference when seismic energy travels along fracture-parallel and perpendicular directions.

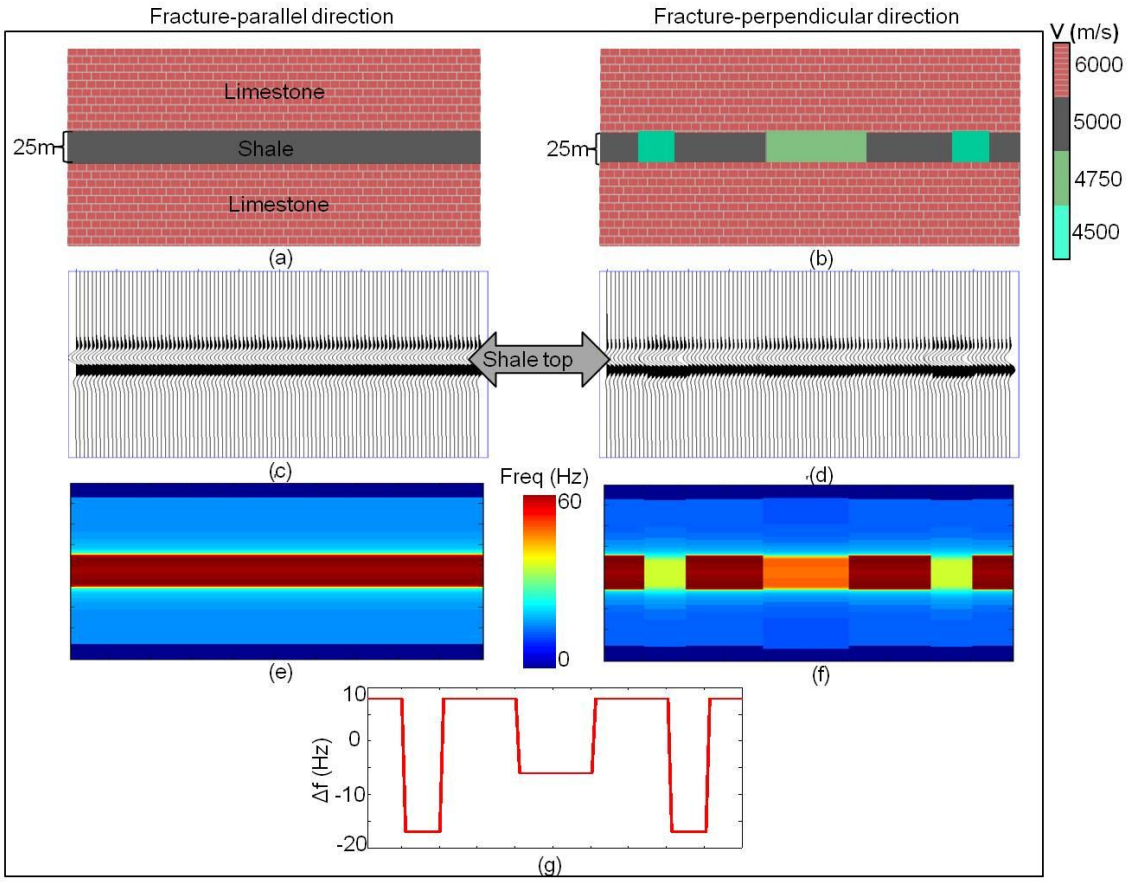

Figure B-2. Model of a 25 m thick fractured shale. Vertical slices through the model (a) parallel to and (b) perpendicular to the fractures. (c) and (d) show synthetics computed from (a) and (b) while (e) and (f) show the peak frequency computed from (c) and (d). (g) is a graph of the difference in the peak frequency shown in (f) and (e) along the top of the shale. Negative values in (g) indicate fracture zones.

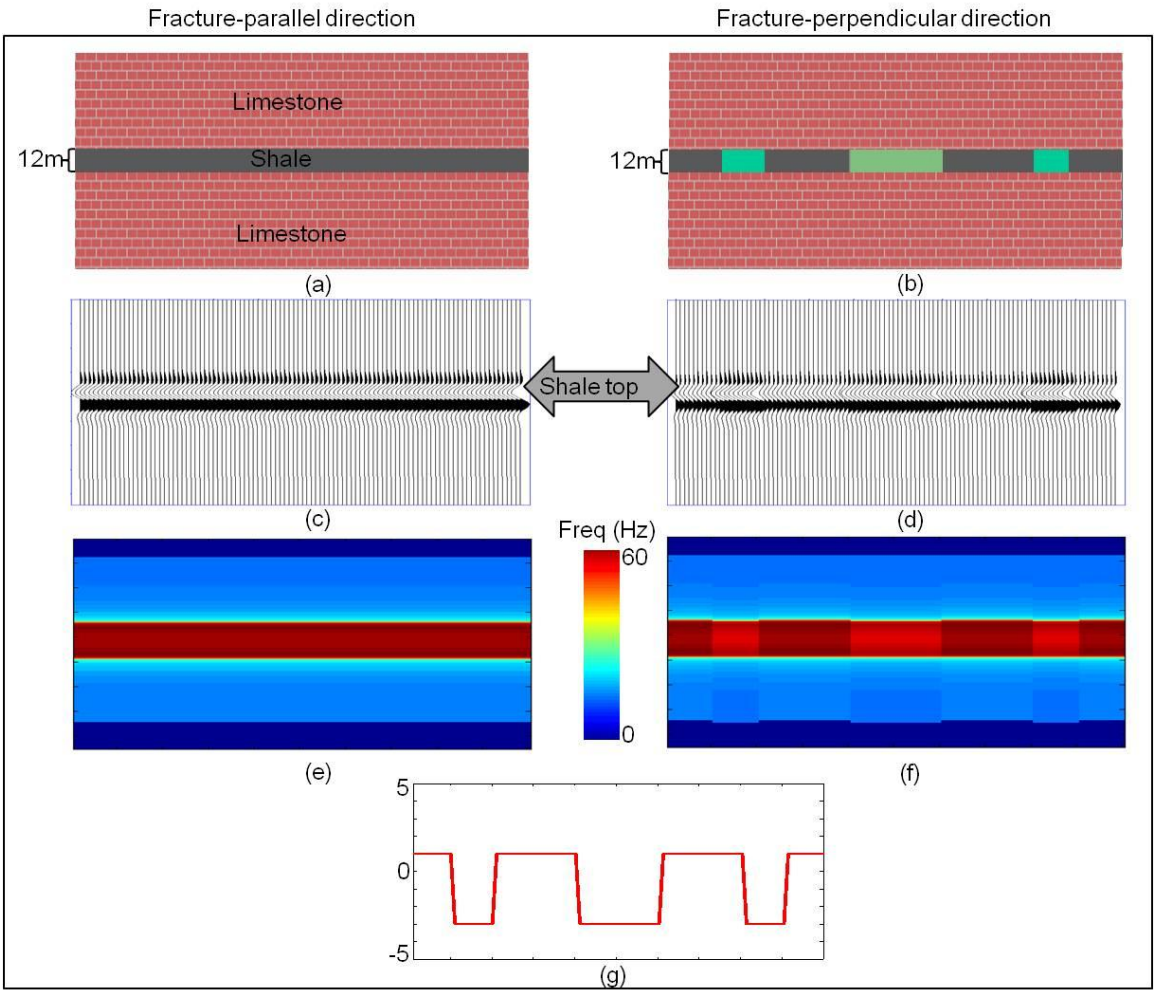

Figure B-3. The same model, synthetics and peak frequency cross sections shown in Figure B-2, but now for a shale layer that is only 12 m thick. Although the shale layer is very thin, the peak frequency is still able to differentiate the fractured from the non-fractured zones.

References

Chapman M., and E. Liu, 2004, Frequency dependent azimuthal amplitude variation in reflections from a fractured layer: 74th Annual International Meeting, SEG, Expanded Abstracts, 147-150.

Chopra, S., and K. J. Marfurt, 2007, Seismic attributes for prospect identification and reservoir characterization: Society of Exploration Geophysicists, Tulsa, OK, 456 p.

Goodway W., J. Varsek, and C. Abaco, 2006, Practical applications of P-wave AVO for unconventional gas Resource Plays-1 Seismic petrophysics and isotropic AVO: CSEG Recorder Special Edition 2006.

Hart, B. S., R. A. Pearson, and G. C. Rawling, 2002, 3-D seismic horizon-based approaches to fracture-swarm sweet spot definition in tight-gas reservoirs: The Leading Edge, **21**, 28-35.

Hunt, L., H., Hadley, S., Hadley, M., Downton, and J., Durrani, B., 2008, Interpolation, PSTM, AVO, and a thin gas charged Viking shoreface in west central Alberta, CSEG Annual Convention abstracts, 177-182.

Hunt, L., S. Reynolds, T. Brown, S. Hadley, H. Downton, and S. Chopra, 2010, Quantitative estimate of fracture density variations in the Nordegg with azimuthal AVO and curvature: a case study: The Leading Edge, **29**, 1122-1137.

Jenner, E., 2001, Azimuthal anisotropy of 3-D compressional wave seismic data, Weyburn field, Saskatchewan, Canada: Ph. D dissertation, Colorado School of Mines.

Liu, J., and K. J. Marfurt, 2007, Instantaneous spectral attributes to detect channels: Geophysics, **72**, 23–31.

Luo, M., and B. J. Evans, 2004, An amplitude-based multiazimuth approach to mapping fractures using P-wave 3D seismic data: Geophysics, **69**, 690-698.

Marfurt, K. J., and R. L. Kirlin, 2001, Narrow-band spectral analysis and thin-bed tuning: Geophysics, **66**, 1274-1283.

Nelson, R. A., 2001, Geologic Analysis of Naturally Fractured Reservoirs: Elsevier.

Nissen S. E., T. R. Carr, K. J. Marfurt, and E. C. Sullivan, 2009, Using 3-D seismic volumetric curvature attributes to identify fracture trends in a depleted Mississippian carbonate reservoir: implications for assessing candidates for CO_2 sequestration: AAPG studies in geology, **59**, 297-319.

Perez, G. and K. J. Marfurt, 2008, New azimuthal binning for improved delineation of faults and fractures: Geophysics, **73**, S7-S15.

Rich, J., 2008, Expanding the applicability of curvature attributes through clarification of ambiguities in derivation and terminology: 78th Annual International Meeting, SEG, Expanded Abstracts, 884-888.

Roende, H., C. Meeder, J. Allen, S. Peterson, and D. Eubanks, 2008, Estimating subsurface stress direction and intensity from subsurface full azimuth land data: 78th Annual International Meeting, SEG, Expanded Abstracts, 217-220.

Rüger, A., 1998, Variation of P-wave reflectivity with offset and azimuth in anisotropic media: Geophysics, **63**, 935-947.

Shuey, R. T., 1985, A simplification of the Zoeppritz equation: Geophysics, **50**, 609-614.

Sicking, C., S. Nelan and W. Mclain, 2007, 3D azimuthal imaging: 77th Annual International Meeting, SEG, Expanded Abstracts, 2364-2367.

Singh, P., 2008, Lithofacies and Sequence Stratigraphic Framework of the Barnett Shale, Northeast Texas: Unpublished PhD thesis, The University of Oklahoma, Norman, Oklahoma, 181 p.

Singleton, S., 2009, The effects of seismic data conditioning on prestack simultaneous impedance inversion: the Leading Edge, **28**, no. 7, 772-781.

Sudhakar, V., S. Chopra, G. Larsen, and H. Leong, 2000, New methodology for detection of faults and fractures: 70th Annual International Meeting, SEG, Expanded Abstracts, 635-638.

Thompson, A., J. Rich, and M. Ammerman, 2010a, Fracture characterization through the use of azimuthally sectored attribute volumes: 80th Annual International Meeting, SEG, Expanded Abstracts, 1433-1436.

Thompson, A., 2010b, Induced fracture detection in the Barnett Shale, Ft, Worth Basin, Texas: M.S. Thesis, the University of Oklahoma.

Thomsen, L., 1995, Elastic anisotropy due to aligned cracks in porous rock: Geophysical Prospecting, **43**, 805-829.

Treadgold, G., C. Sicking, V. Sublette, and G. Hoover, 2008, Azimuthal processing for fracture prediction and image improvement: CSEG recorder, **34**, no. 4, 38-41.

Xu, X., and I. Tsvankin, 2007, A case study of azimuthal AVO analysis with anisotropic spreading correction: the Leading Edge, **26**, 1552-1561.

Chapter 3: Quantitative correlation of fluid flow to curvature lineaments

Kui Zhang[1] , Yanxia Guo[1], Kurt J. Marfurt[1], and Susan E. Nissen[2]

[1] *University of Oklahoma, School of Geology and Geophysics,* [2] *Consultant, McLouth, Kansas*

Email: kui.zhang-1@ou.edu, Yanxia.Guo-1@ou.edu, kmarfurt@ou.edu, and nissen_susan@yahoo.com

Part of this work was presented in a paper at the 80th Annual Society of Exploration Geophysicists International Exposition meeting in Denver, Colorado, USA

SEG Expanded Abstracts 29, 1372-1376 (2010)

This paper will be submitted to GEOPHYSICS journal for publication.

Chapter 3: Quantitative correlation of fluid flow to curvature lineaments

Abstract

In most of unconventional reservoirs, open fractures provide critical fluid conduits, and the heterogeneous hydrocarbon production is highly dependent on the proximity of wells to these fractures. Attributes such as curvature do not "see" fractures; rather they are direct measures of real or apparent (due to conjugate faulting) folds and flexures that are associated with fractures through an appropriate tectonic model. In this study, we extend a previously-developed, interpreter intensive workflow to generate a suite of azimuthally-limited attribute volumes that can be directly correlated to production sensitive to fracture orientation and intensity. Specifically, we crosscorrelate the strength and strike of curvature lineaments to production based on the hypothesis that production will be a function of the well's distance to "fractures" correlated with curvature.

We validate this workflow on a 3D seismic survey acquired over a Mississippian supermature carbonate reservoir in Dickman Field, Ness County, Kansas that was previously interpreted by explicit hand correlation. After calibration of the hypothesized fluid flow based on the strength and strike of the most negative principal curvature, we find oil production increases with increasing distance from sealed NE-trending fractures while water production decreases with increasing distance from open NW-trending fractures. We also apply this workflow to a seismic survey over Woodford Shale in

Arkoma Basin, OK, and find that, oil and gas production increases with proximity to lineaments trending 30^o to 60^o and decreases with proximity to lineaments trending -30^o to 0^o.

Introduction

Fractures play a significant role in affecting reservoir performance. In conventional clastic or carbonate reservoirs with relatively good matrix porosity and permeability, open natural fractures can improve reservoir permeability allowing for higher production rate, while sealed fractures may provide a barrier to hydrocarbon flow in the rock matrix. In reservoirs with poor matrix characteristics, including tight gas sands, shales, or coalbed methane, open natural fractures or fissures may serve as an important hydrocarbon storage component and dominant fluid conduits, and heterogeneous hydrocarbon production is often directly related to the spatial distribution of fracture sweet spots. In unconventional reservoirs, sealed natural fractures can be popped-open during hydraulic fracturing, thereby directing energy away from virgin rock and reducing stimulation performance (Rich, 2008).

Although it has relatively low vertical and lateral resolution, 3D seismic data provides a means to map the spatial distribution of fractures and analyze the major fracture trends. Poststack geometric attributes derived from seismic data are often correlated with fracture "sweet" and "bitter" spots in shale players. For example, Johnson (2010) reported that greatly increased oil production is found in Bakken Shale sweet spots over bowl-shaped salt dissolution features in North Dakota. In contrast, the bowl-

shaped carbonate collapse features in the Ellenberger Limestone aquifer of the Fort Worth Basin (e.g. Sullivan et al., 2006) connect via fracture "bitter" spots with the overlying Barnett Shale, resulting in wells that produce only water.

Among all the attributes derived from poststack seismic amplitude data, volumetric curvature has proven to be one of the most promising attributes allowing us to map fractures and faults. Although the relationship between fractures and curvature lineaments is quite complicated, many studies have demonstrated that open fractures are correlated with strong structural deformation. Hart (2002) and Nelson (2001) showed that open fractures are related to flexures in tight sandstone reservoirs. Narhari et al. (2009) found a direct correlation between curvature and coherence lineaments and natural fractures seen in image logs. Arasu et al. (2010) used Schmidt diagrams to derive an ant-tracking algorithm to estimate fracture sweet spots of a given azimuth. Hunt et al. (2010) directly correlated natural fractures seen on horizontal image logs and induced fractures measured by microseismic experiments with AVAz, VVAz and curvature. Guo et al. (2010) observed that, the high producing wells in a Woodford Shale survey correlated with the structural lows given by most negative principal curvature k_2. Ideally, a full understanding of fracture distribution needs reconstruction of the deformation and subsequent strain field through geologic time. Indeed, Hennings et al. (2000) found that natural fractures measured on the outcropping Frontier Formation in the northern Rockies are highly correlated to both paleostrain estimated through palinspastic reconstruction and present-day curvature. Surprisingly, these two measures were poorly correlated with each other.

To our knowledge, one of the first attempts to correlate fluid flow with seismic volumetric curvature was made by Nissen et al. (2009). In their study of Dickman Field in Ness County, Kansas, they found the fluid flow to be closely related to the distance of the well to the nearest structural lineaments seen on most negative curvature maps. The water production decays as the distance to the NW-trending fracture lineament increases, indicating open fractures connected to the underlying aquifer. In contrast, oil production increases with the distance to the NE-trending fracture lineaments, indicating this fracture sets to be sealed, which is confirmed by nearby logs in horizontal wells. We generalize this idea by assuming: 1) the fluid production is a sum of fluid flow from all rather than the nearest fracture lineaments, and 2) the fracture intensity is proportional to the curvature value. Specifically, we generate a suite of azimuthally-limited attribute volumes that can be directly correlated with production to understand the contribution of fluid flow from fracture lineaments at every azimuth, thereby testing whether a given fracture set is open or closed.

We begin by describing our methodology to quantitatively correlate fluid flow to structural lineaments provided by curvature measures. Then, we apply this workflow to the previously-studied Mississippian carbonate reservoir in Kansas by Nissen (2009), and a gas shale reservoir in the Woodford Shale studied by Guo et al. (2010). We conclude with the suggestion that this workflow can be used to aid in proposing future well locations.

Methodology

Although three-dimensional seismic volumetric curvature attributes provide the opportunity to correlate subtle structural lineaments to fractures, most published curvature analysis for fracture delineation has been qualitative. Nissen et al. (2009) determined that fluid flow is not correlated to the curvature value seen at the well, but rather, associated with the proximity of the well to the nearest fracture lineament. Well log analysis of chert components indicated that fracture sets of different azimuths experienced different diagenetic alteration, leading them to postulate that fractures at one azimuth may be open, while those at another azimuth may be sealed, and should be treated differently. Unfortunately, this approach suffers from two pitfalls: 1) it needs extensive manual picking, and 2) it only accounts for the contribution of fluid flow from the nearest lineament. Our objective is to generate a suite of 3D azimuthally-limited "fracture intensity" volumes that can then be directly correlated to production without picking. For a specific location, all the close-by fracture-related lineaments are considered to contribute to the fluid flow.

The diagram in Figure 3-1 shows the fluid flow at one well location. The fluid flow is approximately a function of κ/r, κ is permeability and r is distance from well to the fracture lineament. If the joint or fracture plane is open, κ takes a very large value, while if it is sealed, κ approaches to zero. Using the theory of calculus and assuming linear systems, a fluid charged fracture would provide a response proportional to the sum of a line of equally-spaced fluid injectors along the fracture. There are several steps necessary to generate an azimuthally-limited fracture intensity map. For our two examples, both of which are associated with joints and diagenetic alteration of either Mississippian limestone (for Kansas) or the underlying Hunton limestone (for the

Woodford Shale in Oklahoma), the lineaments of interest are delineated by the most negative principal curvature, k_2. The strike of these lineaments is the azimuth of maximum curvature, when $|k_2|>|k_1|$, and the azimuth of minimum curvature when $|k_2|\leq|k_1|$, where k_1 is the most positive principal curvature, and the azimuths of these two curvatures are given by Rich (2008). Next, these lineaments are loaded into the workstation and the interpreter adjusts a gray-scale color bar to highlight features hypothesized to be associated with fractures. We use a very simple display based on a lower threshold, k_{lower}, and an upper threshold, k_{upper}, resulting in a color bar and "fracture intensities" shown in Figure 3-8. Curvature values less than k_{lower} are set to black and assigned a weight of 1.0. Curvature values greater than k_{upper} are set to white and assigned a weight of 0.0 . Intermediate values are assigned linearly interpolated shades of gray and corresponding weights.

The previous process results in a skeletonized image of fracture lineaments. At this point, we have two means of smoothing. The most common one is to convolve the skeletonized lineaments with a Gaussian operator, which can be efficiently achieved through iterative five- or nine-point smoothing. Another means is that, based on statistical correlation made by Nissen et al. (2009) and the fact that the Green's function for fluid flow in or out of a vertical well (fault pillar) in a flat layers is simply $1/r$, where r is the radial distance $r=(x^2+y^2)^{1/2}$, we can convolve our skeletonized fracture lineaments with the impulse response $1/r$. Figure 3-3 describes the workflow used to generate azimuthally-limited hypothesized fluid flow volumes that can be used directly to correlate with production. The impulse response of our azimuth filters is shown in Figure 3-2.

Application in Dickman survey, Kansas, USA

Dickman Field is an old Mississippian carbonate reservoir locating to the west of the Central Kansas Uplift in Ness County, Kansas (Figure 3-4). Discovered in 1962, Dickman Field has since produced approximately 1.7 million barrels of oil. The target Mississipian formation consists of shallow-shelf carbonates unconformably overlain by the pre-Pennsylvanian Shale of the Cherokee Group which serves as the seal. The reservoir has a very strong bottom water drive by the Western Interior Plains aquifer system, making it a perfect candidate to study CO_2 sequestration. Immediately underlain by the aquifer system is the tight Gilmore City limestone with low porosity and permeability, providing the barrier to the water flow. According to previous studies (Goebel, 1966; Nodine-Zeller, 1981; Nissen et al., 2009), Mississippian carbonate reservoir rocks in Dickman Field generally contain solution-enhanced fractures. Some of these fractures were subsequently filled by Pennsylvanian Shale, acting as barriers of fluid flow. Others may be opened by some geologic processes, thereby serving as fluid conduits.

The seismic survey (Figure 3-5b) under our study covers a larger area than the one studied by Nissen et al. (2009) shown in Figure 3-5a, which allows to make a broader interpretation of the fracture distribution. Figure 3-6a shows the time-structure map of the top of Gilmore City horizon underlying the Mississippian aquifer. Figures 3-6b and 3-6c show representative vertical seismic lines AA' and BB', where yellow arrows indicate collapse features. In Dickman Field, Nissen et al. (2009) found the fractures give rise to

most negative curvature lineaments; the exact cause is uncertain, though diagenetic alteration and subsequent infilling with the overlying lower Cherokee Shale is a major component. In Figure 3-7, we display horizon slices along the Gilmore City through most negative principal curvature k_2. A simple gray scale color bar is applied with pure black corresponding to a value of k_2=-0.002, and pure white to k_2=+0.002. Corresponding colors are linearly interpolated between the minimum and maximum values such that pure gray corresponds to a value of k_2=0.0. According to this map, the majority of lineaments align along NE-SW direction, while some lineaments align along NW-SE direction.

Figure 3-8 shows "Skeletonized" image obtained by interactively adjusting the color bar to delineate features interpreted to be associated with fractures. k_{lower} and k_{upper} are used to assign weights. Figure 3-9 shows the strike of the most negative principal curvature k_2 modulated by its strength, which allows definition of fracture sets from different azimuths. Figure 3-10 is the 3D visualization of the same co-rendered volume using transparency display. Note that the solution-enhanced fractures in Mississippian have quite good vertical continuity, and thereby mapping of fracture lineaments on Gilmore City is sufficient to help us to understand the fracture patterns through the entire Mississippian interval.

Nissen et al. (2009) correlated the 5-year oil and water production against the distance to the nearest interpreted lineaments along NE-SW and NW-SE respectively. Figure 3-11a shows the interpreted lineaments from the superimposed most negative curvature maps of top and bottom of Mississippian. In Figure 3-11b, oil production is plotted against the distance of the wells to the NE lineaments and NW lineaments. In

Figure 3-11c, water production is plotted against the distance to those lineaments. From these cross-plots, we see the NE-trending fracture related lineaments seem to be sealed, providing a barrier to the oil flow, while there is no identifiable correlation between oil production and distance to the NW-trending lineaments. In contrast, the good correlation between water production and distance to NW-trending fracture-related lineaments suggest that the NW-trending fractures may be open extending into the underlying aquifer.

We generated twelve azimuthally-limited hypothesized fluid flow maps from the most negative principal k_2 and its strike with an azimuthal increment of 15^o with the goal of reproducing the correlation between 5-year oil production, water production, and fracture azimuth described by Nissen et al. (2009). Figure 3-12 shows these azimuthally-limited maps with oil production bubbles. Bubble size represents relative oil production. We see the map generated from fracture lineaments with azimuth 45^o has the largest negative cross-correlation, which implies the fractures in NE-trending might be shale-filled, forming a barrier to oil flow through rock matrix. Figure 3-13 shows correlation between the same twelve maps with water production. This time, the hypothesized fluid flow generated from fracture-related lineaments with 135^o has the strongest correlation, which means fractures at 135^o (NW-SE) might to be open, which channel the water from underlying aquifer. Figure 3-14 clearly shows the cross-correlation between oil production, water production with fracture lineaments from different azimuths. The two observations we made here is consistent with the conclusions drawn by Nissen et al. (2009), which validate the feasibility of the proposed calibration approach.

Application in Woodford Shale survey

Since last decade, the Woodford Shale play has become one of the most promising unconventional resources in USA, holding a huge accumulation of gas and oil. With the introduction of successful horizontal drilling, extensively fractured Woodford wells can produce over 10 million cubic feet of gas in the first week. The Woodford Shale is a thick, deep-marine, organic-rich, fissile black shale deposited during later Devonian to early Mississippian, making it a good source rock. Natural fractures and hydraulically induced fractures serve as key fluid conduits for the economic gas production in the play.

The seismic survey under study lies at the western end of the Arkoma Basin, with an overall area of 160 mi^2. The Arkoma Basin covers portions of west-central Arkansas and southeastern Oklahoma with an area of approximate 33800 mi^2. The basin is bounded on the north by the Ozark Uplift in Arkansas, and the Cherokee Platform in Oklahoma, and on the southwest and south by the Arbuckle Uplift and the Quachita Fold and Thrust Belt (Figure 3-15a). Figure 3-15b depicts the stratigraphic column of the Arkoma Basin (Portas, 2009), with the Woodford Shale overlying the Hunton Limestone.

Figure 3-16 shows the composite image of time-structure and most negative principal curvature k_2 through the Woodford horizon. Yellow arrow indicates a strong wrench fault. In Figure 3-17, we project the gas and oil production onto three measures: (a) coherence, (c) most positive principal curvature k_1, and (e) most negative principal curvature k_2. Figures 3-17b, d, and f provide close-up views of the high-producing north end of the survey. Red and green bubbles represent gas and oil production respectively,

where bubble size represents the gross revenue of the first 90 days of those wells calculated using \$4/*MCF* (thousand cubic feet) for gas and \$80/barrel for oil. We visually correlate the majority of high producing wells to structural-low regions delineated by most negative principal curvature. The use of oil-based muds precludes the use of image logs, but we hypothesize they correlate to joints that continue into the Hunton Limestone, giving rise to the structure lows. Figure 3-18 shows the rose diagram along the Woodford which basically tells us that the lineaments have two dominant orientations: NE and NW.

In Figure 3-19, we generate six azimuthally-limited maps at 30^o increments from k_2 and its azimuth along Woodford horizon to calibrate with gas and oil production in an attempt to determine which fracture set, if any, correlates to better or worse production. These results indicate that improved production is strongly correlated with the fractures, as evidenced by the positive correlation of production and the hypothesized fracture fluid flow at azimuth 30^o and 60^o. Figure 3-20 shows the spreadsheet for calculation of cross-correlation coefficient, and the bar plot giving the cross-correlation coefficient as a function of azimuth.

Discussions and conclusions

We develop a new workflow to quantitatively correlate the fracture-related curvature lineaments from different azimuths to the production data. This approach hypothesizes that, open natural fractures or closed fractures that are easily popped open by the hydraulic fracture program act as the dominant fluid conduits in the reservoir. Assuming one fracture composed of a set of point fluid injectors, we can predict the

hypothesized fracture “fluid flow” from different azimuths through integration of the contribution from all point fluid injectors. Compared with the approach proposed by Nissen et al. (2009), the workflow avoids the intensive manual picking of the distance from the well to the nearest lineament. In addition, we consider the contribution of fluid flow from all rather than the nearest fracture lineaments around the well, which is more physically plausible.

We demonstrate that this workflow can be employed to investigate the fracture characteristics (open or sealed) by applying it to a carbonate Field in Kansas and a Woodford Shale survey in Arkoma Basin. We believe that such statistically significant correlations based on the workflow introduced in this paper can result in a more efficient drilling program.

Acknowledgements

Thanks to Mull Drilling, Pablo LLC, BP, and CGG-Veritas for providing the data and authorization to publish this work. Initial inspiration for this approach followed brainstorming sessions with Austin Vander Hoya and Kevin Woller of Pioneer Resources. The Dickman analysis was built on interpretation made by Rachel Barber. Finally, we thank the industry sponsors of the University of Oklahoma Attribute-Assisted Seismic Processing and Interpretation (AASPI) Consortium for financial support.

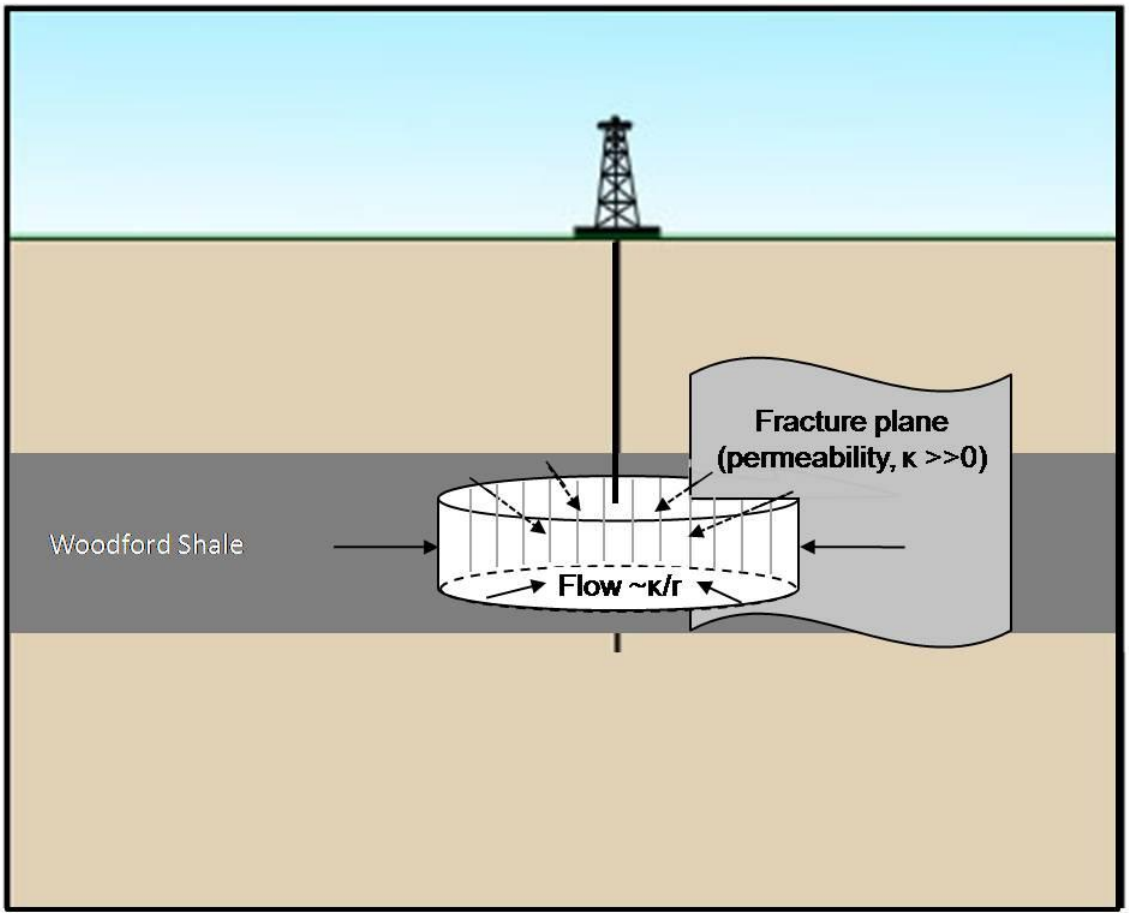

Figure 3-1. Diagram showing the fluid flow of a well controlled by the finite permeability of the layer κ, and the proximity to a highly permeable joint or fracture. We hypothesize that κ is large for open fractures, and close to zero for sealed fractures.

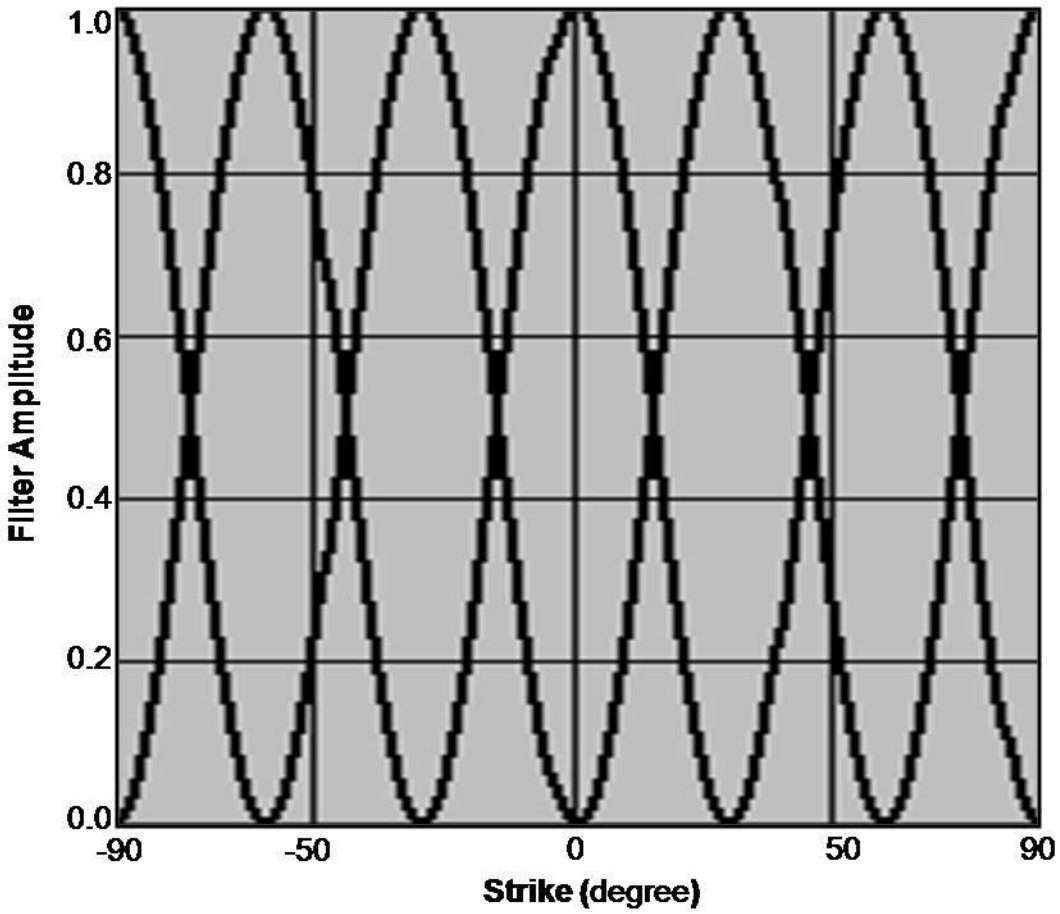

Figure 3-2. Impulse responses of a suite of azimuthal filters.

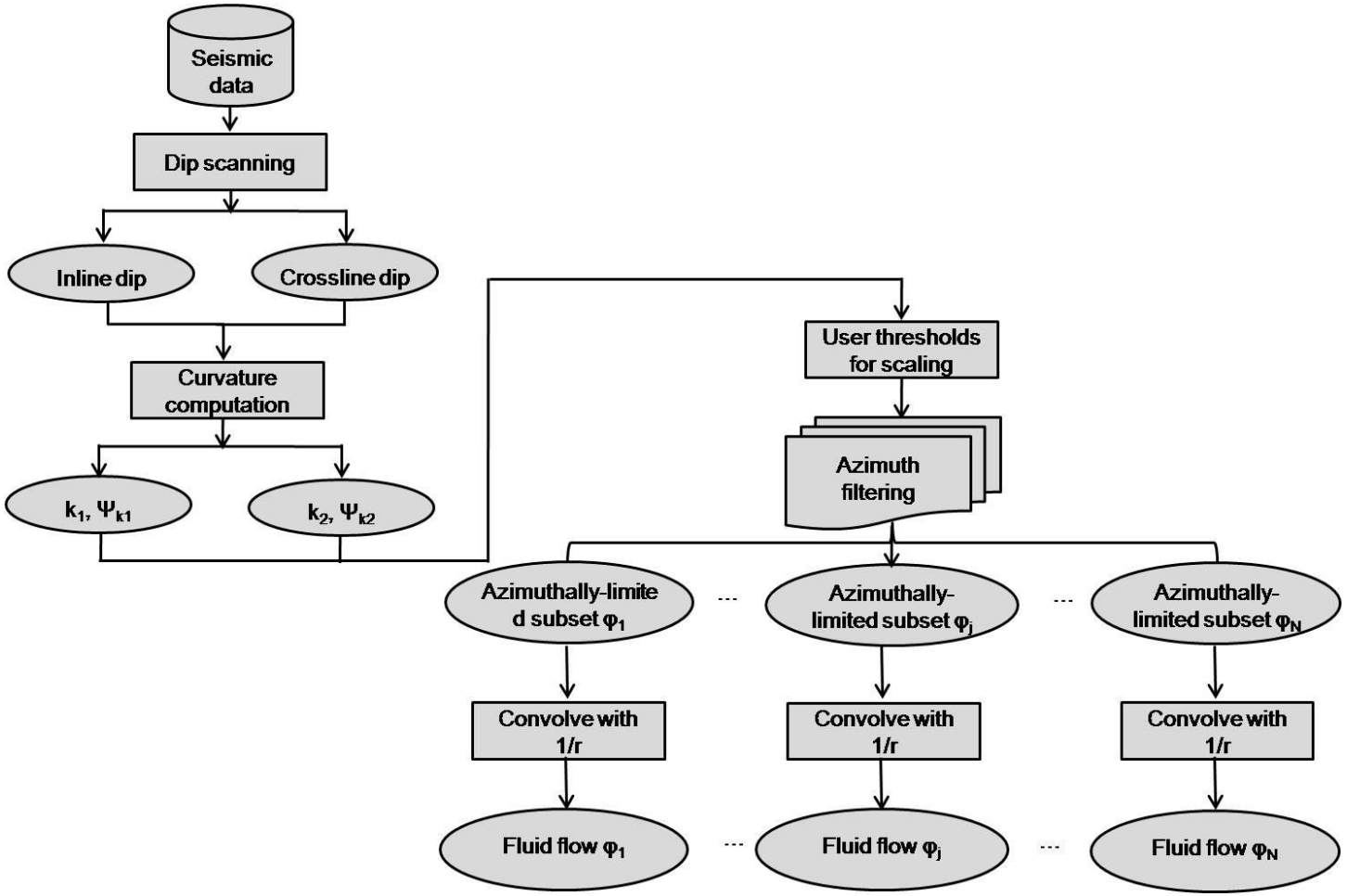

Figure 3-3. The workflow for calculation of "fluid flow" based on hypothesized equally-spaced "injectors" distributed along each fracture set.

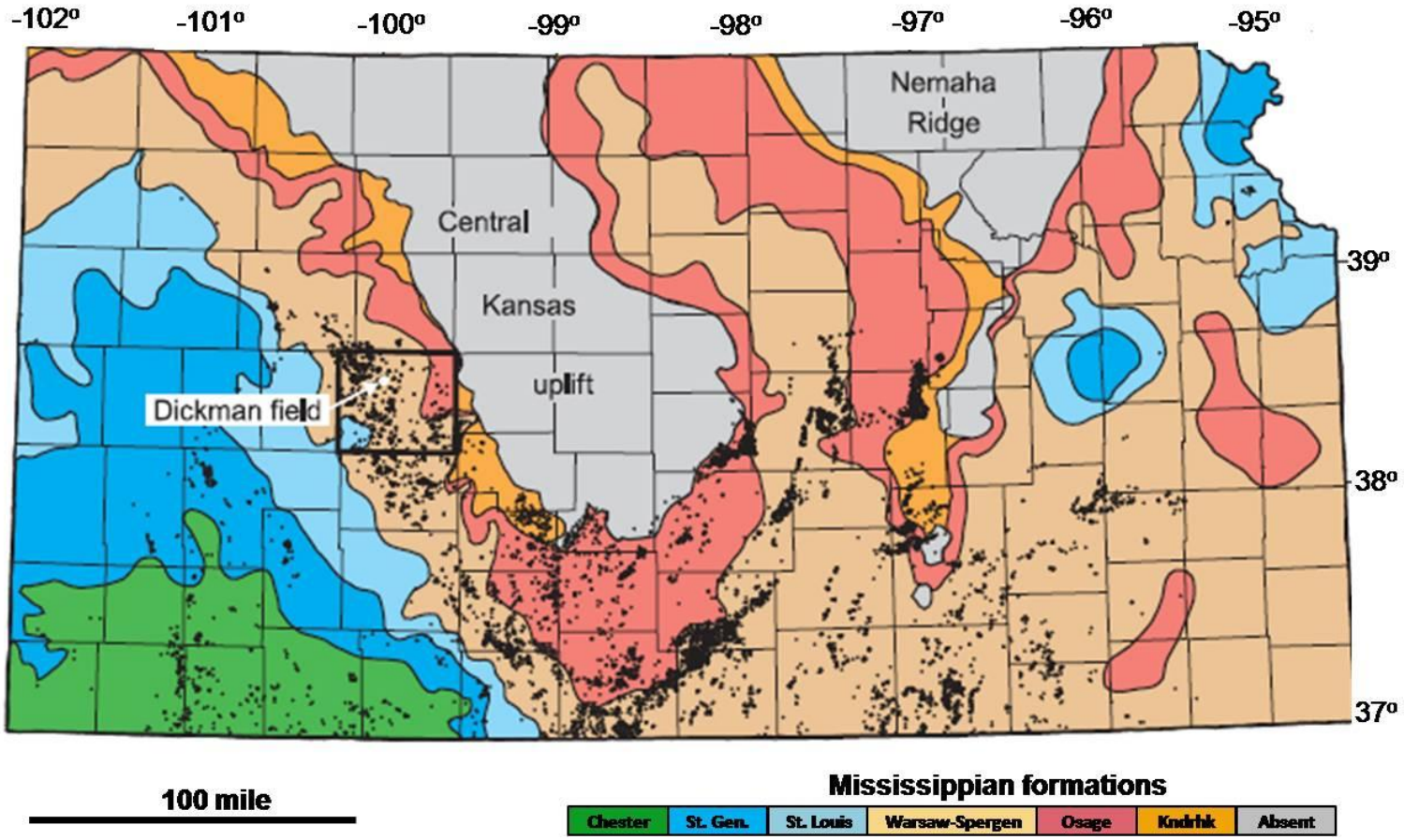

Figure 3-4. Map of the Mississippian subcrop in Kansas. Black box outlines Ness County, and white arrow points to the location of Dickman Field. Black dots represent oil production. Colors represent different formations. (from Nissen et al., 2009)

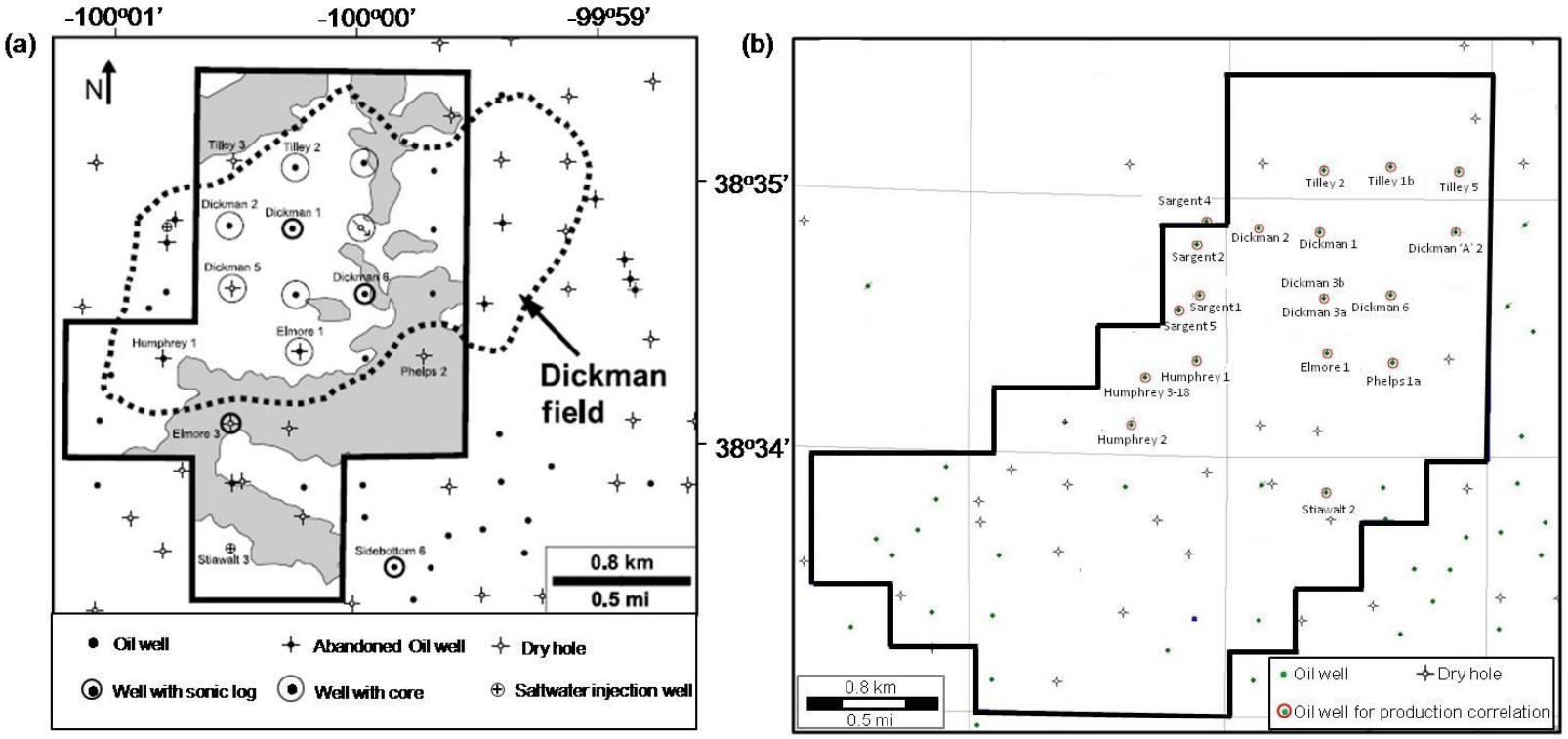

Figure 3-5. Maps of (a) the seismic survey studied by Nissen et al. (2009), and (b) a somewhat larger merged survey used in our study. The heavy black outline shows the extent of the two surveys. The grey areas indicate the top of Mississippian below the interpreted oil-water contact.

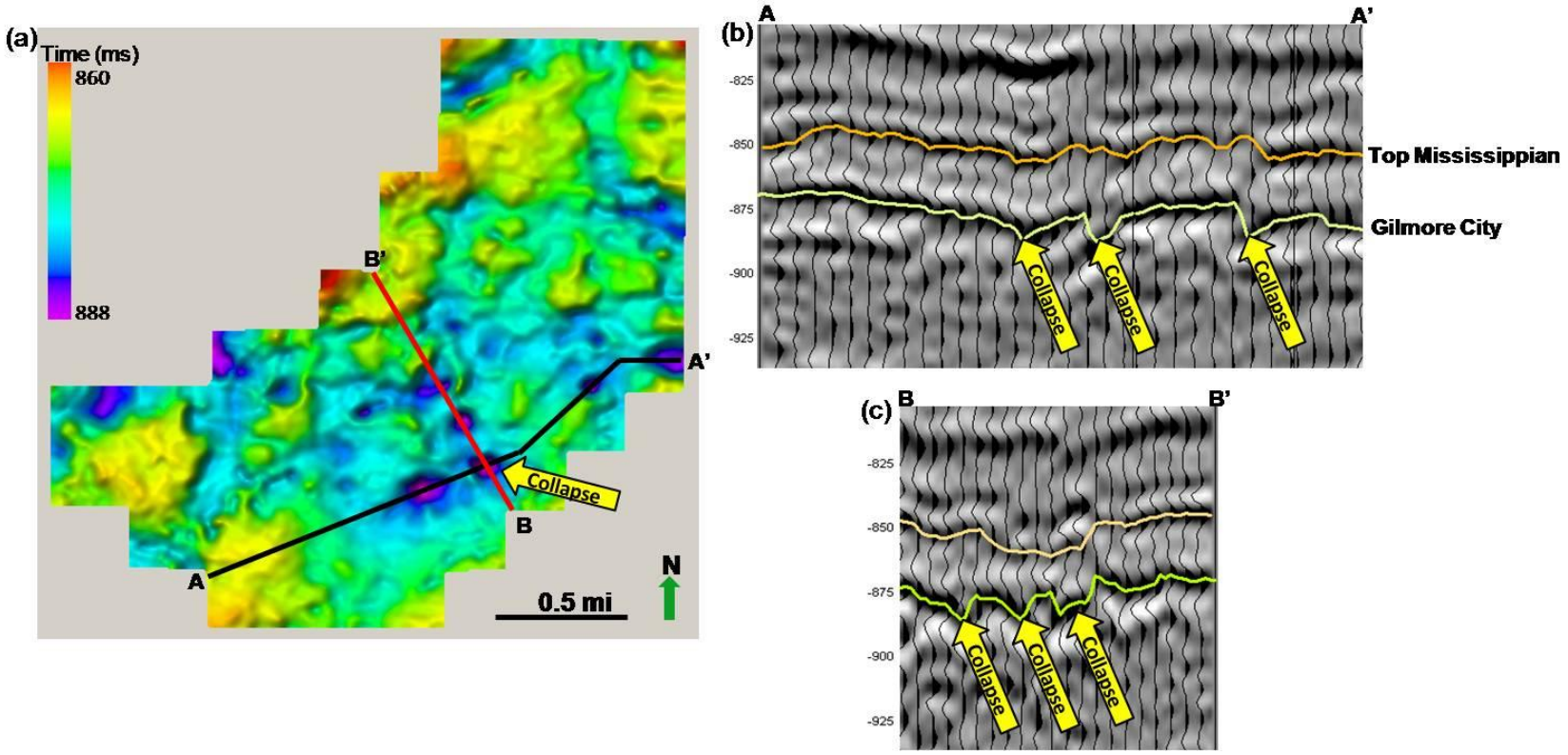

Figure 3-6. (a) Shaded relief time-structure map of the top of Gilmore City horizon underlying Mississippian reservoir, and two representative seismic lines (b) AA', and (c) BB', showing data quality. Yellow arrows indicate possible collapsed features?

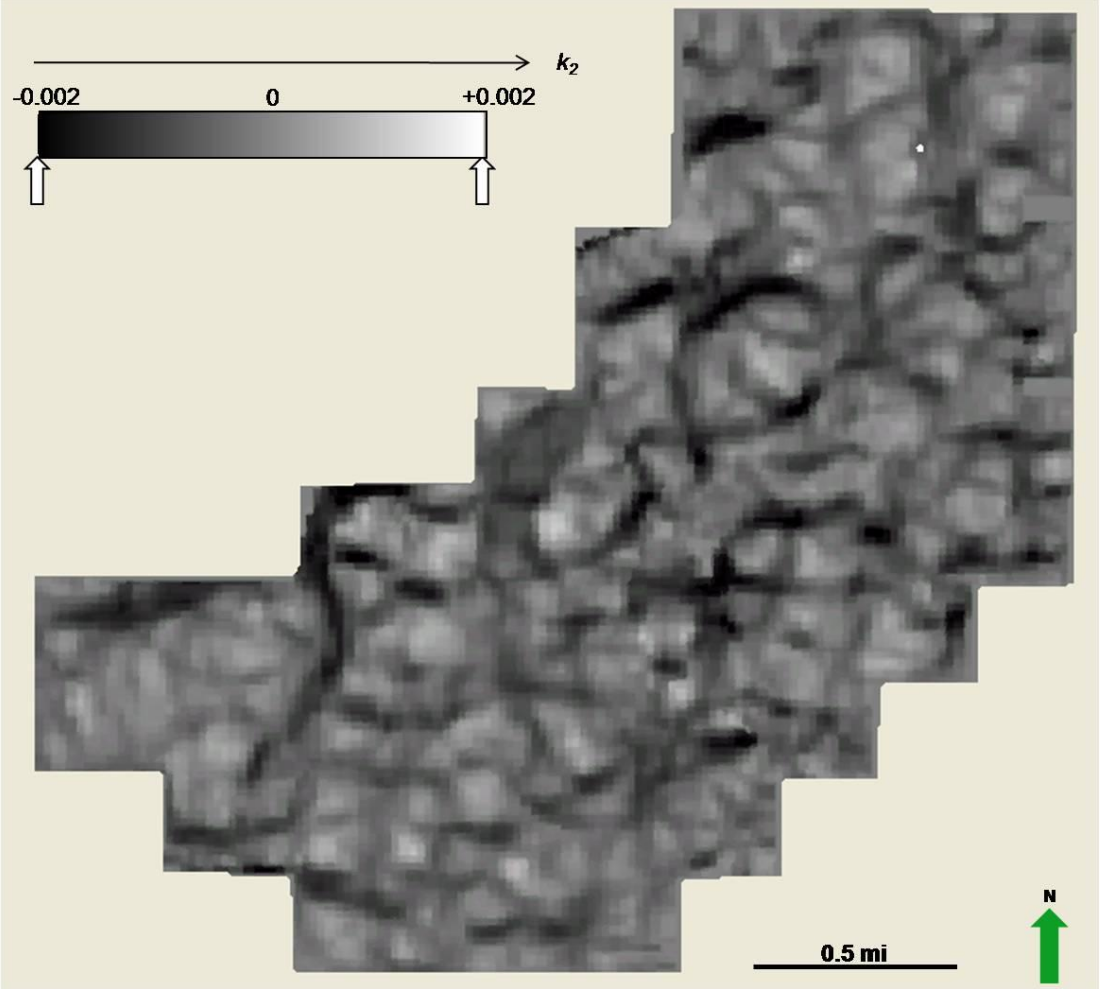

Figure 3-7. Horizon slice through the Gilmore City showing most negative structural curvature, k_2. A simple gray scale color bar is applied with pure black corresponding to a value of k_2=-0.002, and pure white to k_2=+0.002. Corresponding colors are linearly interpolated between the minimum and maximum values such that pure gray corresponds to a value of k_2=0.0.

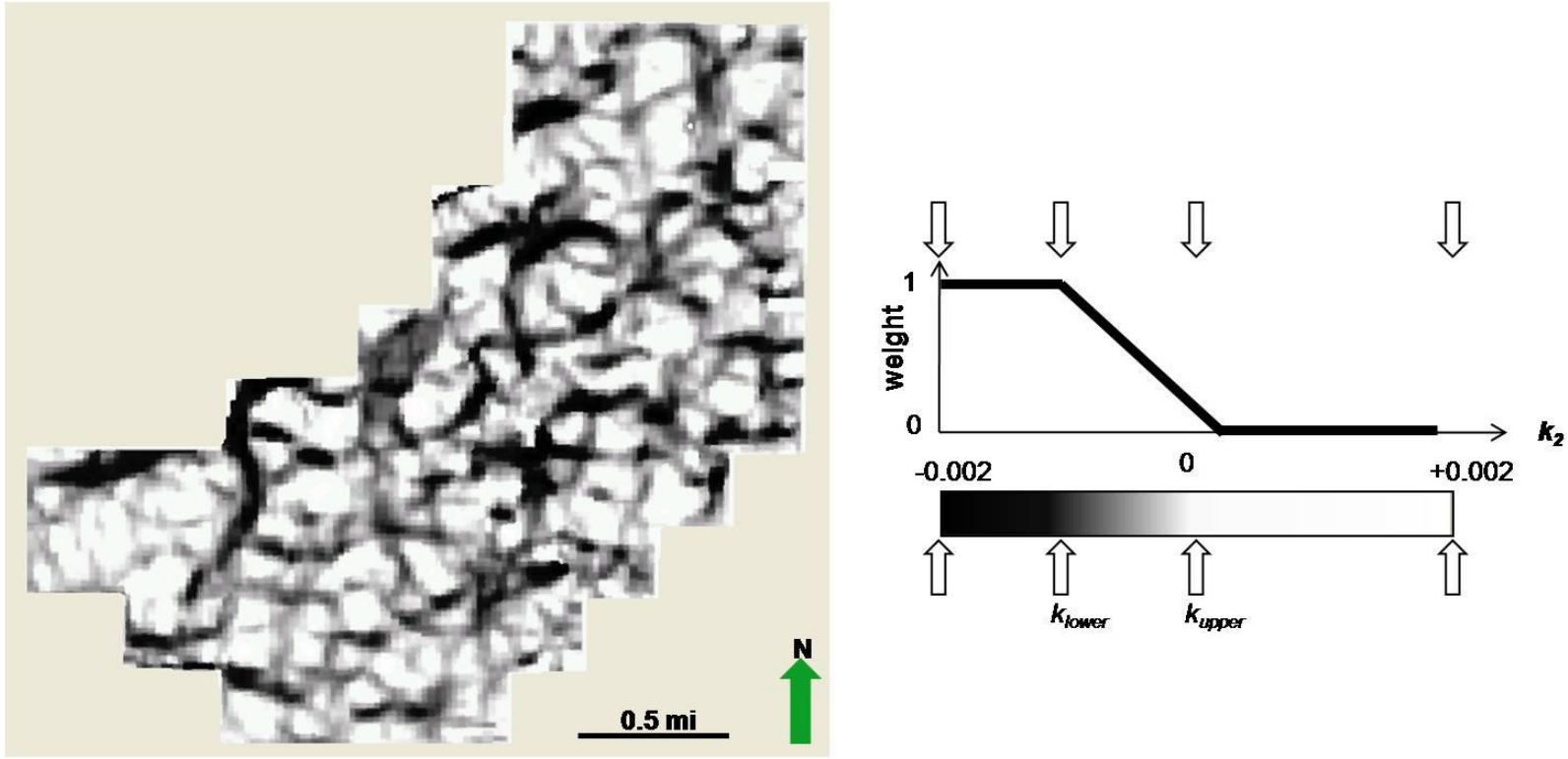

Figure 3-8. “Skeletonized” image obtained by interactively adjusting the color bar to delineate features interpreted to be associated with fractures. Curvature values less than k_{lower} are set to black and assigned a weight of 1.0. Curvature values greater than k_{upper} are set to white and assigned a weight of 0.0. Intermediate values are assigned linearly interpolated shades of gray and corresponding weights.

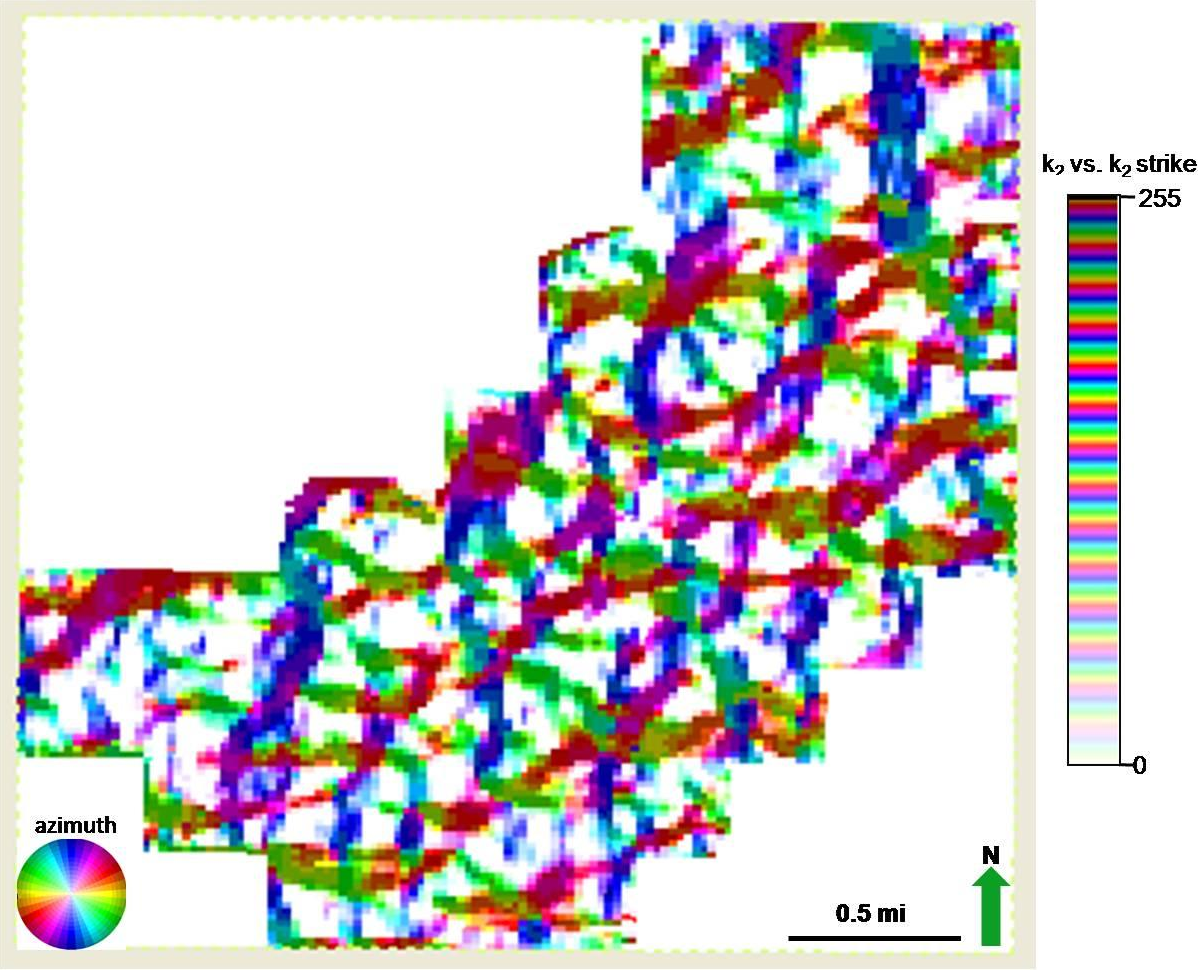

Figure 3-9. Co-rendered volume from most negative structural curvature k_2 and strike of k_2 which allows definition of "fracture" sets having different azimuths.

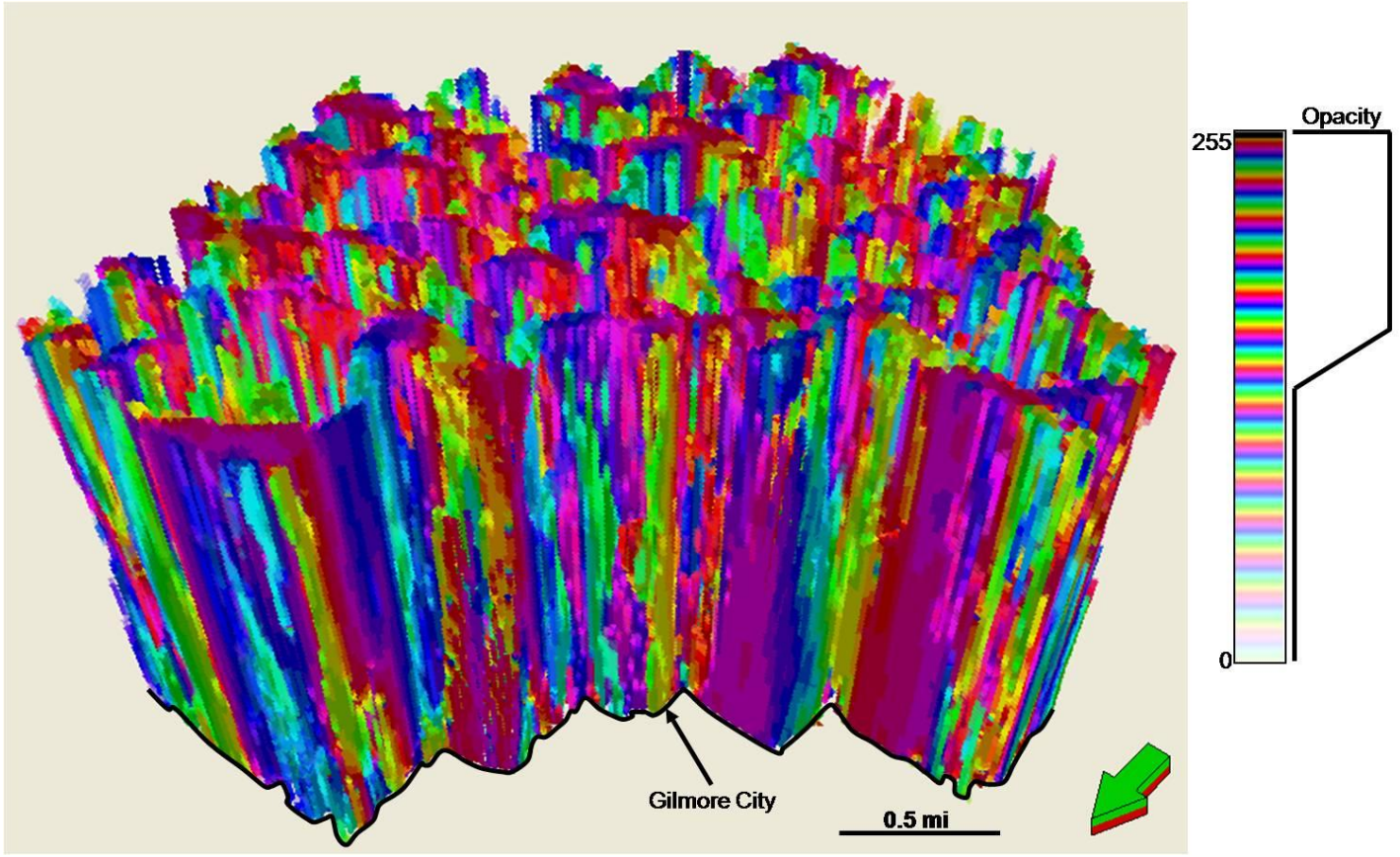

Figure 3-10. 3D view of the co-rendered volume from k_2 and strike of k_2. The solution-enhanced fractures in Mississippian have good vertical continuity, and thereby interpretation of fracture lineaments on Gilmore City is sufficient to map the fracture patterns through the entire Mississippian interval.

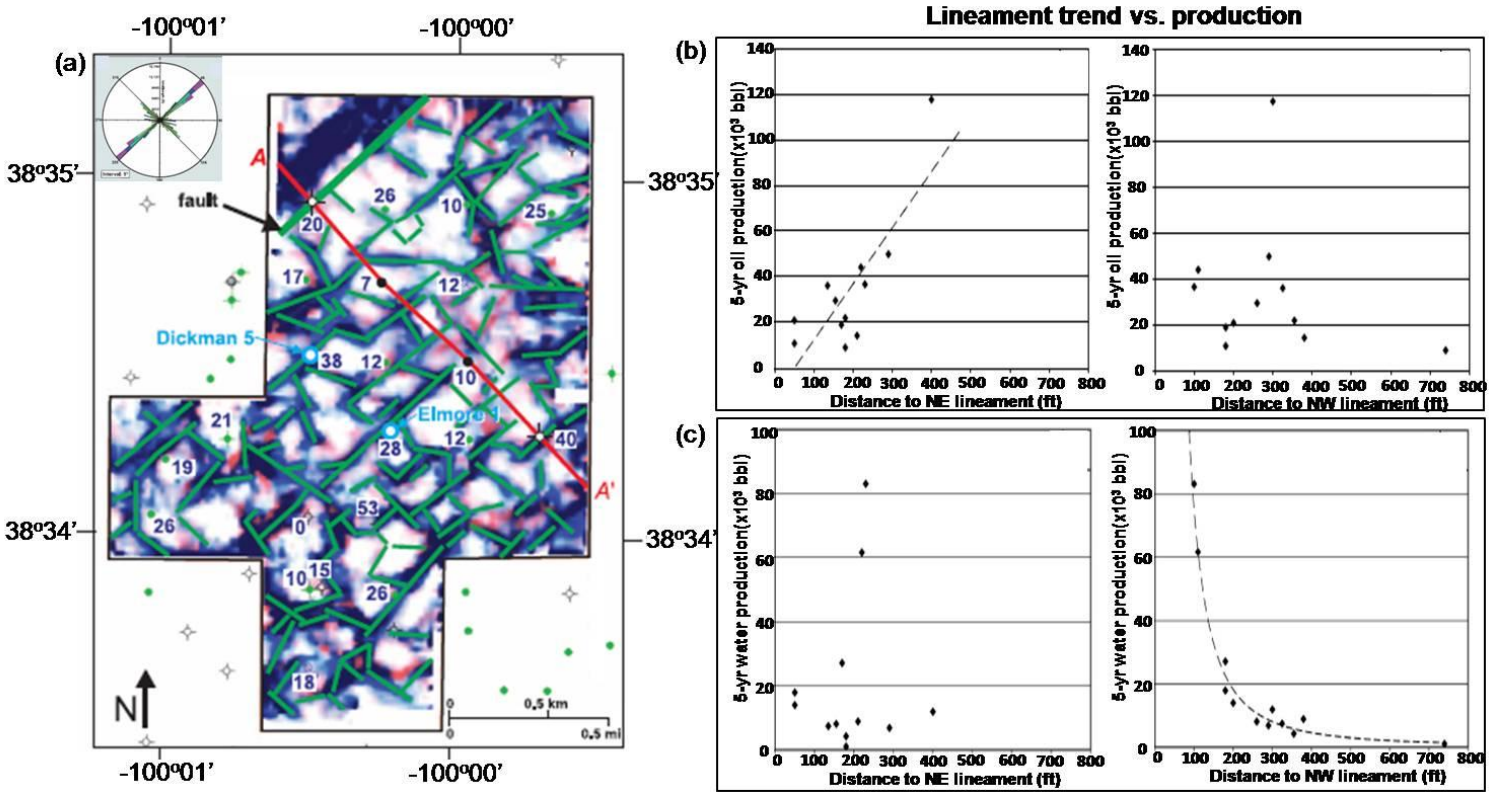

Figure 3-11. Superimposed most negative curvature maps from top and bottom of Mississippian with the fracture lineaments interpreted (a). (b) and (c) are 5-year oil and water production against distance to lineaments from different azimuths. A linear relationship between oil production and distance to NE lineaments exists, and a non-linear correlation between water production and distance to NW lineaments exists. (after Nissen et al., 2009)

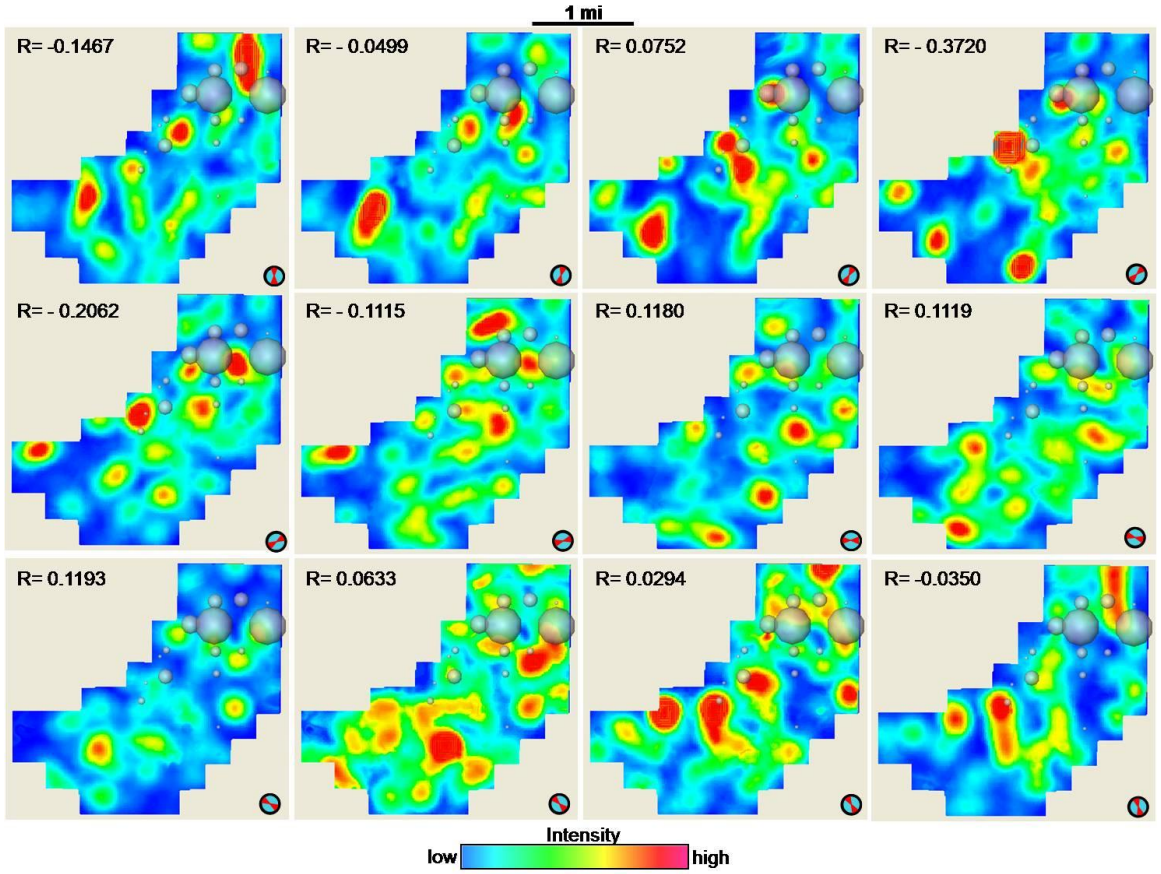

Figure 3-12. 5-year oil production against hypothesized fracture fluid flow computed from k_2 curvature and its strike. The strongest negative correlation at azimuth 45^{o} and 60^{o} suggests the NE-SW trending fractures might be sealed, acting as the barrier to the fluid flow. This is consistent with the work by Nissen et al. (2009). Bubble size represents relative oil production.

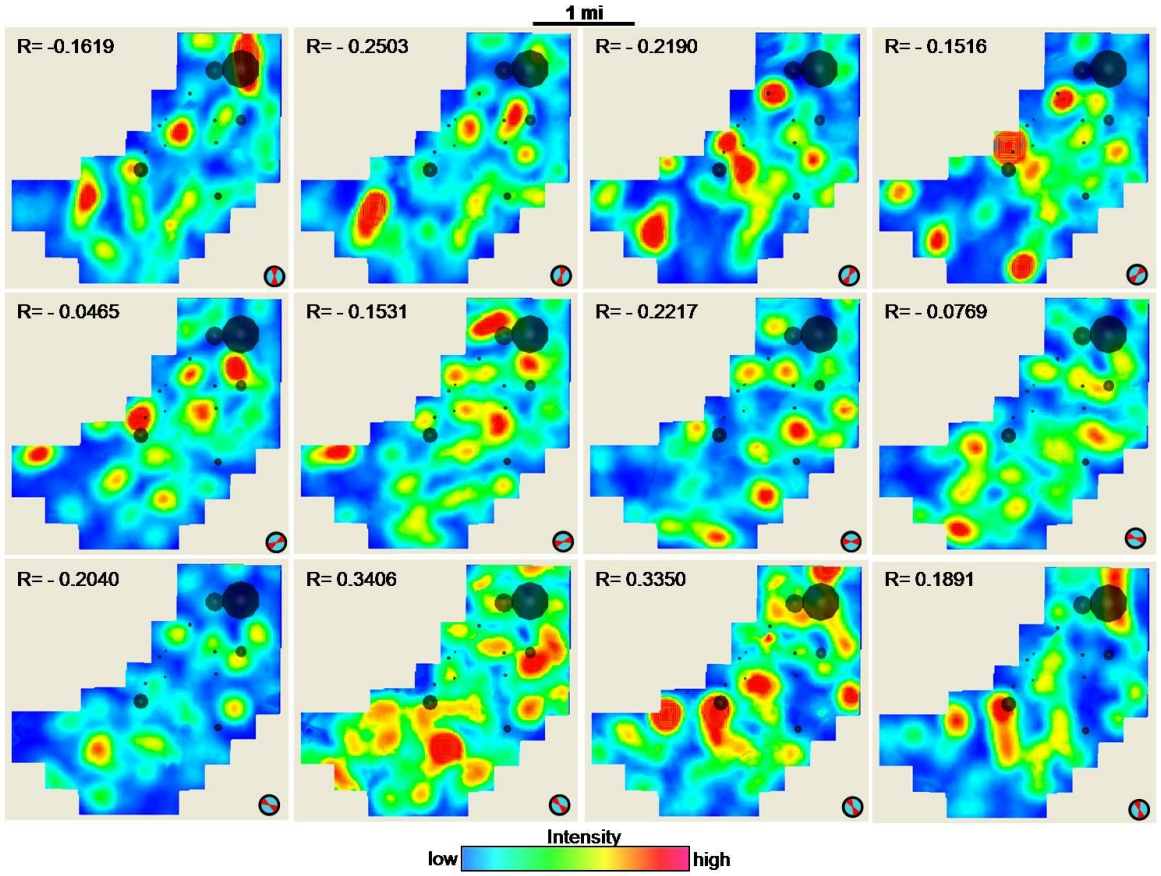

Figure 3-13. 5-year water production against hypothesized fracture fluid flow computed from k_2 curvature and k_2 strike. The strongest positive correlation at -45^{o} suggests that NW-SE-trending fractures are open, corroborated by the work from Nissen et al. (2009). Bubble size represents relative water production.

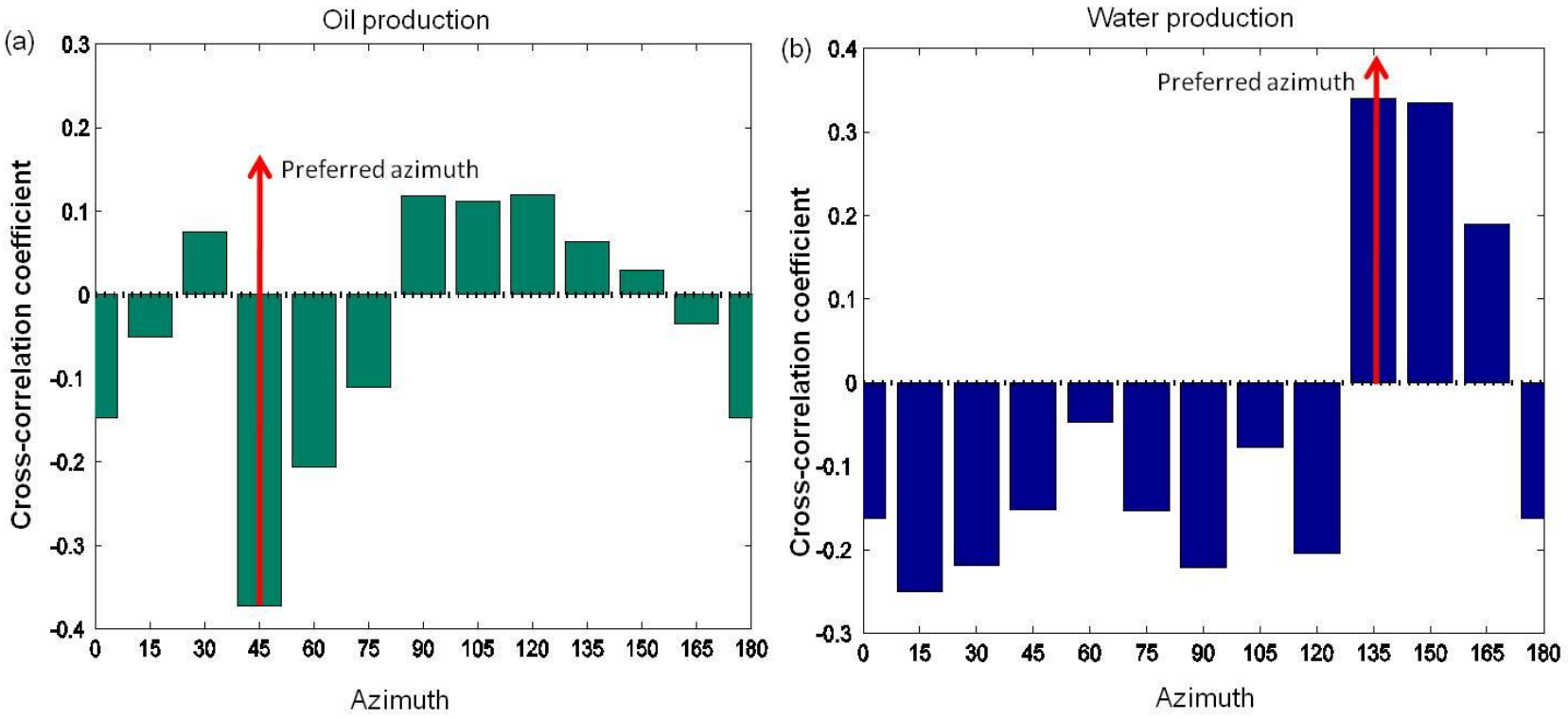

Figure 3-14. Cross-correlation of oil production (a), water production (b) with the hypothesized fluid flow from different azimuths. The strong negative coefficient at NE 45^{o} implies that the NE lineaments are sealed, while the strong positive correlation at NW 45^{o} implies that the NW trending fractures are open.

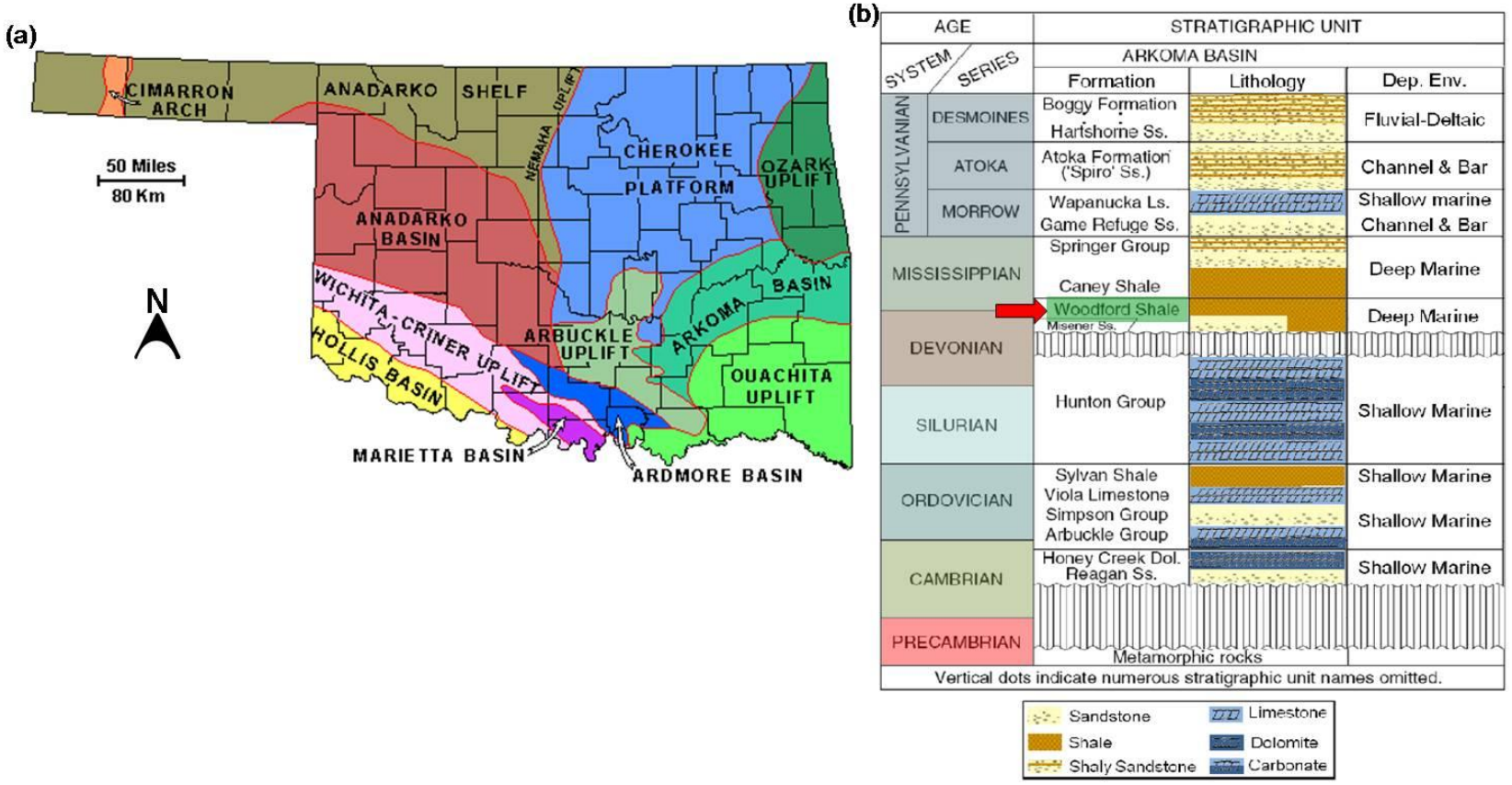

Figure 3-15. Major geologic provinces of Oklahoma (a) (after Northcutt and Campbell, 1995), and (b) stratigraphic column of Arkoma Basin (Portas, 2009). Red arrow points to Woodford Shale.

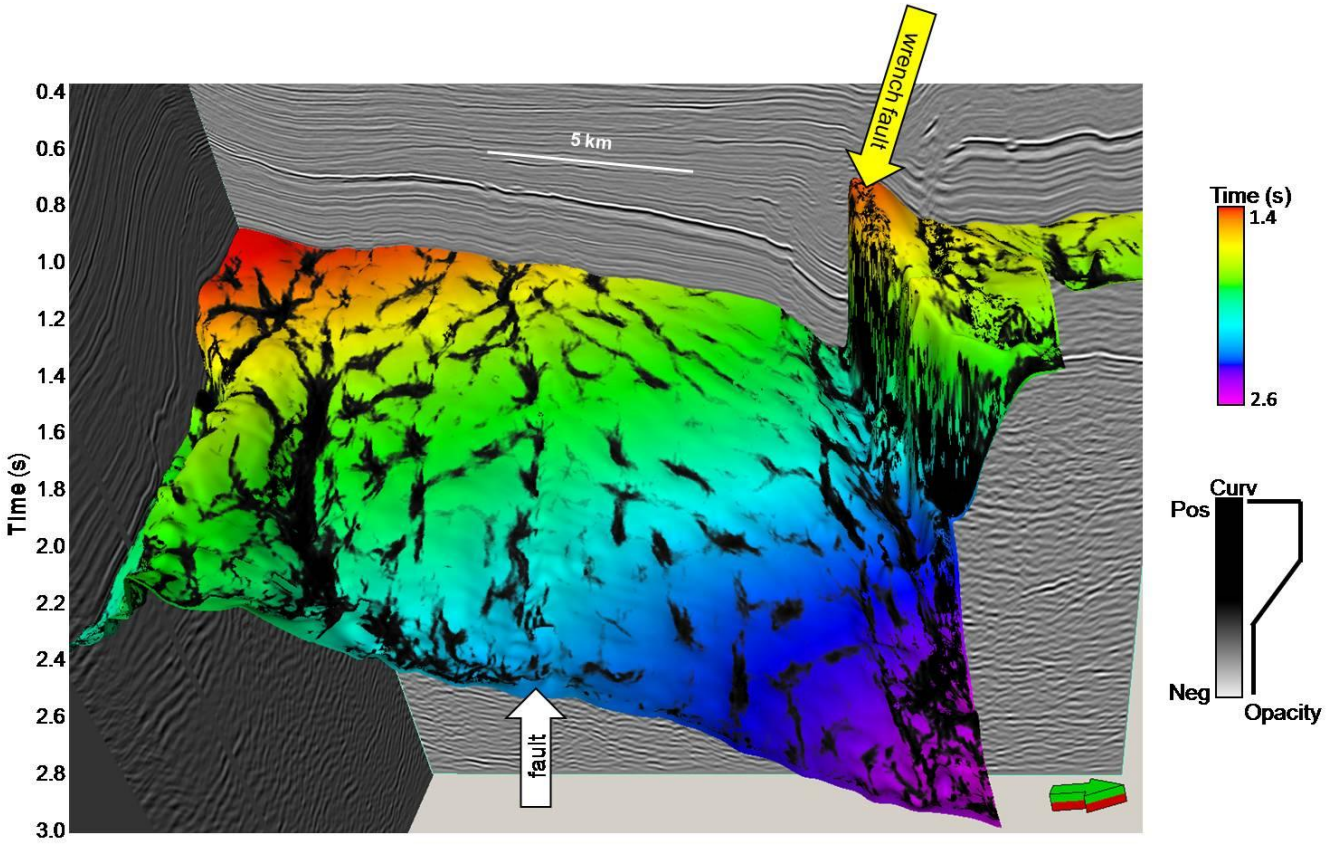

Figure 3-16. Blended image from time-structure map and most negative principal curvature k_2 through the top Woodford horizon (Seismic data courtesy of CGG-Veritas). Dark color indicates structural lows. Yellow arrow denotes a west-east wrench fault. White arrow denotes another fault which downthrown side shows as a valley.

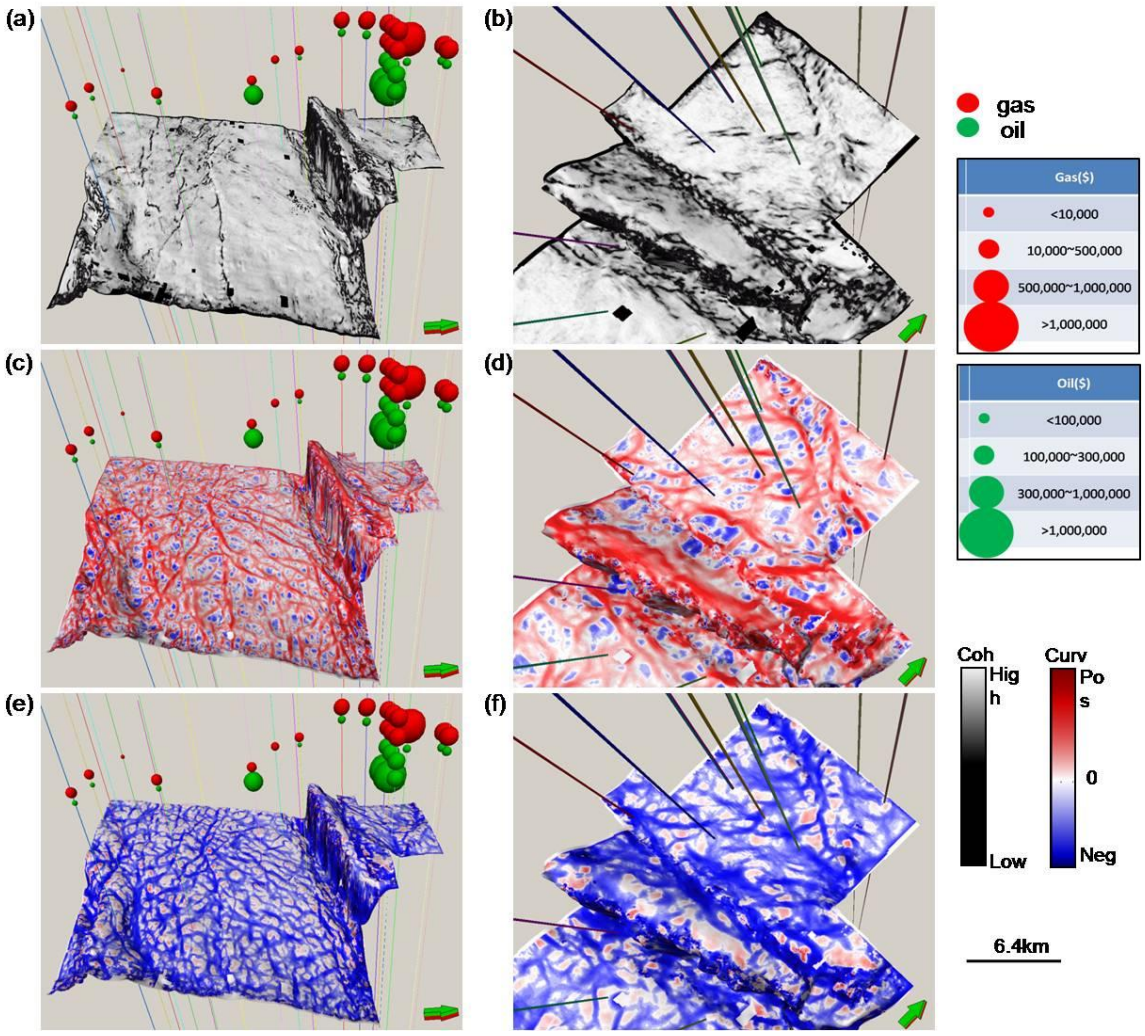

Figure 3-17. Horizon slices through (a) coherence, (c) most positive curvature k_1 and (e) most negative curvature k_2 vs. well location and production. (b), (d), and (f): close up view of the high-production area from (a), (c), and (e) respectively. The bubbles represent the gross revenue of the first 90 days of those wells. We see majority of high producing wells locates at lineaments with most negative curvature.

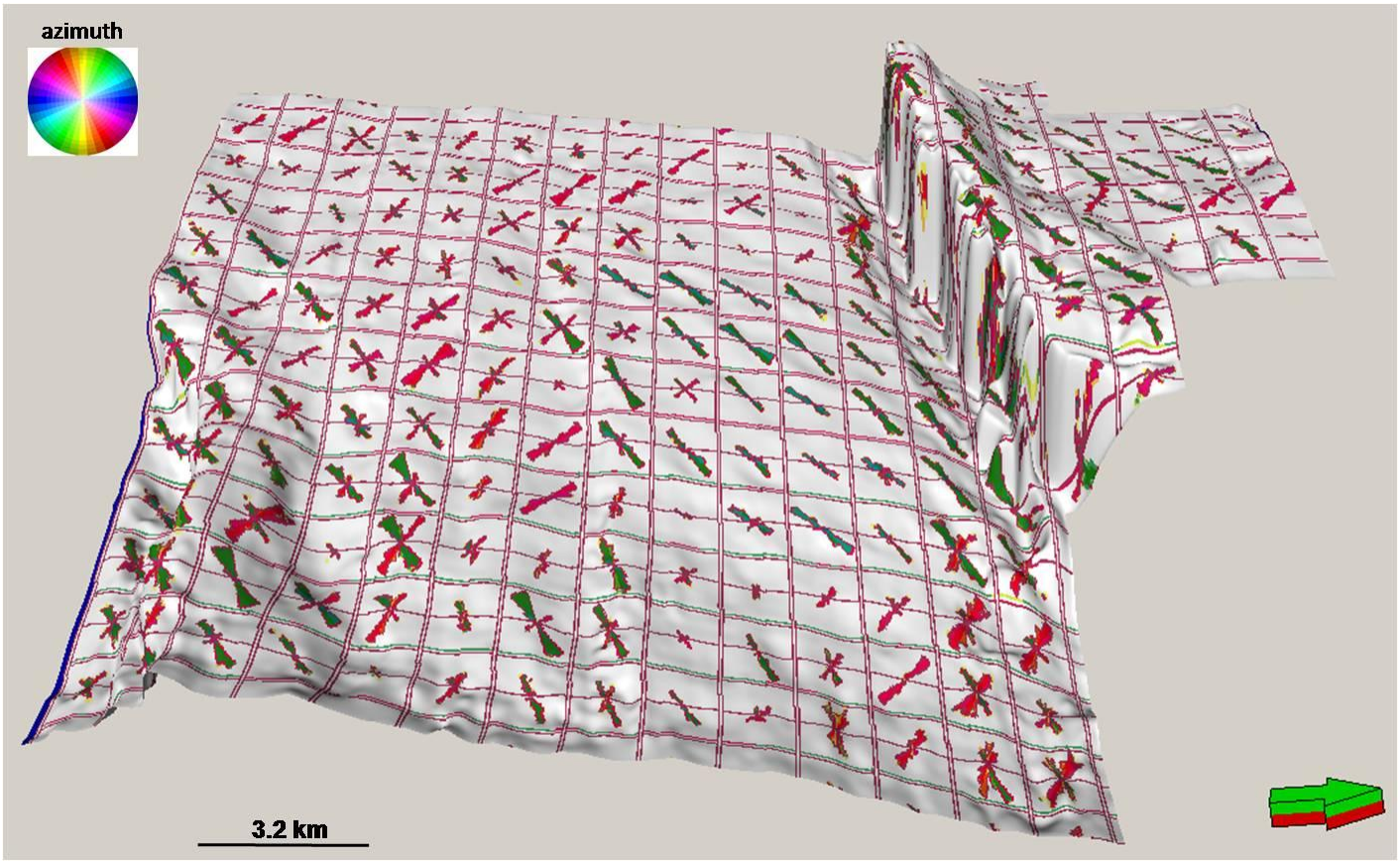

Figure 3-18. Horizon slices through rose diagram calculated from most negative curvature. Different colors represent different azimuth. These lineaments show two dominant orientations: NE and NW.

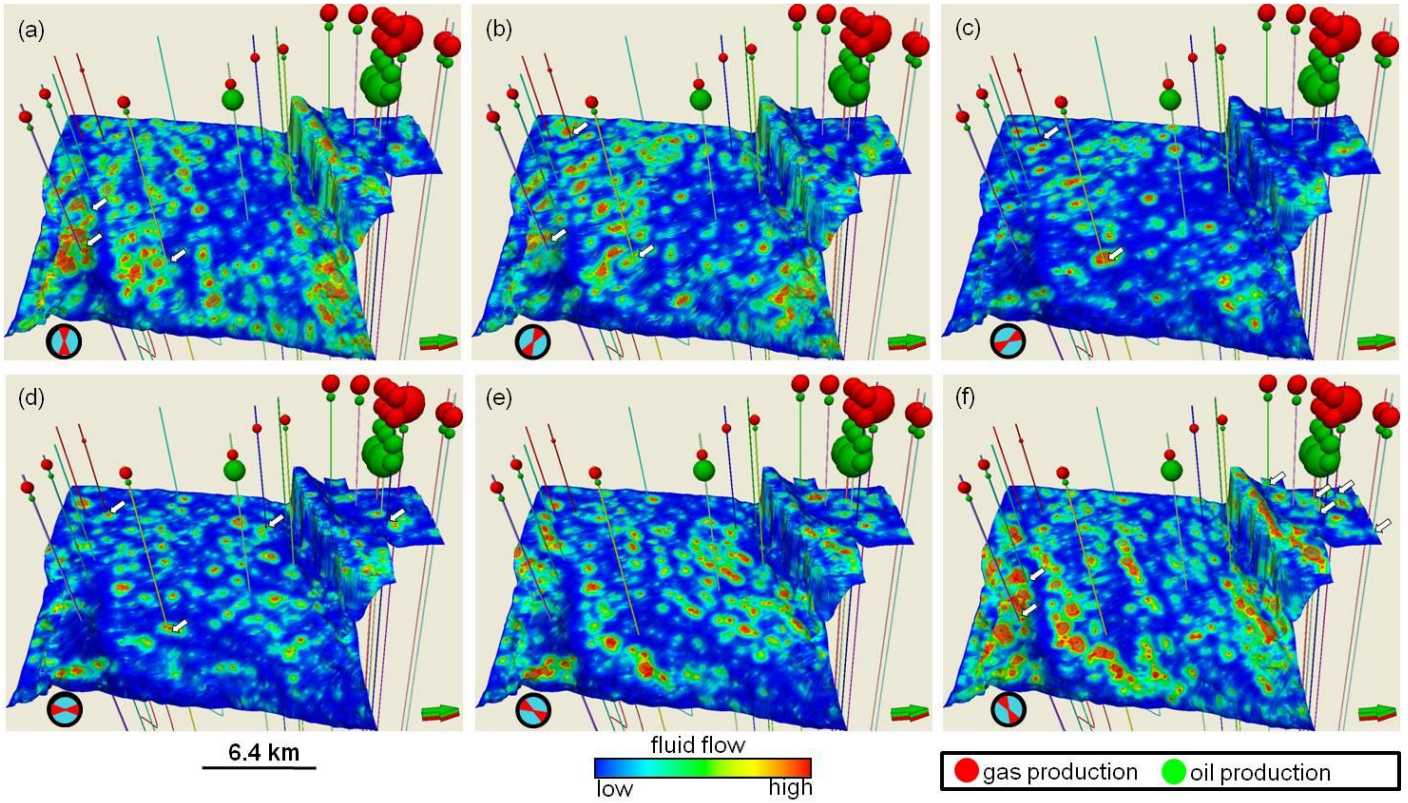

Figure 3-19. Horizon slices along Woodford showing the hypothesized fracture fluid flow from azimuths (a) -90^o, (b) -60^o, (c) -30^o, (d) 0^o, (e) 30^o, and (f) 60^o computed from most negative principal curvature k_2 and its strike. White blocky arrows indicate the wells that have good correlation with the hypothesized fracture fluid flow at a given azimuth. The bubbles represent the gross revenue of the first 90 days of those wells.

	-90	-60	-30	0	30	60	Production ($)
#1	0.04	0.04	0.00	0.06	0.07	0.11	1255449
#2	0.02	0.00	0.00	0.02	0.08	0.22	1473738
#3	0.02	0.09	0.00	0.09	0.00	0.00	287393
#4	0.00	0.00	0.00	0.01	0.00	0.01	1655189
#5	0.02	0.02	0.00	0.07	0.02	0.02	843092
#6	0.07	0.02	0.00	0.01	0.00	0.07	309303
#7	0.06	0.06	0.00	0.01	0.00	0.01	710933
#8	0.01	0.01	0.00	0.04	0.00	0.01	661117
#9	0.04	0.04	0.00	0.06	0.07	0.11	919741
#10	0.03	0.19	0.01	0.02	0.00	0.00	943046
#11	0.11	0.09	0.00	0.03	0.03	0.06	1258780
#12	0.18	0.04	0.00	0.00	0.01	0.30	921799
#13	0.05	0.05	0.00	0.03	0.02	0.06	297464
#14	0.01	0.15	0.01	0.20	0.00	0.00	0
#15	0.18	0.04	0.00	0.00	0.01	0.30	1076063
#16	0.02	0.03	0.01	0.13	0.01	0.03	76912
#17	0.00	0.00	0.00	0.01	0.00	0.01	1139721
#18	0.01	0.02	0.01	0.01	0.00	0.00	137504
#19	0.54	0.18	0.00	0.01	0.02	0.09	749376
#20	0.02	0.04	0.03	0.09	0.01	0.03	130175
X-correl	0.087	-0.199	-0.523	-0.549	0.448	0.383	

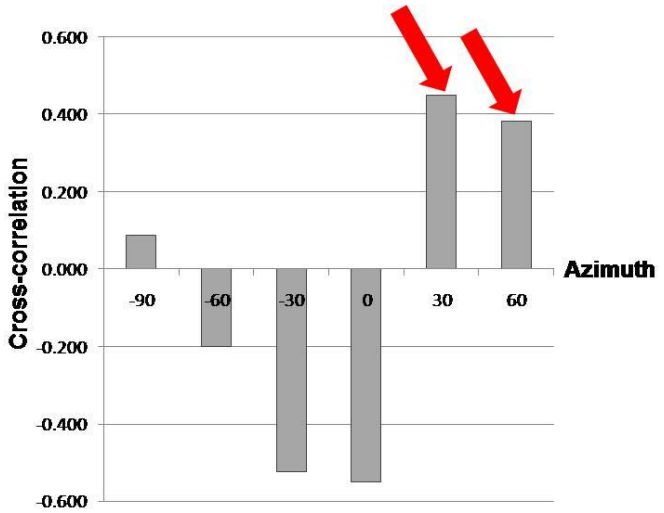

Figure 3-20. Correlation of hypothesized fluid flow from different azimuth to the gross revenue of first 90 days of all the wells in the survey calculated using $4/MCF (thousand cubic feet) for gas and $80/barrel for oil. Fractures in NE direction (30^o and 60^o) tends to have more contribution to the fluid flow.

References

Arasu, R. T., M. D. Al-Ajmi, S. K. Singh, A. K. Dey, T. F. Al-Adwani, and K. Devlikanov, 2010, Integrated interpretation techniques for detection of fracture corridors – an essential play element of hydrocarbon potential for a tight carbonate reservoir in southeast Kuwait: 80th Annual International Meeting, SEG, Expanded Abstracts, 1428-1431.

Chopra, S., and K. J. Marfurt, 2007, Seismic attributes for prospect identification and reservoir characterization: SEG.

Goebel, E. D., 1966, Stratigraphy of Mississippian rocks in western Kansas: Ph. D dissertation, University of Kansas, Lawrence.

Guo, Y., K. Zhang, and K. J. Marfurt, Seismic attribute illumination of Woodford Shale faults and fractures, Arkoma Basin, OK: 80th Annual International Meeting, SEG, Expanded Abstracts, 1372-1375.

Hart, B. S., R. A. Pearson, and G. C. Rawling, 2002, 3-D seismic horizon-based approaches to fracture-swarm sweet spot definition in tight-gas reservoirs: The Leading Edge, **21**, 28-35.

Hennings, P. H., J. E. Olson, and L. B. Thompson, 2000, Combining outcrop data and three-dimensional structural models to characterize fractured reservoirs: a example from Wyoming: AAPG Bulletin, **84**, 830-849.

Hunt, L., S. Reynolds, T. Brown, S. Hadley, H. Downton, and S. Chopra, 2010, Quantitative estimate of fracture density variations in the Nordegg with azimuthal AVO and curvature: a case study: The Leading Edge, **29**, 1122-1137.

Johnson, M. S., 2010, Parshall Field, North Dakota, discovery-of-the-year for the Rockies and beyond: GSA annual meeting 2010.

Narhari, S. R., A. L. Al-Kandari, V. K. Kidambi, S. Al-Ashwak, B. Al-Qadeeri, and C. Pattnaik, Understanding fractures through seismic data: North Kuwait case study: 79th Annual International Meeting, SEG, Expanded Abstracts, 547-550.

Nelson, R. A., 2001, Geologic Analysis of Naturally Fractured Reservoirs: Elsevier.

Nissen, S. E., T. R. Carr, K. J. Marfurt, and E. C. Sullivan, Using 3-D seismic volumetric curvature attributes to identify fracture trends in a depleted Mississippian carbonate reservoir: implications for assessing candidates for CO_2 sequestration: AAPG studies in geology, **59**, 297-319.

Nodine-Zeller, D. E., 1981, Karst-derived early Pennsylvanian conglomerate in Ness County, Kansas: Kansas Geological Survey, Bulletin 222.

Rich, J., 2008, Expanding the applicability of curvature attributes through clarification of ambiguities in derivation and terminology: 78th Annual International Meeting, SEG, Expanded Abstracts, 884-888.

Sullivan, E. C., K. J. Marfurt, A. Lacazatte, and M. Ammerman, 2006, Application of new seismic attributes to collapse chimneys in the Fort Worth Basin: Geophysics, **71**, 111-119.

Chapter 4: Seismic attribute illumination of an igneous reservoir in China

Kui Zhang[1], Zhonghong Wan[2], Shifan Zhan[2], and Kurt J. Marfurt[1]

[1]The University of Oklahoma, School of Geology and Geophysics, [2]Bureau of Geophysical Prospecting, China National Petroleum Corporation

Email: kui.zhang-1@ou.edu, zhhwan@sohu.com, zhanshifan@bgp.com.cn, and kmarfurt@ou.edu

This paper was originally submitted to The Leading Edge journal for publication in July 2010.

Chapter 4: Seismic attribute illumination of an igneous reservoir in China

Introduction

When lava flows and pyroclastic deposits exhibit sufficient porosity and permeability, extrusive igneous rocks have the potential to host large hydrocarbon accumulations. The porosity in these deposits can come from either vesicular porosity, or from secondary porosity resulted from later fracturing and hydrothermal alteration. Recent studies (Feng, 2008) showed that significant hydrocarbon reserves are contained in volcanic rocks in China which are primarily found in the Songliao, Bohai Bay, and Erlian Basins. These hydrocarbon-rich reservoirs range from upper Jurassic to Tertiary in age. Historically, volcanic rocks have not been considered to be good hydrocarbon reservoirs. For that reason, these igneous reservoirs were not fully explored, waiting for recent advances in geophysical techniques. These techniques include high resolution gravity and magnetic data, as well as 3D seismic data acquisition, true amplitude processing and quantitative interpretation.

During last decade, seismic attributes have become one of the key components in characterizing subsurface geological features including turbidites, gas shales, dewatering, and collapse features. In addition to aiding the mapping of large-scale structural and stratigraphic targets, attributes can also enhance very subtle changes in lithology and fluids through careful calibration with well control.

To date, interpreters tended to use seismic data directly (Hansen et al., 2004; Trude, 2004; Farooqui, 2009) to study the geometry of igneous bodies, which are often well-imaged due to the significant contrast in acoustic properties between igneous and surrounding sedimentary rocks. In contrast, there are only a few studies of the seismic attribute expression of igneous rocks (Pena et al., 2009; Jiang et al., 2004). Theoretically, seismic attributes, which extract individual components of the seismic response, enhance the subtle features that are often difficult to see in the seismic data. Hence, seismic attributes hold significant potential to delineating the spatial distribution and internal architecture of the intrusive and extrusive igneous bodies that may form hydrocarbon reservoirs.

This paper applies a three-dimensional seismic geomorphology workflow to a volcanic reservoir in Songliao Basin, Northeast China. Since the volcanic buildup under the study has strong reflectivity and the volcanic conduit generates a chaotic seismic response, both amplitude and geometric attributes provide a very good illumination of the volcanic architectural elements.

Geologic setting

The Songliao Basin is a Mesozoic–Cenozoic age rift basin, spanning 260,000 km^2 and covering over four provinces in northeast China. The Songliao Basin is one of China's most prolific hydrocarbon-producing areas, with 0.14 trillion cubic meters of gas found in deep formations with 60-70% of the total gas stored in volcanics and volcaniclastic rocks. During late Jurassic to early Cretaceous age, several rift depressions

were developed in the basin, resulting in sediment deposition in the late Jurassic Huoshiling Formation, and early Cretaceous Shahezi, Yingcheng, and Denloukou Formations. Intense volcanic activities considerably began during the deposition of early Yingcheng Formation associated with strong structural inversion. Faults bounding the rift depressions served as the major conduits for both deep magma and CO_2. During the upper Cretaceous, thick organic-rich source rocks were deposited in the basin, juxtaposed to the volcanic reservoirs. The rhyolite, basalt and rhyolitic tuff in the Yingcheng Formation in our study is one of the most productive volcanic reservoirs in China (Jin et al., 2008). Core analysis and microscopic imaging show that the porosity and permeability of the reservoir rocks is controlled by lithofacies and spatial combination of lithofacies. The average porosity of the volcanic reservoir exceeds 10%, and some rocks may reach 25% porosity. The permeability varies considerably in the reservoir, but some parts of rocks are highly permeable.

Seismic data and methodology

The seismic survey we discuss was acquired in the northeastern part of the Songliao Basin (Figure 4-1) to better delineate the structural elements of the volcanic reservoir deposited as part of the Yingcheng Formation (Figure 4-2). The data were processed using a standard workflow including signal-to-noise ratio enhancement, statics correction, and careful velocity analysis followed by prestack Kirchhoff time migration. Next, the multiwindow structure-oriented principle component (PC) filtering was applied to the seismic data to enhance the fault terminations. Figure 4-3 shows the comparison of

seismic sections before and after two passes of PC-filtering. Note that the filtered result provides an improved image of the fault and volcanic conduit edges.

Seismic attributes expression of the igneous body

Igneous bodies are often well illuminated in 3D seismic data, giving rise to very high reflection coefficients due to large difference in acoustic properties between the igneous rocks and the encasing sedimentary rocks. This characteristic and the modern analog of volcanic eruption (Figure 4-5) enable us to interpret the geometry of the volcanic buildup with confidence (Figure 4-4). We interpreted the pull-up seen in Figure 4-4a to be a distortion caused by the overlying high-velocity volcanics. The seismic amplitude time slices in Figures 4-6a to 4-6d clearly show the cone shaped appearance of the volcanic vent and conduits. The high coherent energy in Figure 4-6e to 4-6h indicates the distribution of the pyroclastic deposits and the change of radius of the volcanic conduit with depth. The Sobel filter similarity time slices 6i-6l facilitate interpreters to map a suite of south-east trending faults, some of which cut the igneous extrusion, which are key components for the reservoir study.

Figures 4-7a to 4-7d are inline energy gradient slices generated along structural dip in the inline direction by taking the second derivative of seismic amplitude, and they clearly show the strong amplitude change around the circular volcanic conduit and the south-east trending faults. The peak spectral magnitude slices in Figures 4-7e to 4-7h add more confidence to our interpretation, in which hot zones illuminate the possible

distribution of the volcanic rocks. Figures 4-7i to 4-7l give the co-rendered images based on the inline energy gradient and peak spectral magnitude.

Figure 4-8a is the interpreted time-structure map of the top of the volcanic extrusion, and the volcanic body shows high similarity with modern volcanic mountain (Figure 4-5). Figures 4-8b to 4-8d are k_1 most positive curvature, k_2 most negative curvature, and reflection strength respectively. Figure 4-8e is the co-rendered image from time structure map and k_1 curvature, and in Figure 4-8f, the Sobel filter coherence is overlain onto the time structure map by keeping only the low coherence through color blending. Obviously, each of these attributes are mathematically independent, but coupled through the underlying geology, allowing us to accurately map the spatial distribution, and texture of the volcanic extrusion, and its structure and texture along the top surface of the igneous body. Some NE faults are also well-imaged on these slices. The strong magnitude in the slice of reflection strength indicates clearly the extent of the volcanic deposits, which might be valuable in assisting the reservoir volumetric calculation.

Conclusions

Volcanic rocks in China, Argentina, and other parts of the world serve as hydrocarbon reservoirs. In other areas such volcanic features may be mistaken for carbonate buildups. It is our hope that by presenting images of an important producing volcanic reservoir in the context of seismic geomorphology, that our exploration colleagues can use it as a proven analogue. A prominent feature of the volcanic rocks is

that they typically have strong amplitude in seismic response, such that amplitude-related attributes such as spectral magnitude and reflection strength provide effective means of mapping volcanics. Geometrical attributes including coherence, and curvature also provide convincing results by revealing conduits, the structure and texture of the surface of the igneous body, and also faults cutting into the igneous body. The work in next step is to evaluate of the igneous reservoir properties measured in logs and analyze their correlation with seismic attributes.

Acknowledgements

We thank Bureau of Geophysical Prospecting of China National Petroleum corporation for use of their seismic data. We also extend our appreciation to the industry sponsors of the University of Oklahoma Attributes-Assisted Processing and Interpretation (AASPI) Consortium.

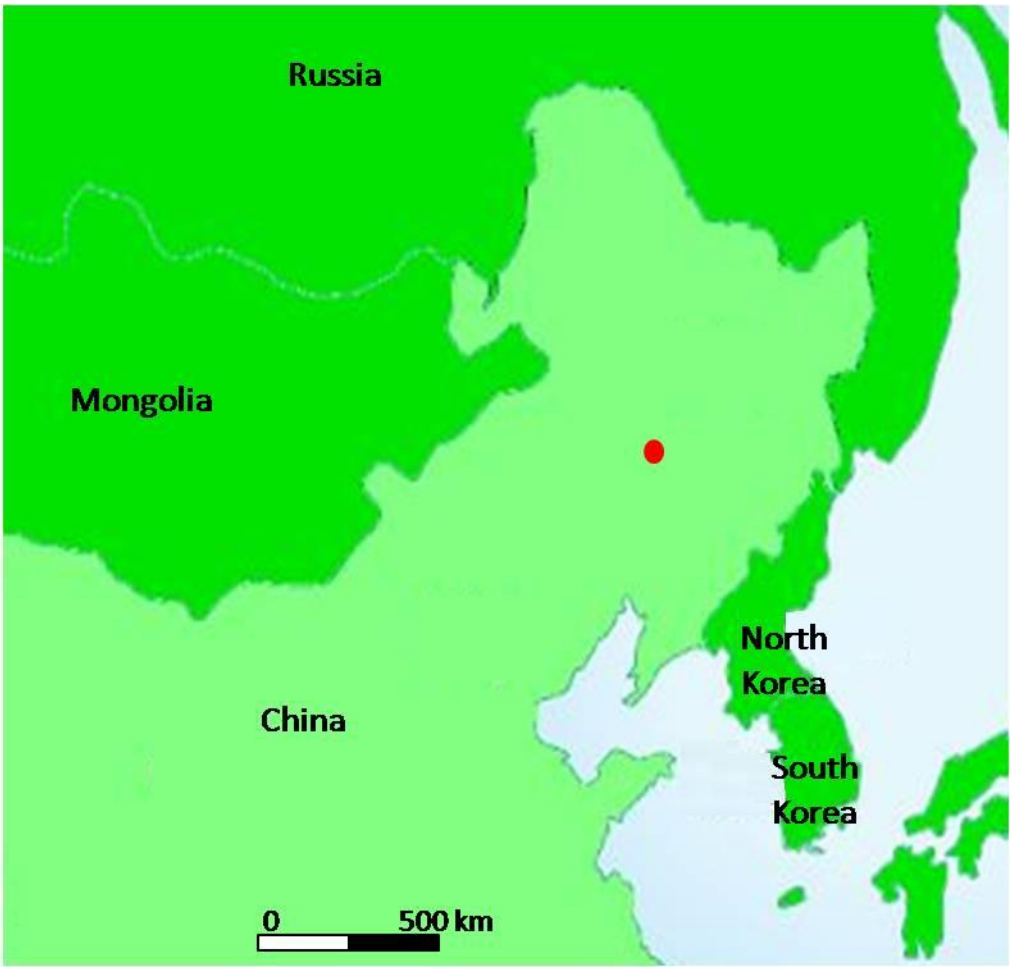

Figure 4-1. Location map, in which red circle marks the location of the seismic survey under study.

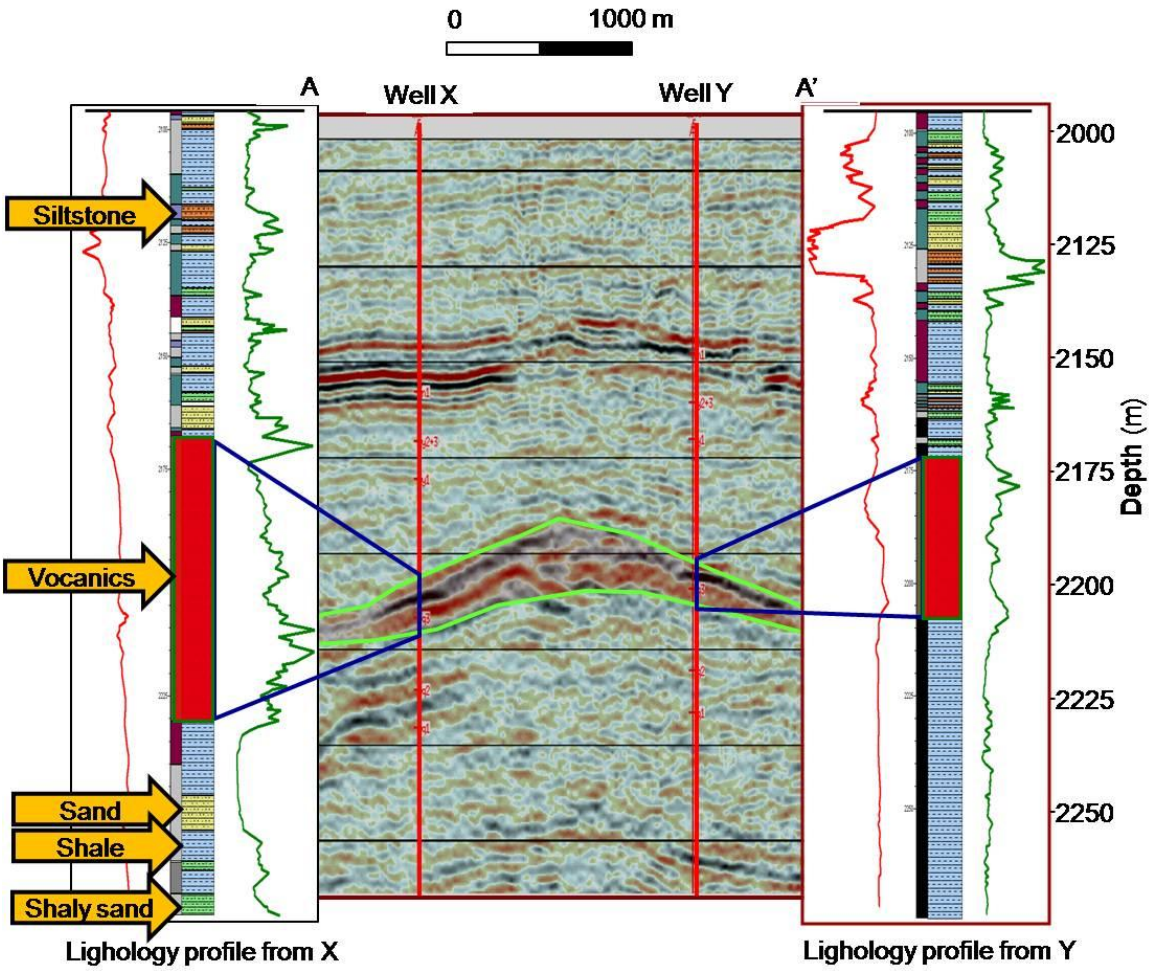

Figure 4-2. Lithologic column from wells X and Y tied to the seismic data. Volcanic rocks are colored in red. The location of line AA' , well X and Y is shown in figure 4-5.

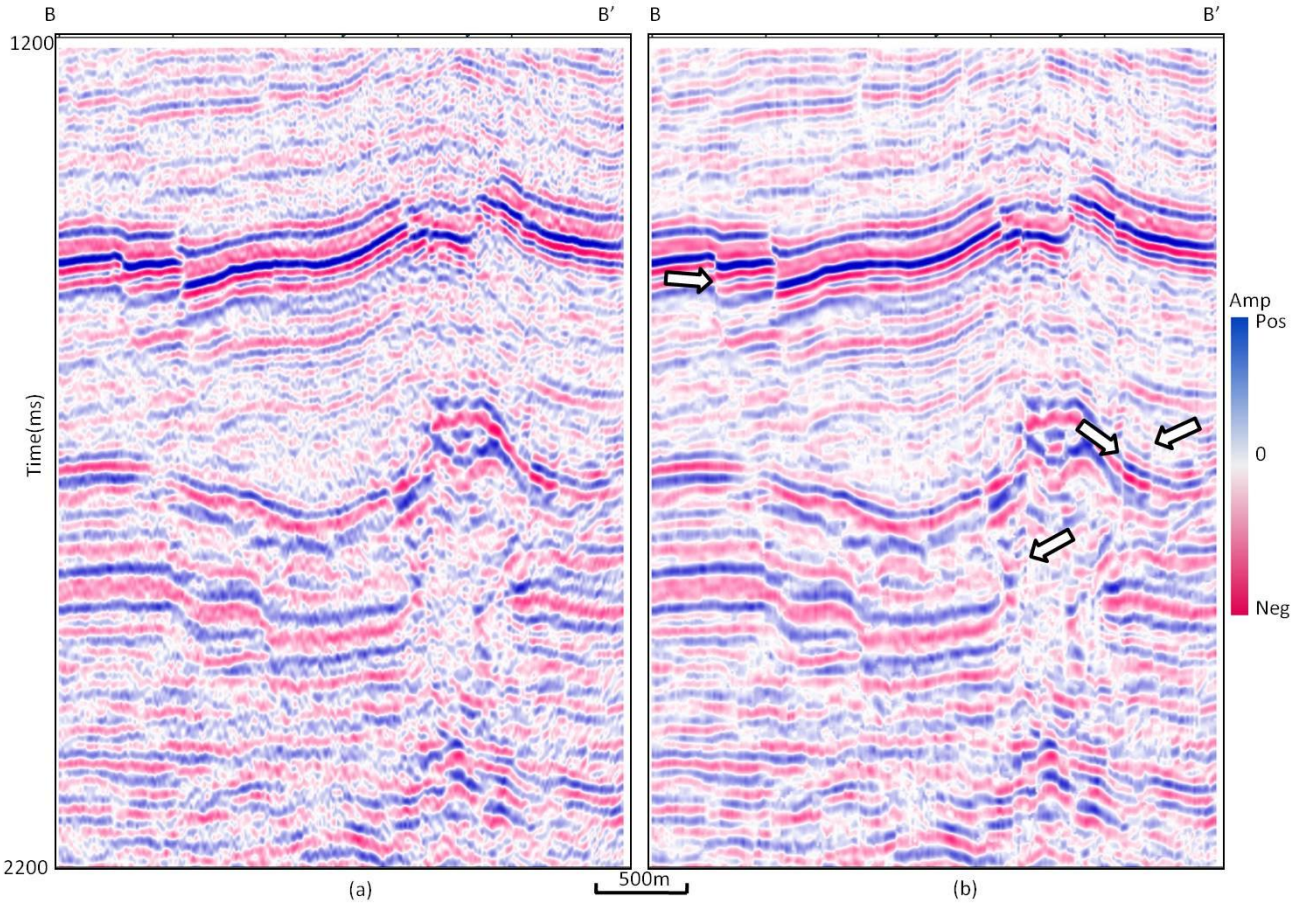

Figure 4-3. Seismic section (a) before and (b) after structure-oriented filtering. Arrows indicate discontinuities that have been enhanced.

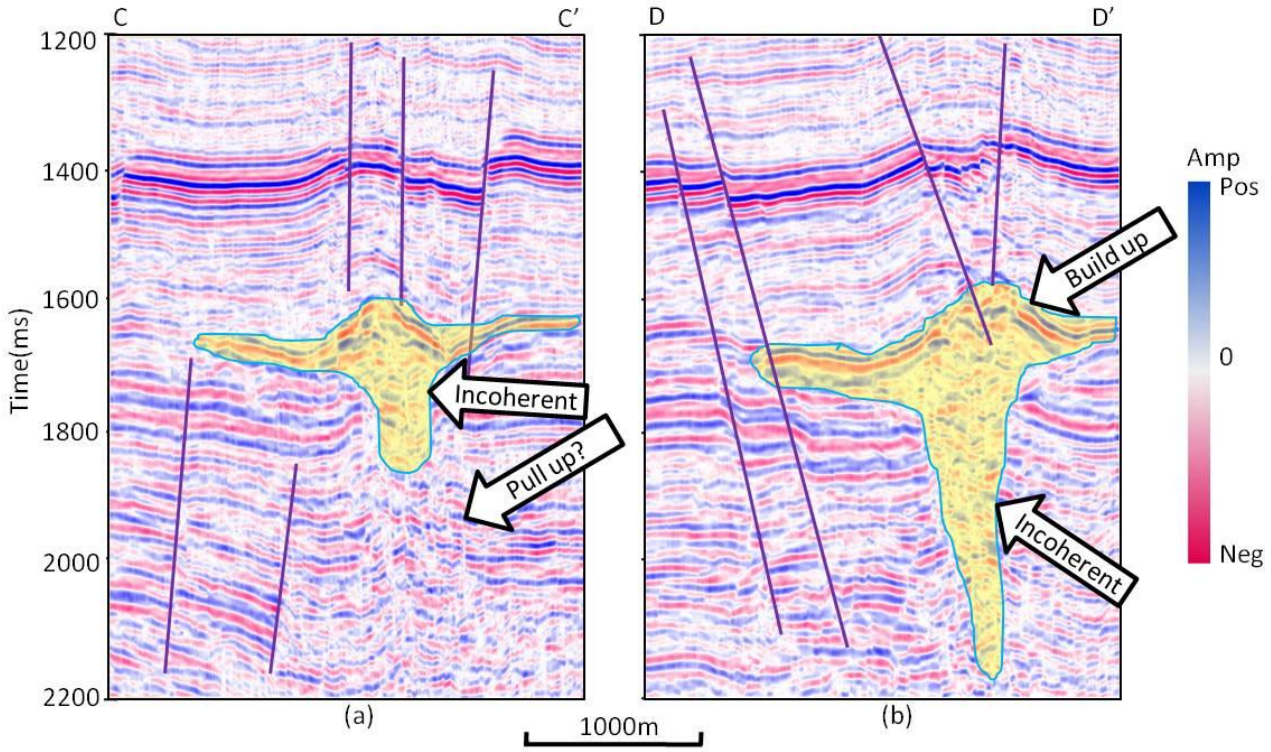

Figure 4-4. An inline seismic section (a) and crossline section (b) with the interpreted igneous body. We interpret the upward dipping reflectors below the volcanic build-up to be due to velocity pull-up.

Figure 4-5. Modern analog of an active volcano at Koryaksky. (MODIS, USGS)

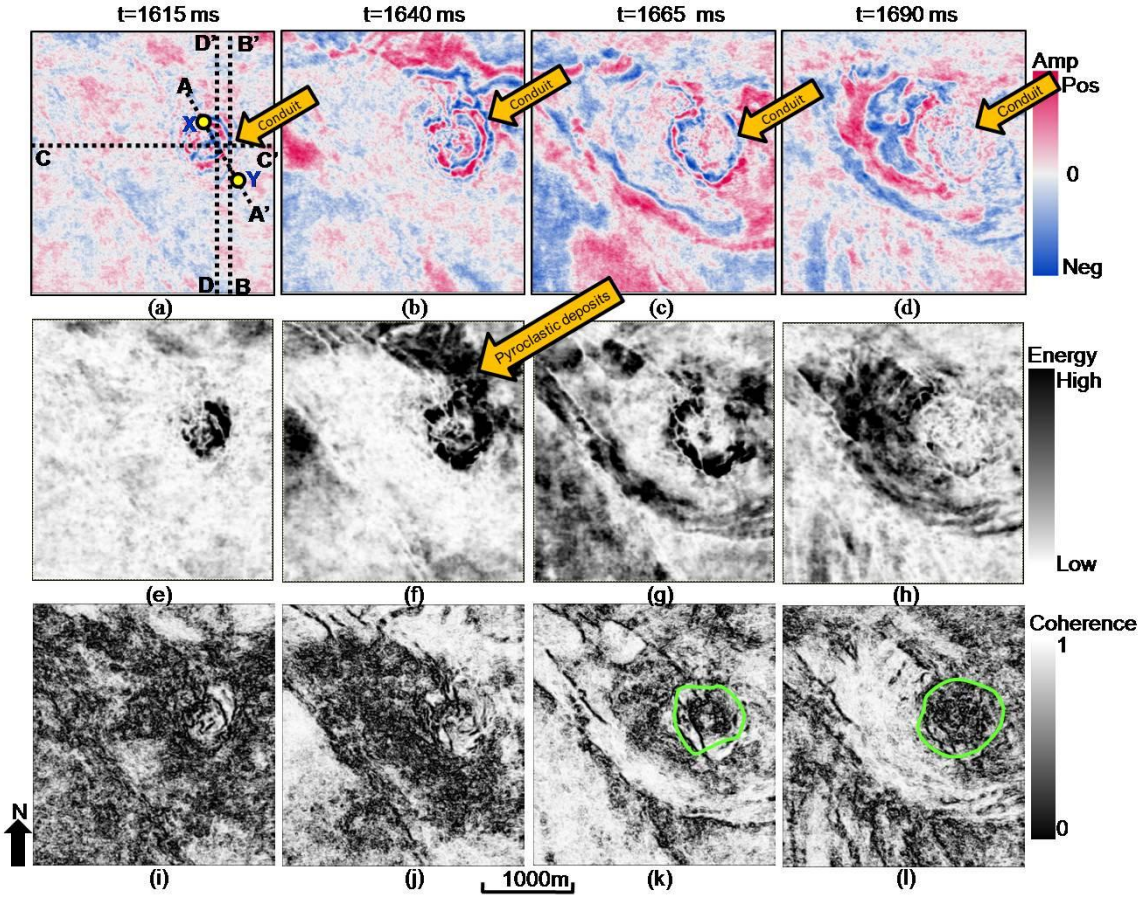

Figure 4-6. Seismic amplitude (a)-(d), coherent energy (e)-(h), and Sobel filter coherence (i)-(l) from four different time slices. Notice that the volcanic conduit and the pyroclastic deposits are shown evidently. Locations of wells X and Y are joined by line AA'. Line BB' is shown in Figure 4-3, and lines CC' and DD' are displayed in Figure 4-4.

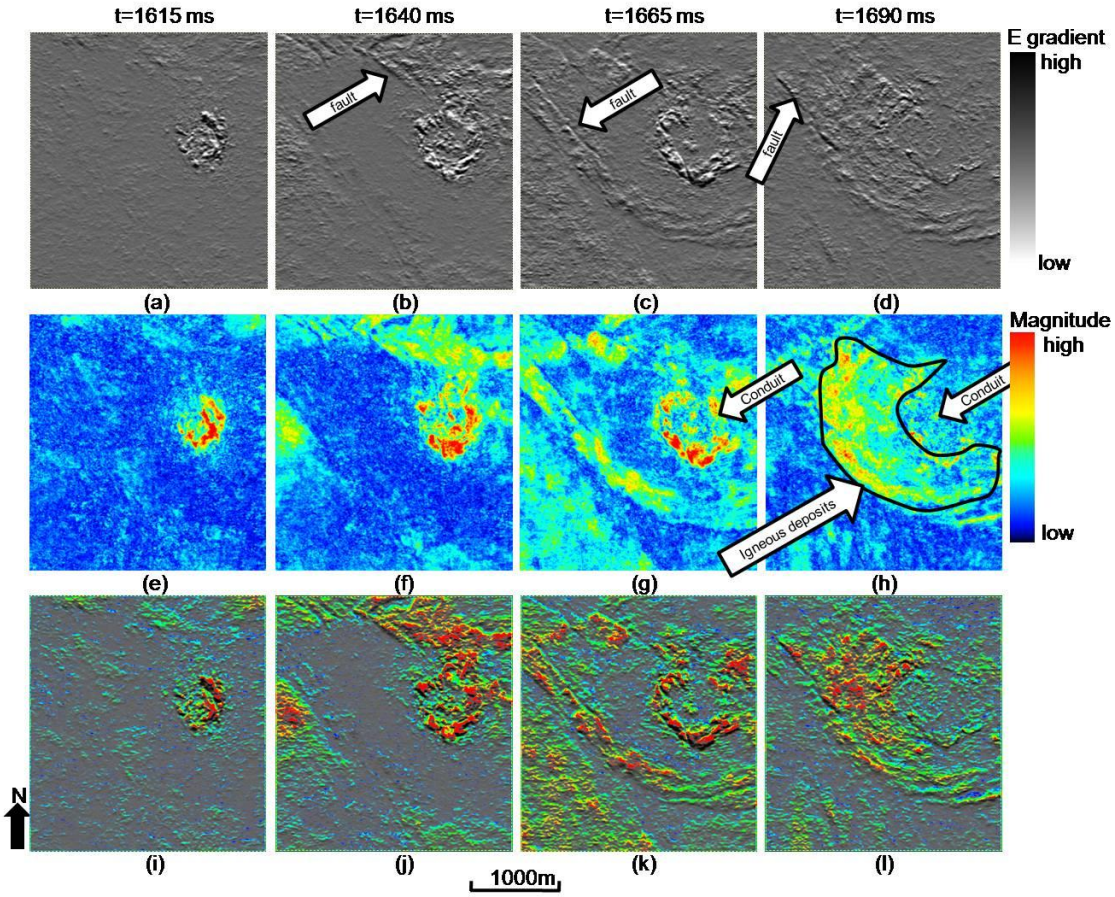

Figure 4-7. Inline energy gradient (a)-(d), spectral peak magnitude (e)-(h), and the co-rendered images of them (i)-(l). Blocky arrows point to faults, conduits, or pyroclastic deposits.

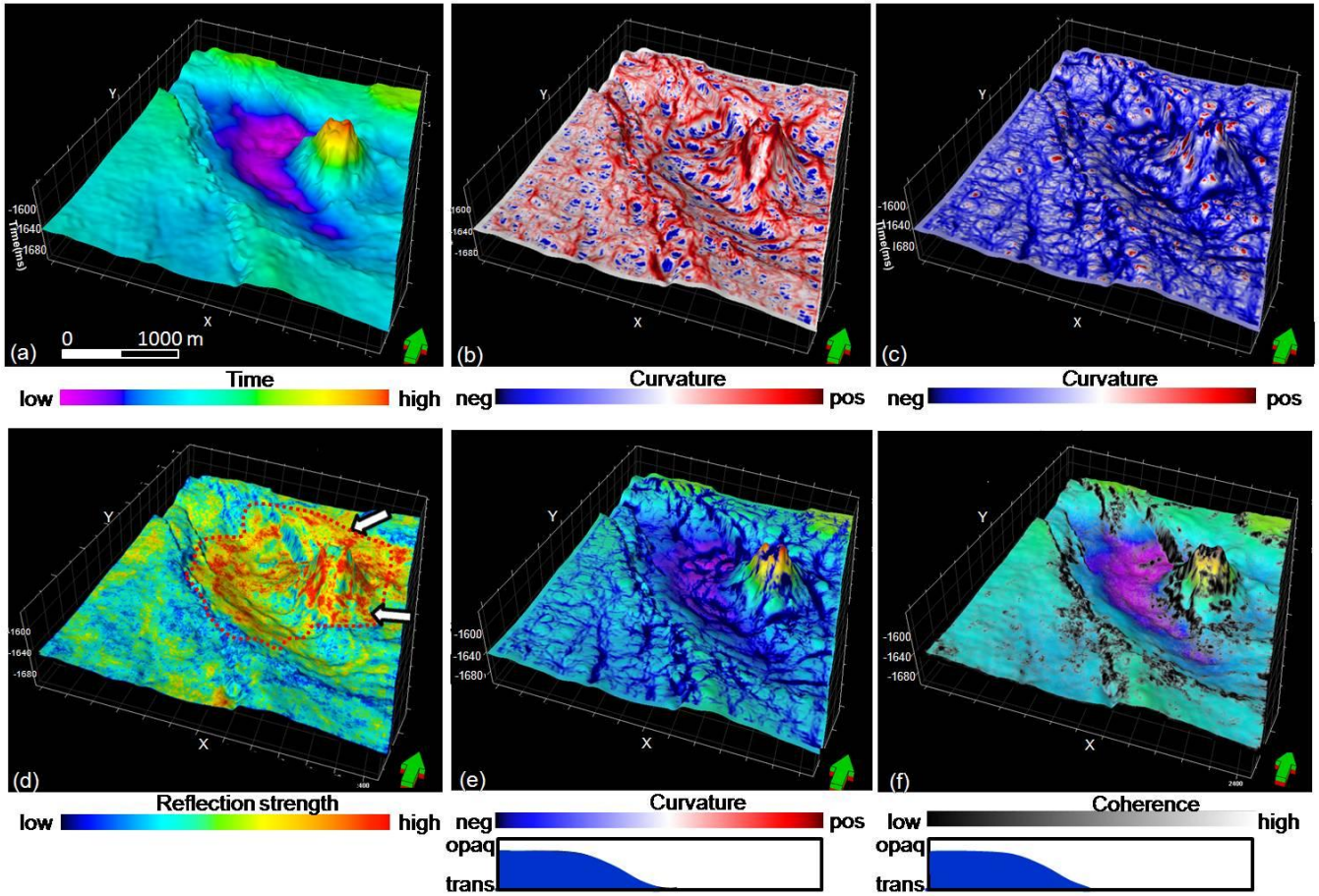

Figure 4-8. Time structure map (a), most positive principal curvature (b), most negative principal curvature (c), reflection strength (d), blended image (e) from time structure and negative curvature, and (f) from time structure and coherence. Blocky arrows in (d) point to volcanic deposits.

References

Hansen, D. M., J. A. Cartwright, and D. Thomas, 2004, 3D seismic analysis of the geometry of igneous sills and sill junction relationships: 3D seismic technology, 199-208.

Pena, V., S. Chávez-Pérez, M. Vázquez-García, and K. J. Marfurt, 2009, Impact of shallow volcanic on seismic data quality in Chicontepec Basin, Mexico: the Leading Edge, **28**, 674-679.

Trude, K. J., 2004, Kinematic indicators for shallow level igneous intrusions from 3D seismic data: evidence of flow direction and feeder location: 3D seismic technology, 209-218.

Farooqui, M. Y., H. Hou, G. Li, N. Machin et al., 2009, Evaluating Volcanic reservoirs: Schlumberger Oilfield Review, Spring 2009, 36-47.

Feng, Z., 2008, Volcanic rocks as prolific gas reservoir: A case study from the Qingshen gas field in the Songliao Basin, NE China: Marine and Petroleum Geology, **25**, 416-432.

Jin, C., W. Dan, D. Qiao, and D. Zhang, 2008, The volcanic oil and gas reservoirs in eastern basins of China: 33rd International Geological Congress OSLO.

Chapter 5: Extension of spectral-decomposition into mapping stratigraphic patterns

Kui Zhang[1] , Kurt J. Marfurt[1], and Marcilio Castro de Matos[2]

[1] *University of Oklahoma, School of Geology and Geophysics,* [2]*Instituto Militar de Engenharia, Brazilian Army*

Email: kui.zhang-1@ou.edu, kmarfurt@ou.edu, and marcilio@matos.eng.br

Paper submitted at the 77th Annual Society of Exploration Geophysicists International Exposition meeting in Las Vegas, Nevada, USA

SEG Expanded Abstracts 27, 919-923 (2008)

Paper submitted at the 78th Annual Society of Exploration Geophysicists International Exposition meeting in Houston, Texas, USA

SEG Expanded Abstracts 28, 3515-3519 (2009)

Chapter 5: Extension of spectral-decomposition into mapping stratigraphic patterns

Abstract

Spectral-decomposition has become a standard tool in aiding stratigraphic interpretation. However, spectral-decomposition presents considerable challenges for human interpretation in that the unwieldy 4D spectral amplitude and phase cubes obtained from 3D seismic input are not amenable for visual analysis. The primary goal of statistical measures of dozens of 3D amplitude and phase components from spectral-decomposition is to provide geologically meaningful estimates that significantly reduce what may be intractably large 4D volumes into small 3D volume. Until now, spectral attributes base on spectra mode have proven to be very instrumental in providing information sensitive to stratigraphy.

Seismic spectra are non-Gaussian after spectral balancing, such that measures of standard deviation, skewness, and kurtosis have limited value. To address this problem, we introduce statistical spectral attributes based on percentiles. We apply these new attributes to two surveys: a land survey acquired over the Central Basin Platform, west Texas, and a survey acquired over Anadarko Basin, Oklahoma, and find the Range-Trimmed Mean magnitude, spectral slope and roughness provide very effective delineation of channels complementary to the well-established edge-sensitive attributes. We also evaluate the sensitivity of these spectral attributes to sequence stratigraphic architecture through investigation of a suite of models, and find that peak frequency and mean frequency are sensitive to the details of the vertical arrangement of different

stratigraphic packages, potentially allowing one to differentiate upward fining, upward coarsening, and blocky patterns.

Introduction

First applied to 3D seismic volumes by Partyka et al. (1999), spectral-decomposition has since become a routine interpretation analysis tool in quantification of tuning thickness (Marfurt and Kirlin, 2001; Tirado, 2004), direct hydrocarbon detection (Castagna et al., 2003), and geological facies delineation (Liu and Marfurt, 2007). More recent applications involve measurement of attenuation, lithology, and fluid type (Li et al., 2006; Maklad and Dirstein, 2007).

Unfortunately, the 4D spectral-decomposition magnitude and phase components obtained from a single 3D seismic amplitude volume are often unwieldy, presenting both visualization and data management problems. Although principle component analysis provides an effective means to reduce the data dimensionality (Guo et al., 2006), such principal components have only a mathematical, rather than a geological basis, and their correlation to well logs is data- and survey- dependent. In contrast, simpler attributes, representing the mode of the 4D complex spectra, such as peak magnitude, peak frequency, peak phase (Liu and Marfurt, 2007; Matos and Johann, 2007), and peak magnitude above the average spectrum (Blumentritt, 2008) have proven to be very useful and broadly used. Other measures based on spectral moments like skewness and kurtosis also provide interpretation value (Zhang et al., 2008; Steeghs and Drijkoningen, 2001).

Theoretically, for a broad-band, spectrally white seismic source wavelet, the seismic expression of different geological sequences such as retrogradational and progradational systems in clastic depositional environments are a direct function of the spectral response which in turn is controlled by acoustic impedance contrasts. By decomposing the seismic amplitude into different frequencies at every temporal sample, spectral-decomposition has the potential of quantitatively discriminating between different stratigraphic packages (Steeghs and Drijkoningen, 2001).

We start by reviewing how one can statistically flatten the spectrum to minimize the modifications of the spectral shape by the source wavelet. Next, we introduce a new suite of attributes based on the balanced spectra that are generalizations of earlier quartile-based measurements that remove data extrema, and apply them to the data acquired over the Central Basin Platform, west Texas, and Anadarko Basin, Oklahoma. Finally, we investigate how peak frequency and mean frequency from time-frequency decomposition can be visually tied to different depositional patterns though synthetic modeling, and application to a deepwater dataset acquired over an outcrop in Wyoming, USA.

Methodology

Spectral balancing plays an important part in extracting tuning effects by removing the spectral bias caused by seismic wavelet. Our spectral balancing approach is performed internal to the matched pursuit spectral-decomposition (Liu and Marfurt, 2005; Liu, 2006) by assuming the geology to be random, giving rise to a “white” spectrum. We

first calculate the time-frequency spectra for the entire volume. Then, we assume the reflectivity is random, with a white spectrum within a 500 ms window spanning the entire survey:

$$S(t, f) = \frac{1}{N(2K+1)} \sum_{k=-K}^{k=+K} \sum_{x,y} a(t + k\Delta t, f, x, y) \quad (1)$$

where *a(t, f, x, y)* is the spectral magnitude at time *t*, frequency *f*, and trace location (*x, y*). With this assumption, the reflectivity spectrum can be approximated by

$$\bar{a}(t, f, x, y) = \frac{a(t, f, x, y)}{s(t, f) + \beta MAX[s(t, f)]} \quad (2)$$

where, β is a small whitening factor that prevents boosting unacceptably small source spectral component.

Figure 5-1 shows a representative spectrum after spectral balancing, with a relatively flat behavior bound by two tails. One way to define the bandwidth is to measure the width between points where the magnitude reaches half of peak magnitude. We choose a different method, and integrate the magnitude between f=0 and f=$f_{Nyquist}$ (Figure 5-1b). Thus, the Range Trimmed Mean (R-T Mean) magnitude is the integration of the spectral magnitude from J_{low} to J_{high}. Pearson and Hart (2004) recognized that, slope between peak frequency and maximum frequency is helpful in reservoir development and it suggests the reservoir attenuation. Companies like Apex approximate the slope with a decaying exponential. In this work, we simply define the slope between J_{low} and J_{high}.

We conduct the slope calculation in a more flexible manner since the interpreter can control according to their understanding of the data and geology. Principally, the

slope measure is sensitive to porous rocks and fractures, and can be used to calibrate the porosity of the reservoir if the seismic data is processing in an amplitude preserved manner. Roughness measures how much a spectrum deviates from the slope which is difficult to interpret sometime, but it also carries some geology information. The mathematic details of these attributes are illustrated in Appendix A.

We can define the mean frequency as,

$$\overline{F}(t) = \frac{\int_{f_{low}}^{f_{high}} f \cdot \overline{a(t, f)} df}{\int_{f_{low}}^{f_{high}} \overline{a(t, f)} df + \varepsilon} \qquad (3)$$

Where, $\overline{a(t, f)}$ is the balanced spectrum described above, and f_{low} and f_{high} are frequencies corresponding to J_{low} and J_{high} respectively. The term ε is a small value which prevents the denominator from becoming zero.

Expression of channels

A land survey acquired over the Central Basin Platform, west Texas

We apply the spectral attributes described above to a land survey acquired in the Central Basin Platform, west Texas with the goal of identifying several Paleozoic meandering channels described by Liu and Marfurt (2007). To investigate the effectiveness of above introduced spectra attributes, we generate the time structure map along the atoka unconformity (Figure 5-2). Figure 5-3 shows a phantom horizon slice 50 ms above the picked Atoka unconformity through peak magnitude. Several channels are

clearly identified by peak magnitude indicated by green arrows. Figure 5-4 shows the same phantom horizon slice through R-T Mean magnitude. Notice that R-T Mean magnitude provides slightly better delineation of those meandering channels indicated by green arrows than peak magnitude. The spectral slope horizon slice in Figure 5-5 also captures those channels. Overall, the channel spectrum tends to have a positive slope, while the non-channel spectrum has a negative slope. The spectra of channels pointed by red arrows have bimodal behavior. Figure 5-6 shows the spectral roughness map, which also highlights some channel details.

Figure 5-7 shows a vertical seismic window AA', and the analyis of four spectra. It is clear that, channel location pointed by yellow arrows corresponds to small negative, or zero spectral slope, while the transition zone pointed by white arrow between channels shows large negative slope. Also notice that, channel location corresponds to larger R-T Mean magnitude. Spectral slope is calculated from percentile 10 to percentile 90.

Figure 5-8 shows phantom horizon slices 40 ms above Atoka unconformity through (a) coherence, (b) R-T Mean magnitude, and (c) spectal slope. Figure 5-8d is the composite interpretation with 6 channels interepted according to (a), (b), and (c). Compared to coherence in Figure 5-8a, we are able to extend out interpretation of channel 1 and 2 towards southwest using R-T Mean magnitude in Figure 5-8b. We also see channel 5 in Figure 5-8b, which is not visible on the coherence slice. Spectral slope in Figure 5-8c also provides some details about channel distribution although it is noisy. Based on above analysis, R-T Mean magnitude, spectral slope, and roughness can be used to identify features of stratigraphic interest, complementary to the standard coherence measure.

A land survey over Red Fork incised channels: Anadarko Basin, Oklahoma

Spectral-decomposition is one of the most useful tools to map fluvial systems. Liu and Marfurt (2007) showed peak frequency, peak magnitude, and co-rendered images of the two allow us to predict channel thickness. Figure 5-9a shows a time structure map of Skinner Limestone over a land seismic survey (Suarez et al., 2008) acquired in Anadarko Basin, Oklahoma. Figure 5-9b is a phantom horizon slice through amplitude at the Red Fork level, and Figure 5-9c is a vertical seismic section BB' with the channels indicated by yellow arrows. Our goal is to map Red Fork infilled channels with different scales based on spectral attributes.

In Figures 5-10a to 5-10f, we display phantom horizon slices through Sobel filter coherence, crossline energy gradient, most negative curvature, R-T Mean magnitude, spectral slope, and roughness around Red Fork level. Noticeably, a channel in northwest corner is discernable on R-T mean magnitude and roughness maps indicated by cyan arrows, but it is difficult to see on other maps. The slope slice shows some interesting features with north-south trend (green arrows) although the image is a little sloppy. Edge-sensitive attributes (especially curvature) lose their resolution in some parts due to their strong susceptibility to acquisition footprint, whereas our attributes are less susceptible because they are implemented by choosing a frequency range, which eliminates some low and high frequency component noise. Figure 5-11 shows the blended images from (a) mean frequency with R-T Mean magnitude, (b) spectral slope with R-T Mean magnitude, and (c) spectral roughness with R-T Mean magnitude. These maps clearly show the

distribution of major channels, but give slightly different illumanitation of subtle thin channels.

Illumination of reservoir facies

Sequence stratigraphic analysis plays an important part in geological and reservoir modeling, allowing workers to correlate strata surfaces, study reservoir compartments and secondary recovery well planning. Traditionally, core plugs and well logs are used to classify lithofacies and lithostratigraphic units at the architectural element scale. Stratigraphers may then use geostatistical krigging methods to extrapolate their stratigraphic interpretation laterally from the well bore. One of our objectives is to define through modeling and calibration with well logs, volumetric attributes that can be closely tied either visually or statistically to the vertical depositional patterns seen on acoustic impedance logs.

The seismic expression of retrogradational and progradational clastic sequences will be different since the seismic response is controlled by the acoustic impedance contrast which varies with thickness, grain composition and sedimentary structure. Since the frequency content of the seismic response carries abundant subsurface stratigraphic information (Zeng and Kerans, 2003), we follow Hart (2008) and investigate those spectral decomposition attributes sensitive to stratigraphic properties.

Stratigraphers commonly describe log patterns by their shape – giving names that are either descriptive – such as ‘blocky’ or ‘egg-shaped’, or imply a specific depositional environment – such as upward fining, upward coarsening or interbedded sand-shale units.

We generate a suite of geologically realistic synthetic models corresponding to these different scenarios and conclude that the peak frequency and mean frequency from spectral-decomposition are stratigraphically-sensitive attributes which can be utilized to characterize different stratigraphic successions.

We also study an outcropping deep-water stratigraphic sequence, and find that peak frequency and mean frequency show very high cross-correlations with the Gamma Ray log; comparison of these two attributes with core data also provides encouraging results.

Synthetic study

Figure 5-12 shows four simple stratigraphic successions which have cylinder shape (a uniform bed), egg shape (a cycle), funnel shape (a coarsening upward sequence), and bell shape (a fining upward sequence) respectively. One classic example of these models is that of thick massive sands in which the sequence arrangement is controlled by the fluid-sediment flow rate (i.e. a Bouma sequence in deep water depositional environment). We assume that the acoustic impedance represents our sequence models, since acoustic impedance commonly increases with the decreasing of grain size such that shale exhibits higher acoustic impedance than more porous and permeable sandstone within the same depositional system. The spectral-decomposition result of the model shows high sensitivity to the original acoustic impedance, whereby both mean frequency and peak frequency can be used to distinguish different sequence successions. We also add 20% random noise to the synthetic in Figure 5-12b, and obtain the associated results

shown in Figure 5-13. From Figure 5-13, we see that peak frequency still maps sequence models quite well indicated by acoustic impedance, while mean frequency does not correlate well for egge-shaped and upward coarsening models.

Figure 5-14 shows four wedge models with the time thickness ranging from 0 to 50 ms. These four models correspond to (a) blocky pattern, (b) upward coarsening gradational pattern, (c) upward fining gradational pattern, and (d) gradational pattern with gentle slope. Note that the peak frequency is highly correlated to the acoustic impedance in Figures 5-14b and 5-14c, allowing us to map upward coarsening and upward fining patterns. Blocky pattern and gradational pattern with gental slope can not be differentiated by peak frequency. Peak phase might be a potential tool to map these two patterns.

In Figure 5-16, we analyze the spectra of 20 stratigraphic models from Figure 5-15, representing different depositional processes, and illustrate that peak frequency is a very effective tool to map the shapes of these models.

Sequence stratigraphic models from another scenario are shale-sand interbeds illustrated in Figure 5-17 which are very common in some clastic depositional settings. For instance, the periodical sea level oscillations in shallow marine depositional environment can give rise to considerable thickness of interbedded shale-sand deposits. It is readily apparent that time-frequency representation is controlled by shale-sand interbedding (Figures 5-17a to 5-17i), rather than the low frequency linear velocity trend. The peak frequency and mean frequency again show value in differentiating upward fining and upward coarsening sequences, but they fail to differentiate two cases shown in Figures 5-17j and 5-17k, and peak phase might provide the answer for this problem.

Application in a field-data acquired over an outcrop in Wyoming

My real data example is from an outcrop of Cretaceous deepwater deposits in Wyoming, USA (Slatt et al., 2008; Slatt et al., 2009). A 1700 ft. Well (CSM #61) was drilled behind the outcrop of deepwater channel levee, sheet sandstones and associated shales, and a shallow 2D seismic line was acquired over the well site. Calibration of clustered gamma ray, bulk density and inverted sonic transit time log responses to a continuously cored interval in the well defined stratigraphic units within the well that were dominated by sheet sandstones, channel sandstones, shale, and interbedded sheet/channel sandstones.

At the architecture element scale, the vertical relative acoustic impedance and seismic section crossing the outcrop in Figure 5-18 have two major units: a channel levee complex composed of many lenticular channel sandstones between internal levee-overbank deposits; and the underlying laterally continuous sheet sandstones. Figures 5-19a and 5-19b show the seismic wiggle trace from the well location and the associated spectral decomposition result respectively. Figure 5-19c is an amplitude balanced version of the data shown in 19b to better display the lower-amplitude events. Since the gamma ray is the classic tool to characterize different stratigraphic units, it is used to calibrate mean and peak frequency attributes. Figure 5-20 shows a very good correlation between peak frequency, mean frequency and the gamma ray log, thereby indicating that the two spectral attributes are sensitive to vertical variation in stratigraphy (Figure 5-20b). We also predict lithofacies using a commercial package called geological analysis via

maximum likelihood system (GAMLS) in Figure 5-20c, and find that, different deepwater sheet and channel sandstones units given by lithofacies can be discriminated by those two spectral attributes.

Discussions and conclusions

We have demonstrated that statistical spectral attributes extracted from spectral-decomposition could be very useful to reveal subtle stratigraphic features. We find R-T Mean magnitude provides similar features to peak magnitude, but with better delineation of channels. By implementing based on percentile, R-T Mean magnitude, spectral slope, and spectral roughness provide a better representation of flattened spectra than standard deviation, skewness and kurtosis that are valid for nearly Gaussian spectra.

Spectral decomposition is sensitive to lateral and vertical stratigraphic heterogeneity. Using a suite of synthetic models and the real data acquired over an outcrop originally deposited in deepwater suggests that peak frequency and mean frequency derived from the spectral decomposition volume are able to differentiate stratigraphic intervals with different vertical stacking arrangements. Spectral attributes extracted from spectral decomposition still suffers from wavelet interference effects between close-spaced reflections.

Acknowledgements

We extend our appreciation to all sponsors of the Attribute-Assisted Seismic Processing and Interpretation (AASPI) consortium at the University of Oklahoma for their support. We also thank Burlington Resources and Chesapeake Energy for the use of their data in education and research. We give our special thanks to Haitham Alsahfy, Yoscel Suarez, and for their technical help and beneficial discussions.

Appendix A

ATTRIBUTES EXTRACTED AFTER SPECTRAL BALANCING

Let us parameterize the balanced spectrum to have the form

$$m_j = m_0 + s(f_j - f_0), \tag{A-1}$$

where m_j is the magnitude at frequency f_j, f_0 is a reference frequency defined as

$$f_0 = (f_{high} - f_{low})/2, \tag{A-2}$$

and m_0 is the magnitude at the reference frequency, s is the slope. We formulate the misfit between our parameterized model and the data m_j as E:

$$E^2 = \sum_{j=J_{low}}^{J_{high}} [m_j - (m_0 + s(f_j - f_0)]^2, \tag{A-3}$$

m_0 and s can be obtained by solving the following equations

$$\frac{\partial E}{\partial m_0} = -2 \sum_{j=J_{low}}^{J_{high}} [m_j - (m_0 + s(f_j - f_0)] = 0, \tag{A-4}$$

$$\frac{\partial E}{\partial s} = -2 \sum_{j=J_{low}}^{J_{high}} \{[m_j - (m_0 + s(f_j - f_0)](f_j - f_0)\} = 0, \tag{A-5}$$

where $J_{high} = f_{high}/\Delta f$, $J_{low} = f_{low}/\Delta f$, and Δf is the frequency sample interval in Hz.

Combining the A-4 and A-5, we obtain

$$s = \frac{\sum_{j=J_{low}}^{J_{high}} (f_j m_j) - m_{ave} \sum_{j=J_{low}}^{J_{high}} (f_j - f_0)}{\sum_{j=J_{low}}^{J_{high}} (f_j f_j) - f_{ave} \sum_{j=J_{low}}^{J_{high}} (f_j - f_0)}, \tag{A-6}$$

$$m_0 = m_{ave} - s * f_{ave} \ , \tag{A-7}$$

where,

$$f_{ave} = \frac{\sum_{j=J_{low}}^{J_{high}} (f_j - f_0)}{J_{high} - J_{low} + 1}, \tag{A-8}$$

$$m_{ave} = \frac{\sum_{j=J_{low}}^{J_{high}} m_j}{J_{high} - J_{low} + 1} \ . \tag{A-9}$$

We define roughness as,

$$R = \frac{E^2}{J_{high} - J_{low} + 1} \ . \tag{A-10}$$

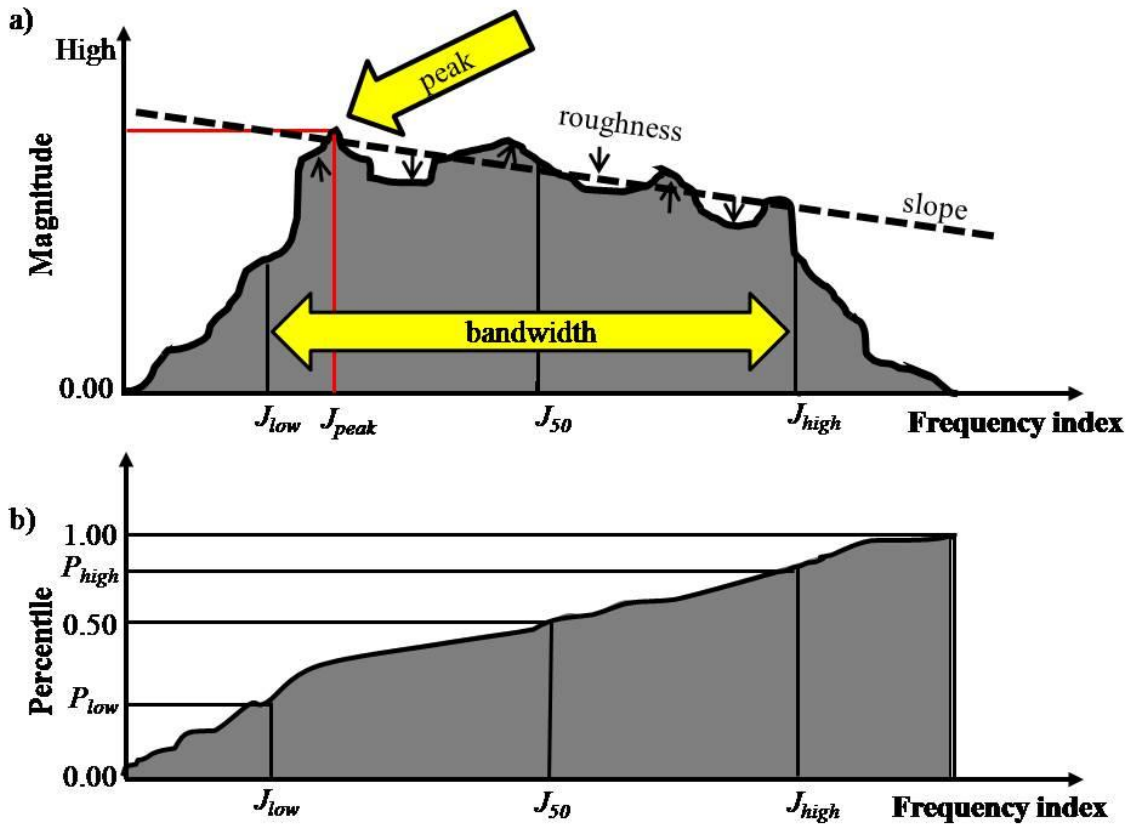

Figure 5-1. (a) A representative spectrum and (b) the cummulative magnitude expressed as a percentile. J_{low} and J_{high} are the frequency index associated with the low percentile P_{low} and high percentile P_{high} defined by the interpreter as percentiles. The peak magnitude occurs at J_{peak}. We define the R-T Mean magnitude as the integration of magnitude from J_{low} to J_{high}. The slope describes how the spectrum is attenuated as frequency increases, and the roughness describes how rough the spectrum is.

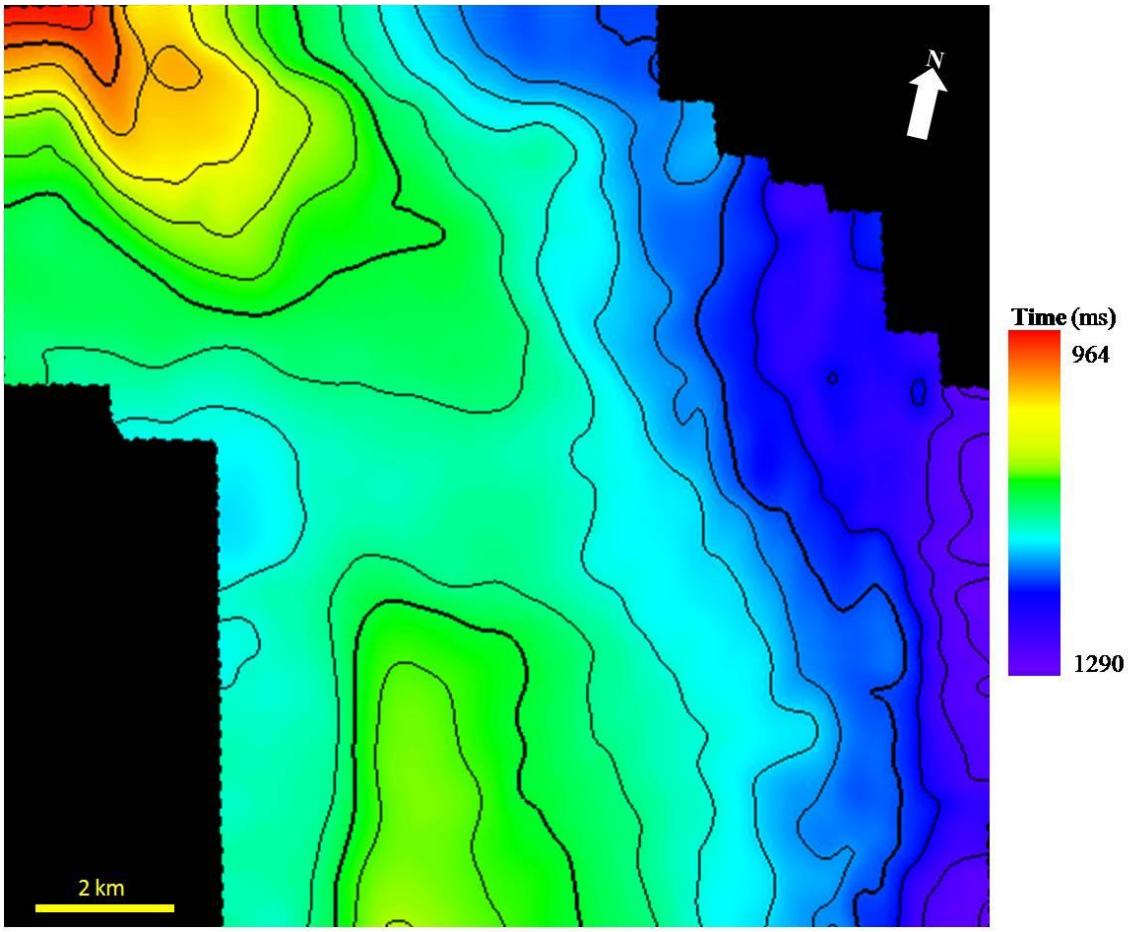

Figure 5-2. Time structure map of the picked Atoka unconformity.

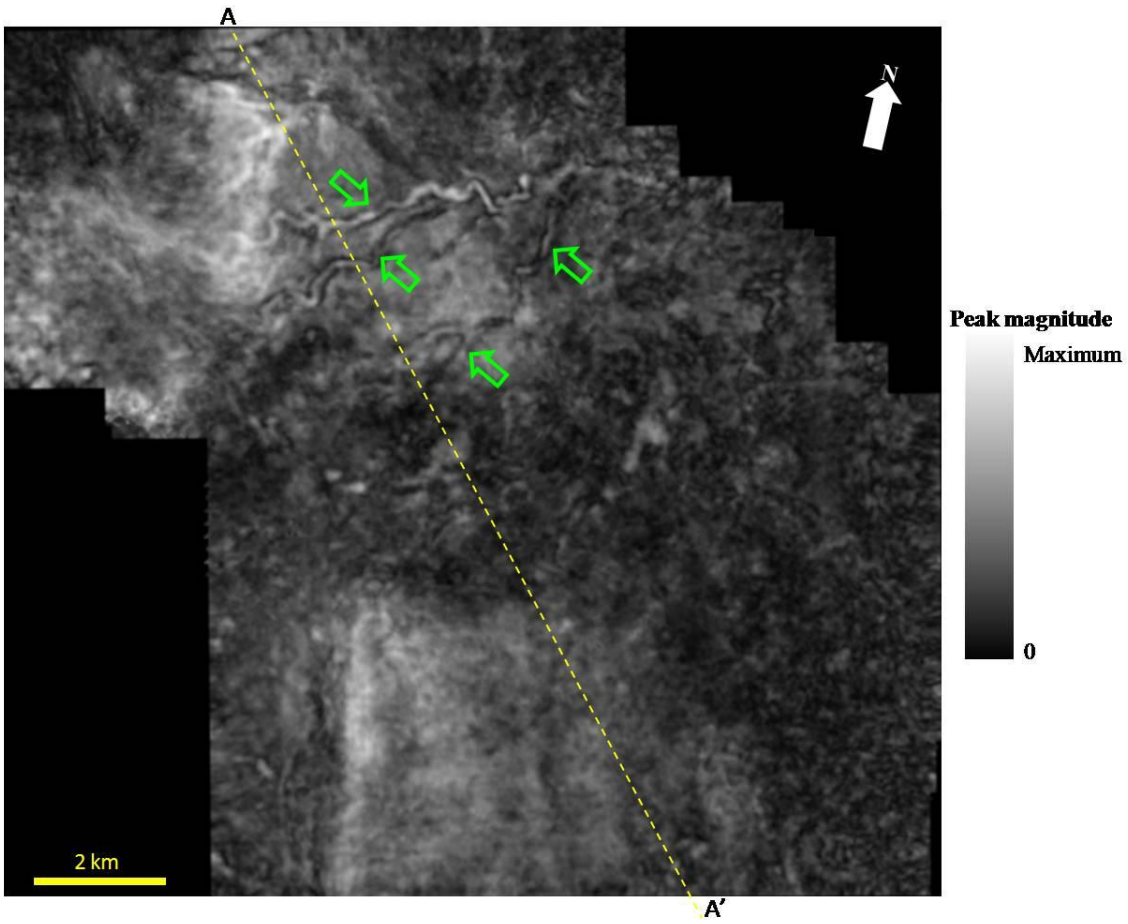

Figure 5-3. Phantom horizon slice 50 ms above the picked Atoka unconformity through peak magnitude from a survey acquired over the Central Basin Platform, west Texas, USA. Green arrows point to channels. Seismic line AA' is shown in Figure 5-6. (Seismic data courtesy of Burlington Resources)

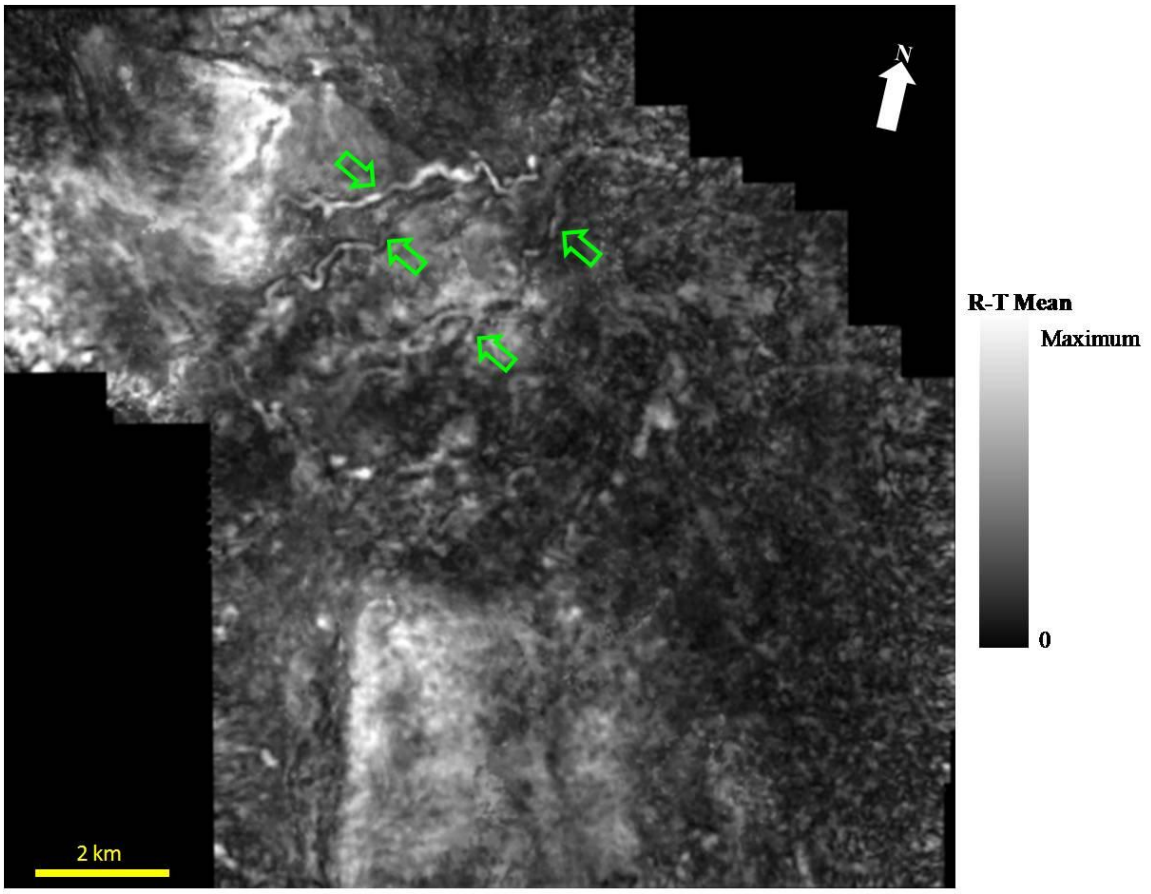

Figure 5-4. Phantom horizon slice 50 ms above the picked Atoka unconformity through R-T Mean magnitude comparable with peak magnitude in Figure 5-3. R-T Mean magnitude provides more clear delineation of channels than peak magnitude.

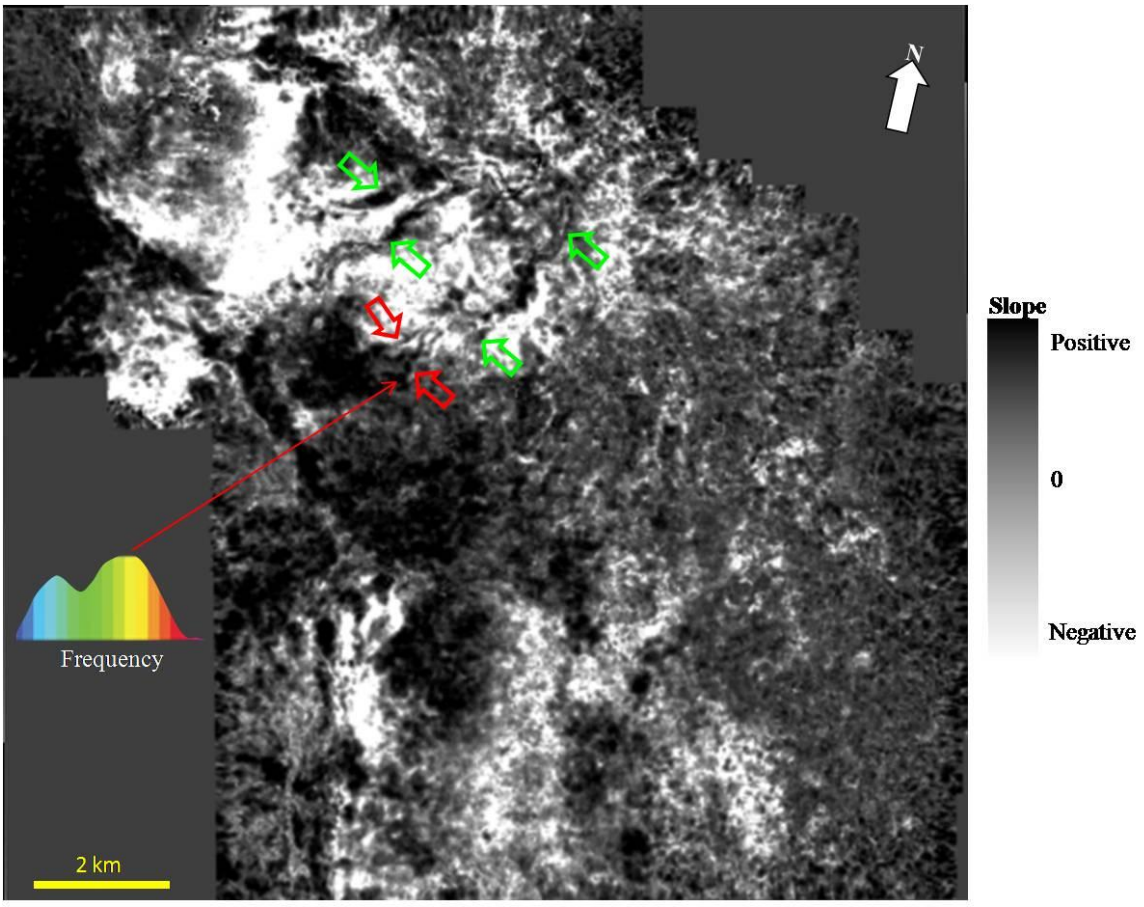

Figure 5-5. Phantom horizon slice 50 ms above the picked Atoka unconformity through spectral slope. Overall, the channel spectrum has a positive slope, while the non-channel spectrum has a negative slope. spectral slope gives some channel details complementary to peak magnitude and R-T Mean magnitude. Red arrows indicate two more channel branches.

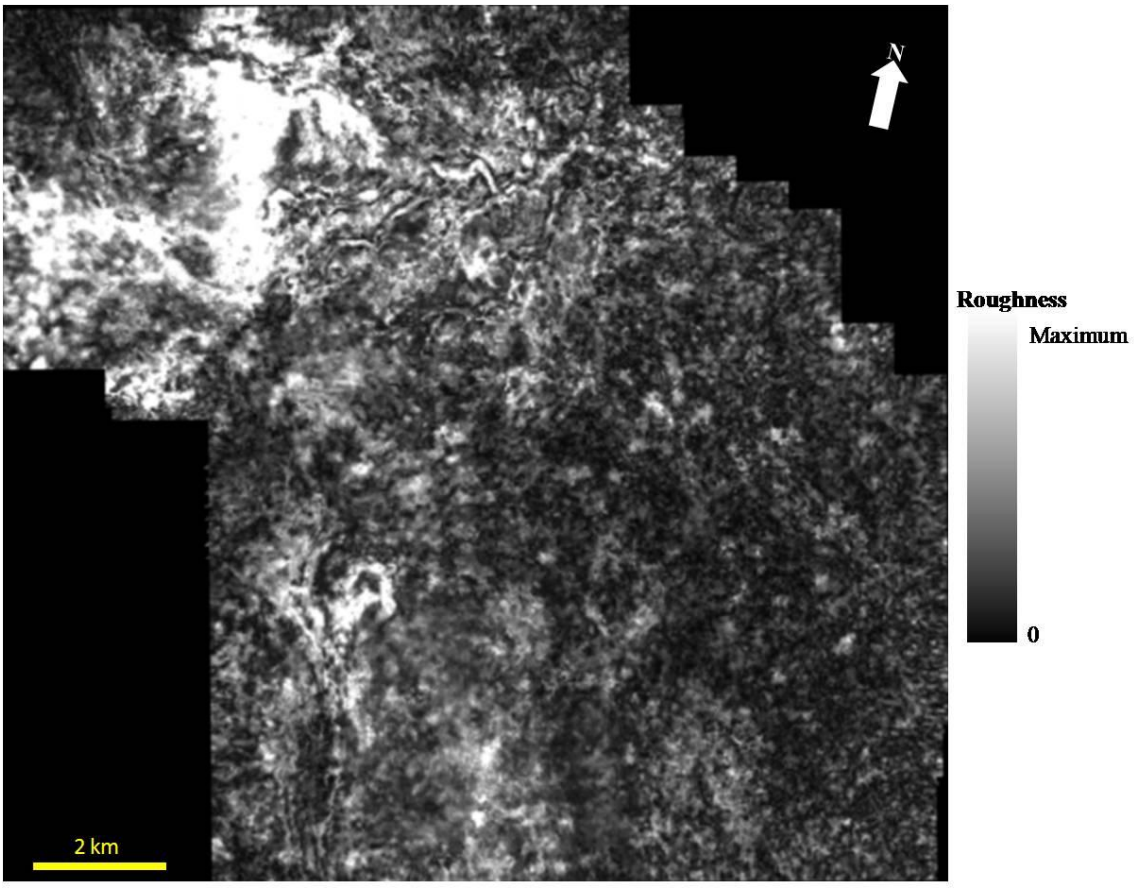

Figure 5-6. Phantom horizon slice 50 ms above the picked Atoka unconformity through spectral roughness. Spectral roughness also provides some channel details complementary to peak magnitude and R-T Mean magnitude.

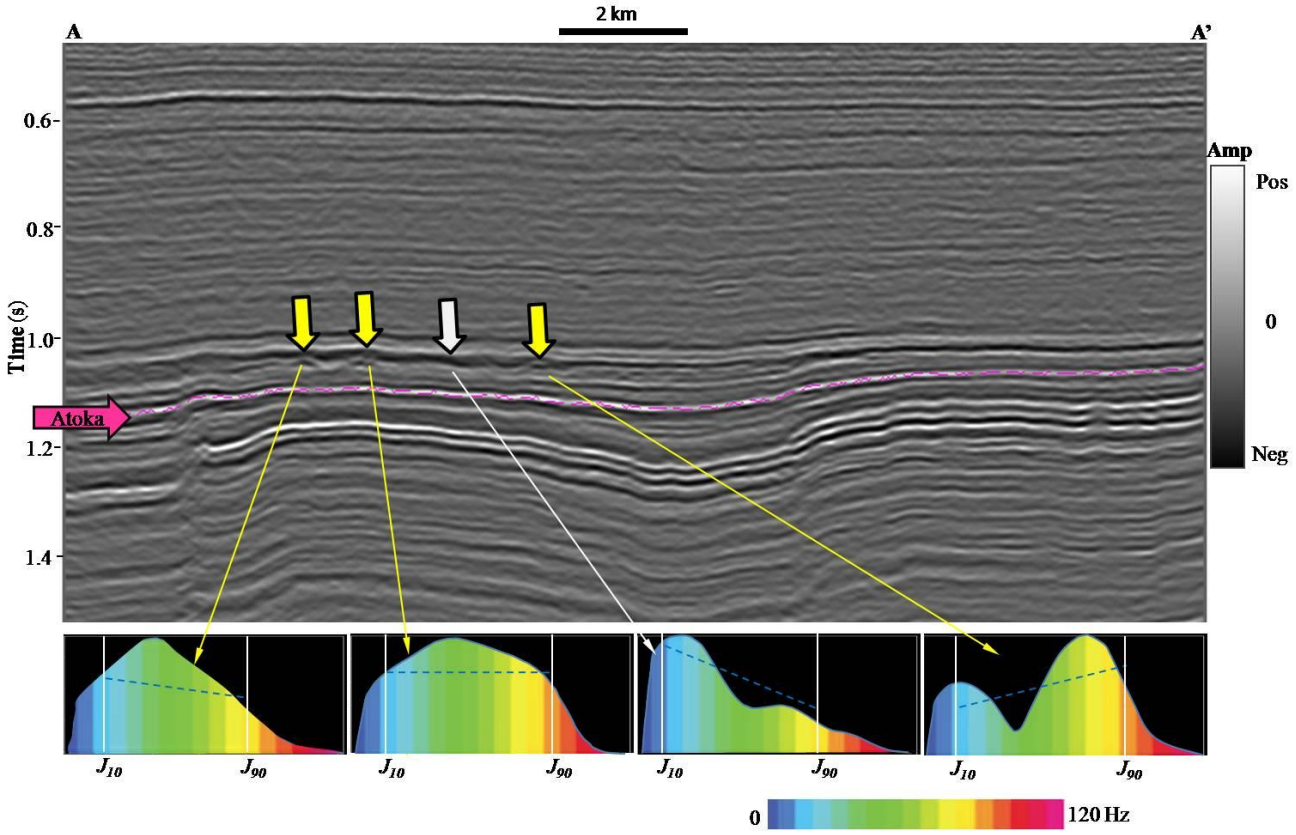

Figure 5-7. Seismic vertical window AA'. Yellow arrows indicate channels easily identified on the vertical slice through the seismic amplitude volume. White arrow indicates non-channel position. The spectra from the four spots tell us that, channel location corresponds to small negative, zero, or positive spectral slope, while the transition zone between channels has large negative slope. The spectral slope is calculated from percentile 10 to percentile 90, which we define as the bandwidth.

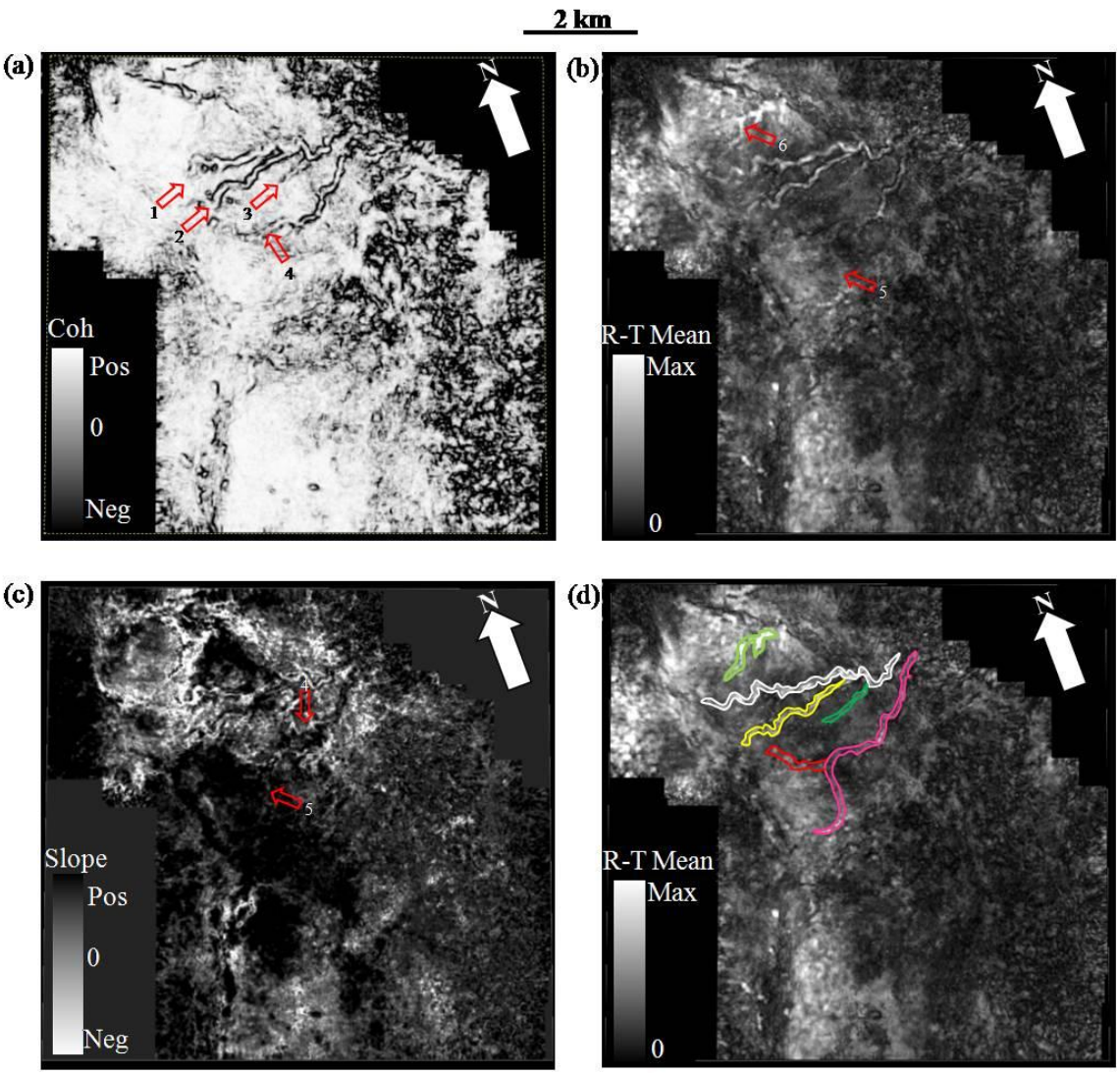

Figure 5-8. Phantom horizon slices 40 ms above Atoka unconformity through (a) coherence, (b) R-T Mean magnitude, and (c) spectral slope. (d) is the multichannel interpretation combing (a), (b), and (c). Channels 1 and 2 extend further towards southwest in (b) than in (a). Channels 5 and 6 are clearly delineated in (b), yet not visible in (a). Spectral slope also gives some details about channel distribution although it is noisy.

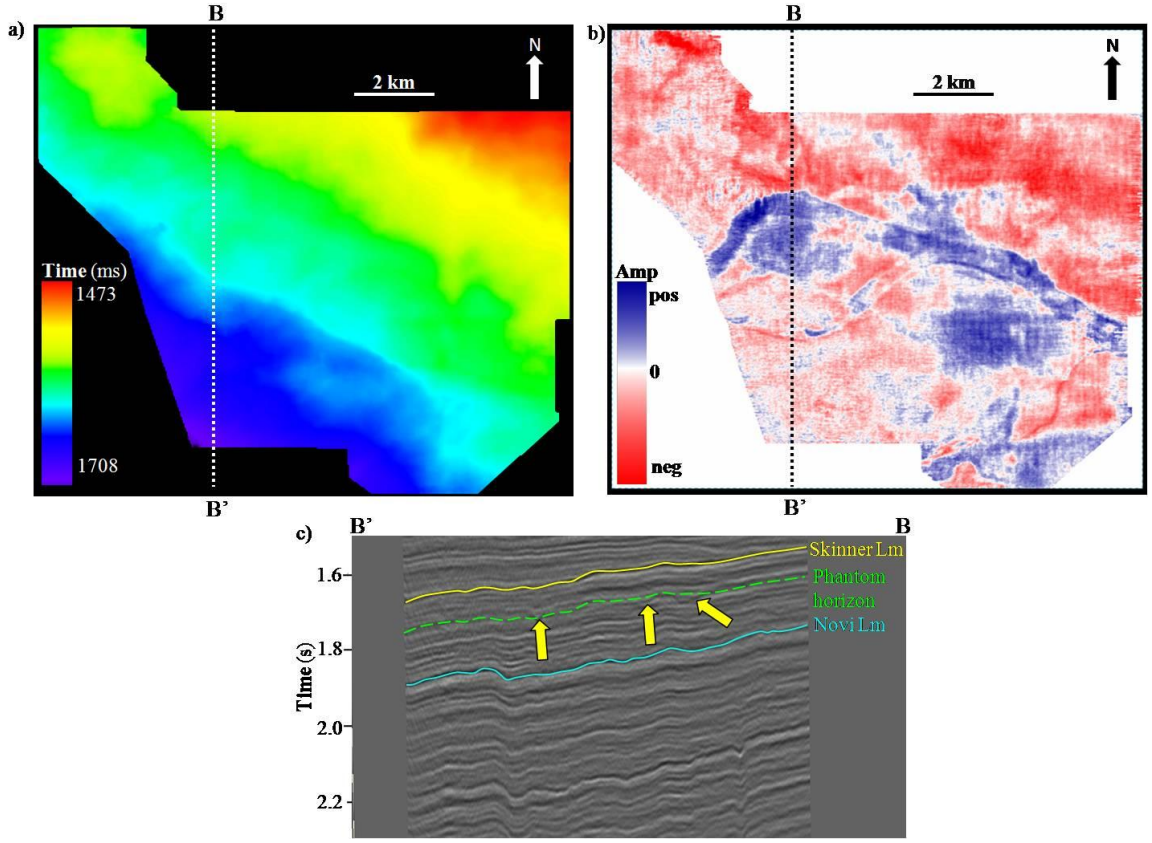

Figure 5-9. (a) Seismic time structure map through Skinner Lm from a merged survey acquired in the Anadarko Basin, (b) phantom horizon slice 60 ms below the Skinner Lm through amplitude at the Red Fork level, and (c) vertical seismic amplitude slice BB'. Yellow arrows indicate incised valley. Note that some data are contaminated by acquisition footprint. (Data courtesy of Chesapeake Energy)

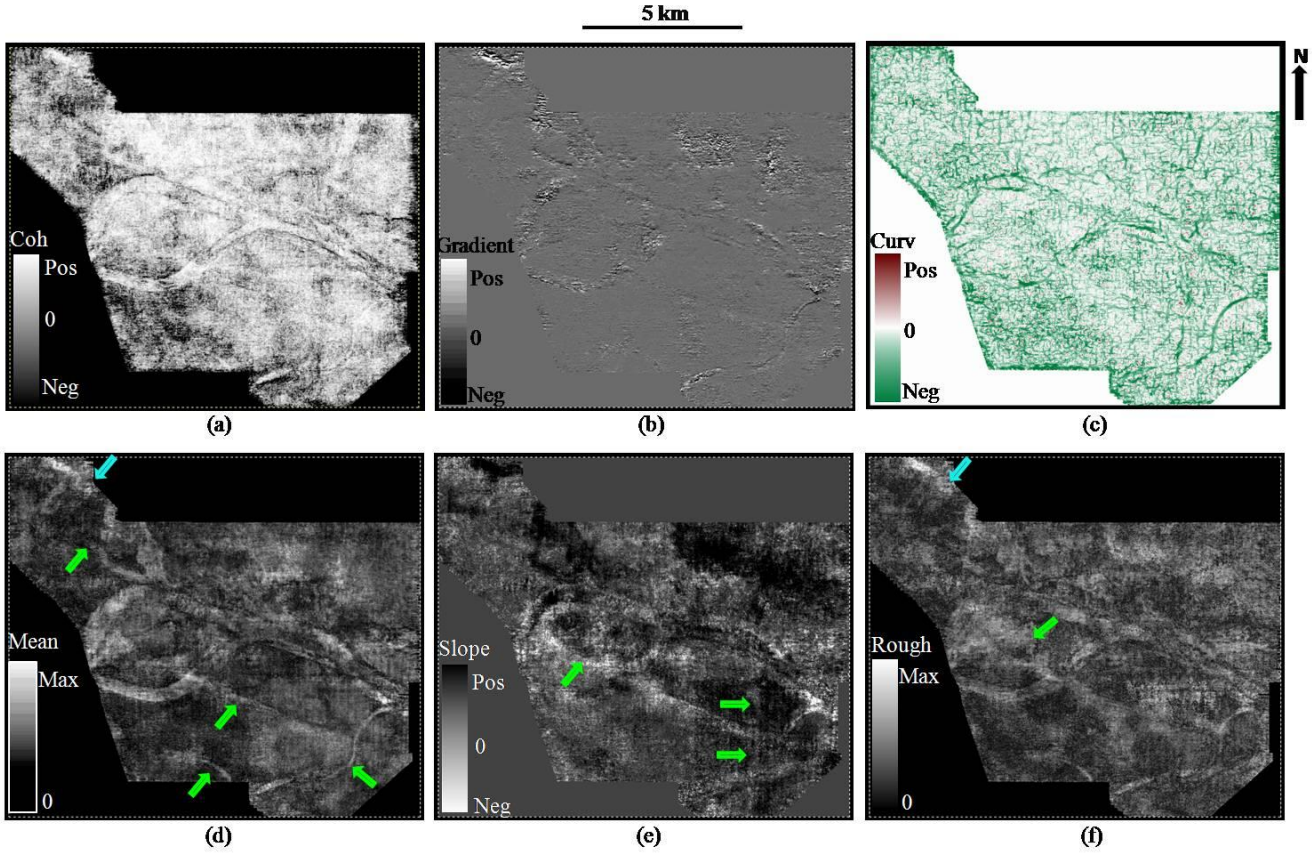

Figure 5-10. Phantom horizon slices 60 ms below the Skinner Lm at the Red Fork level through (a) coherence, (b) crossline energy gradient, (c) most negative curvature, (d) R-T mean magnitude, (e) spectral slope, and (f) roughness. Note that R-T Mean magnitude, spectral roughness, and slope show lots of details complementary to the edge-sensitive attributes (a)-(c).

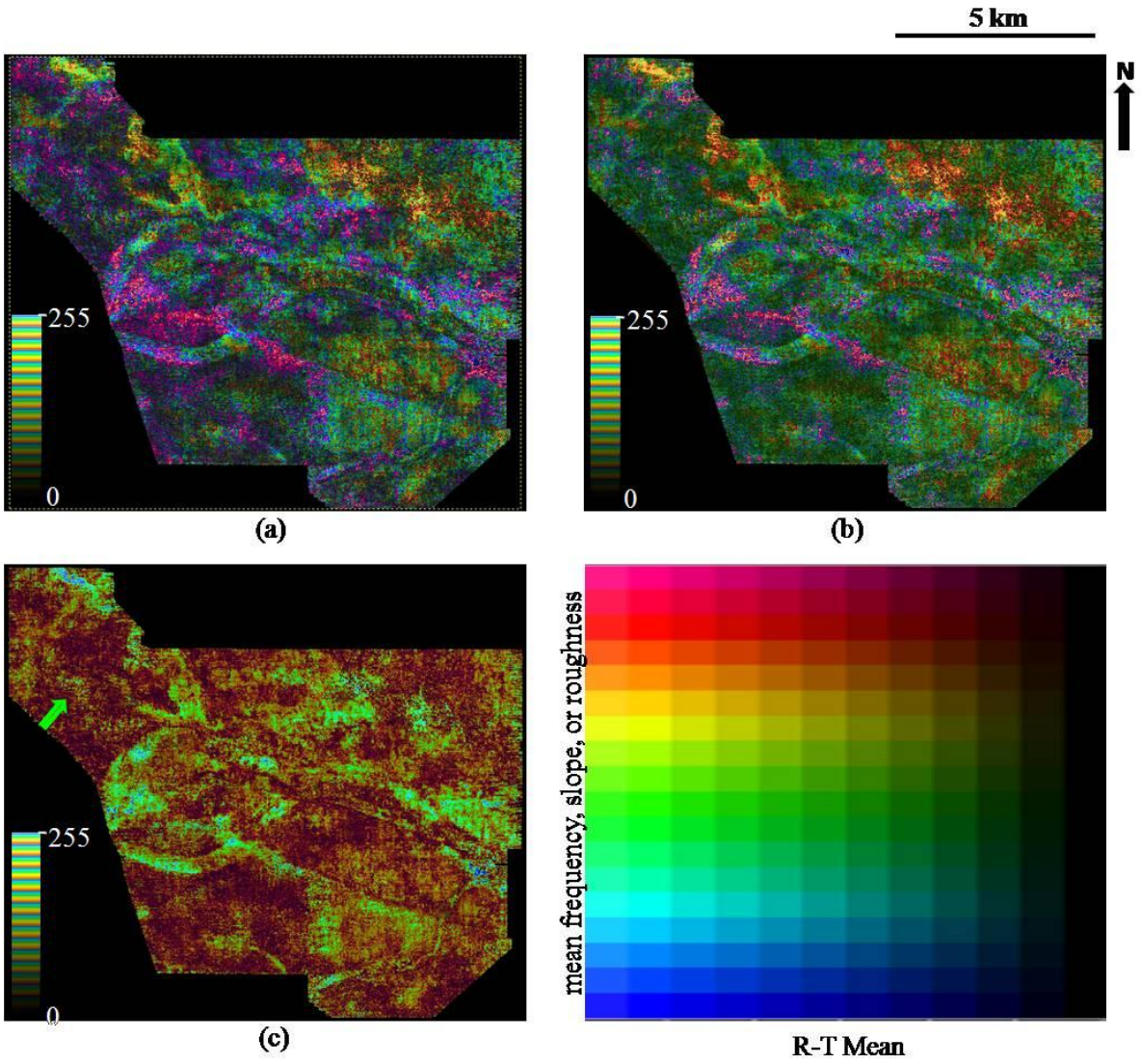

Figure 5-11. Phantom horizon slices 60 ms below the Skinner Lm at the Red Fork level through blended images (a) mean frequency with R-T Mean magnitude, (b) spectral slope with R-T Mean magnitude, and (c) spectral roughness with R-T Mean magnitude. The channel pointed by green arrow in (c) is not discernable in other maps.

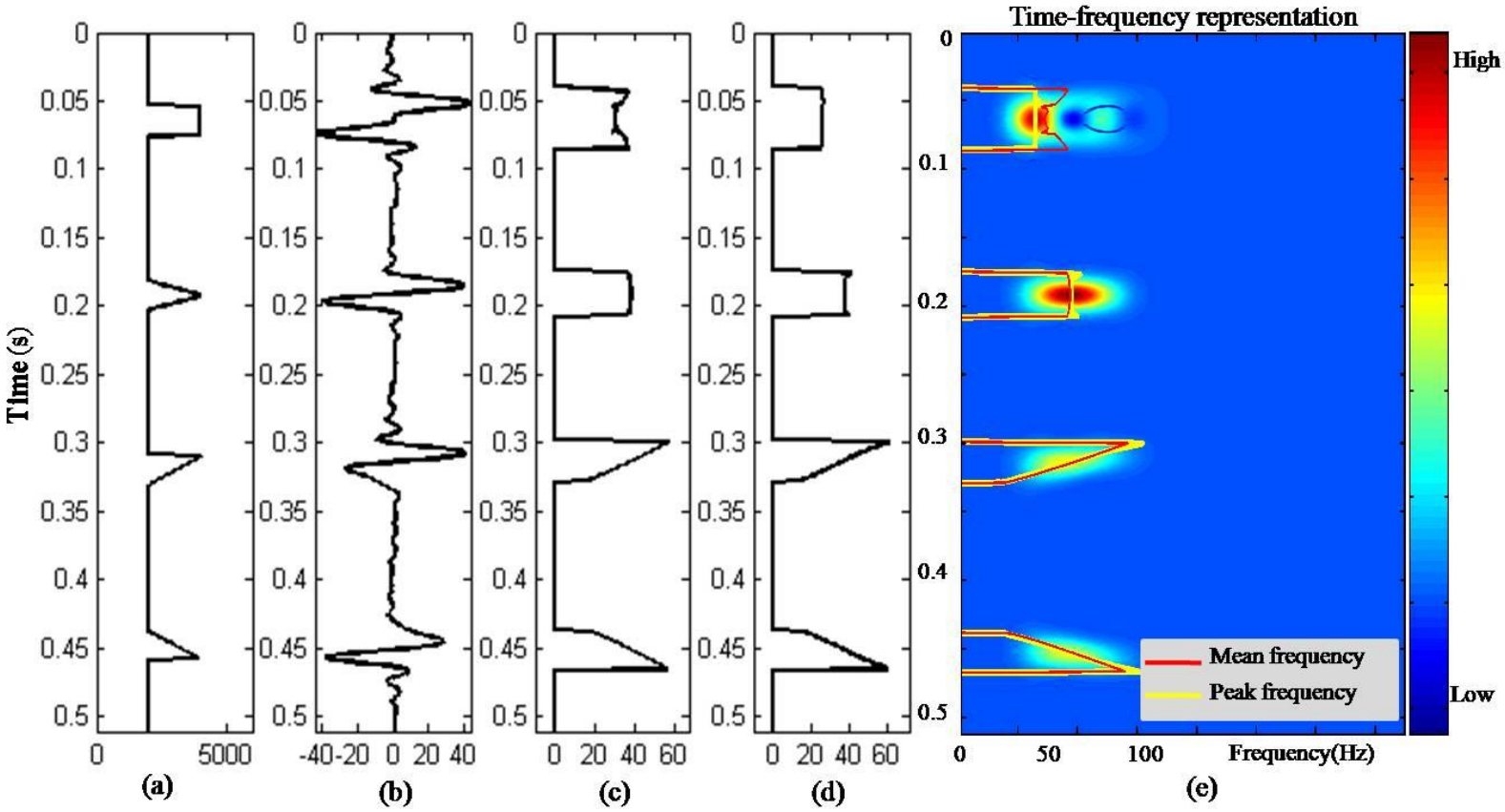

Figure 5-12. Sequence stratigraphic models (a), their seismic responses (b), mean frequency (c), and peak frequency (d) extracted from time-frequency representation (e). Notice that mean frequency and peak frequency map associated sequence models quite well.

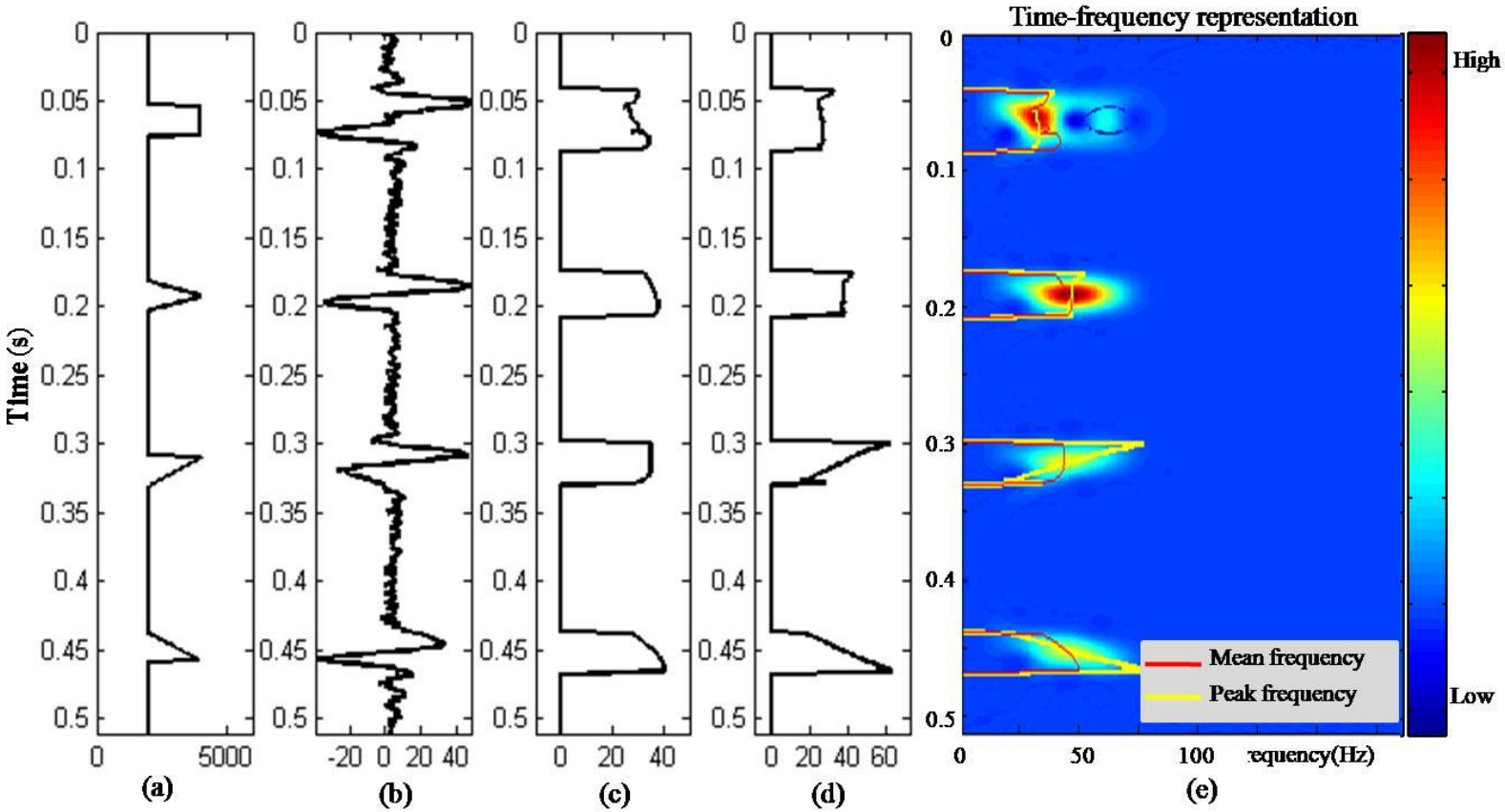

Figure 5-13. Same acoustic impedance models with Figure 5-12 (a), their seismic responses plus 20% random noise (b), mean frequency (c), and peak frequency (d) extracted from time-frequency representation (e). Peak frequency still maps sequence models quite well, while mean frequency does not map egg-shaped and upward coarsening models well.

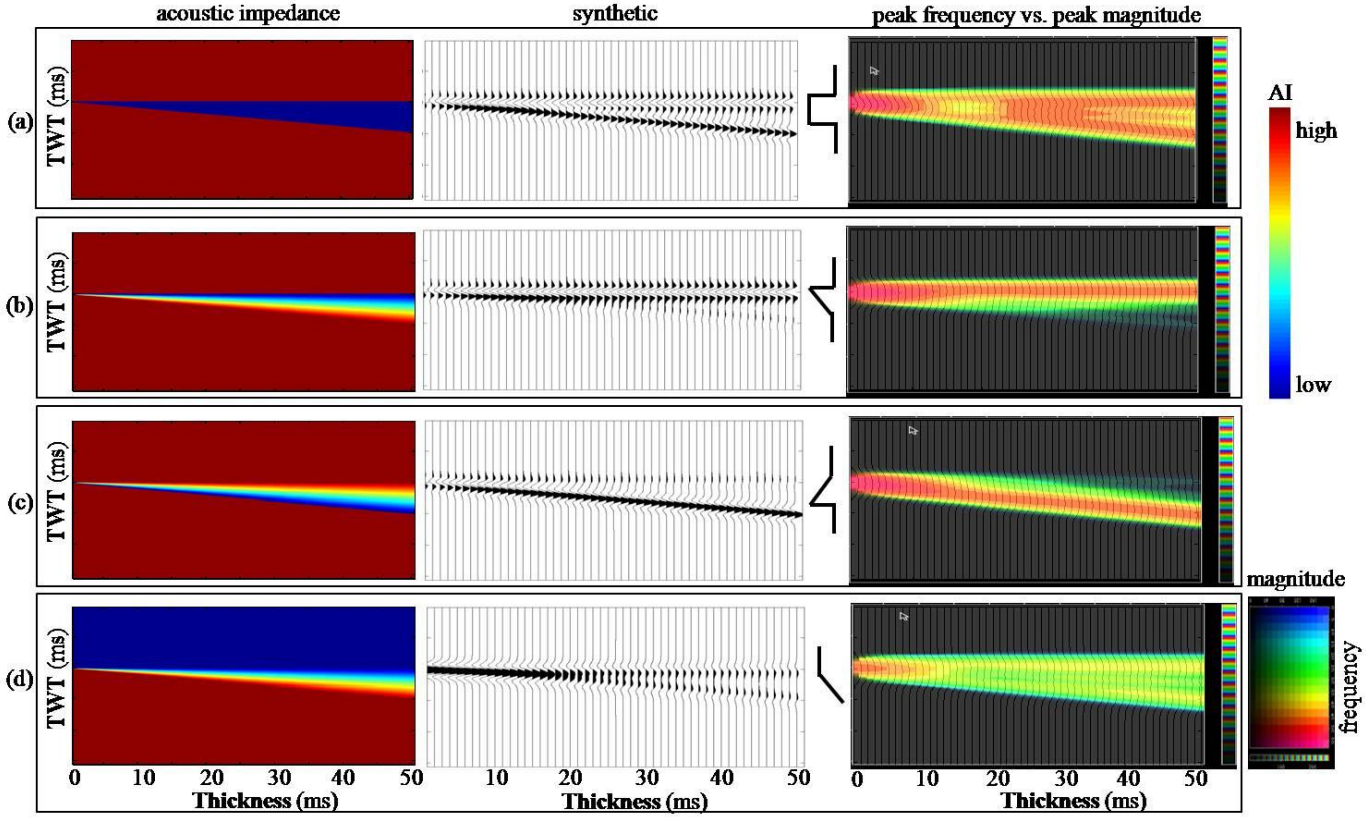

Figure 5-14. Acoustic impedance, synthetic, and the co-rendered image from peak frequency and peak magnitude of wedge models (a) blocky pattern, (b) upward coarsening gradational pattern, (c) upward fining gradational pattern, and (d) gradational pattern with gentle slope. The time thickness of these models ranges from 0 to 50 ms. We see peak frequency can be used to differentiate upward coarsening and upward fining patterns.

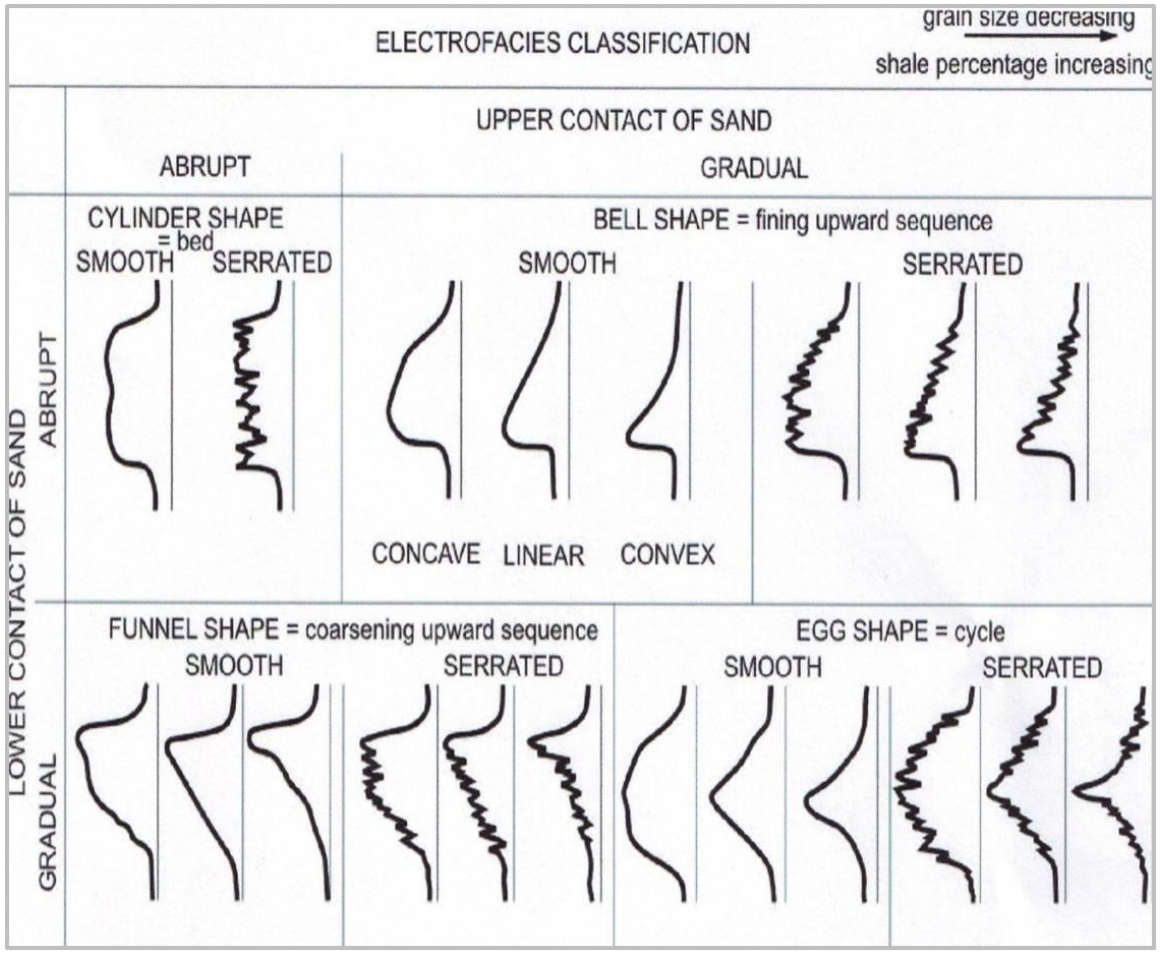

Figure 5-15. 20 stratigraphic models, representing different depositional processes.

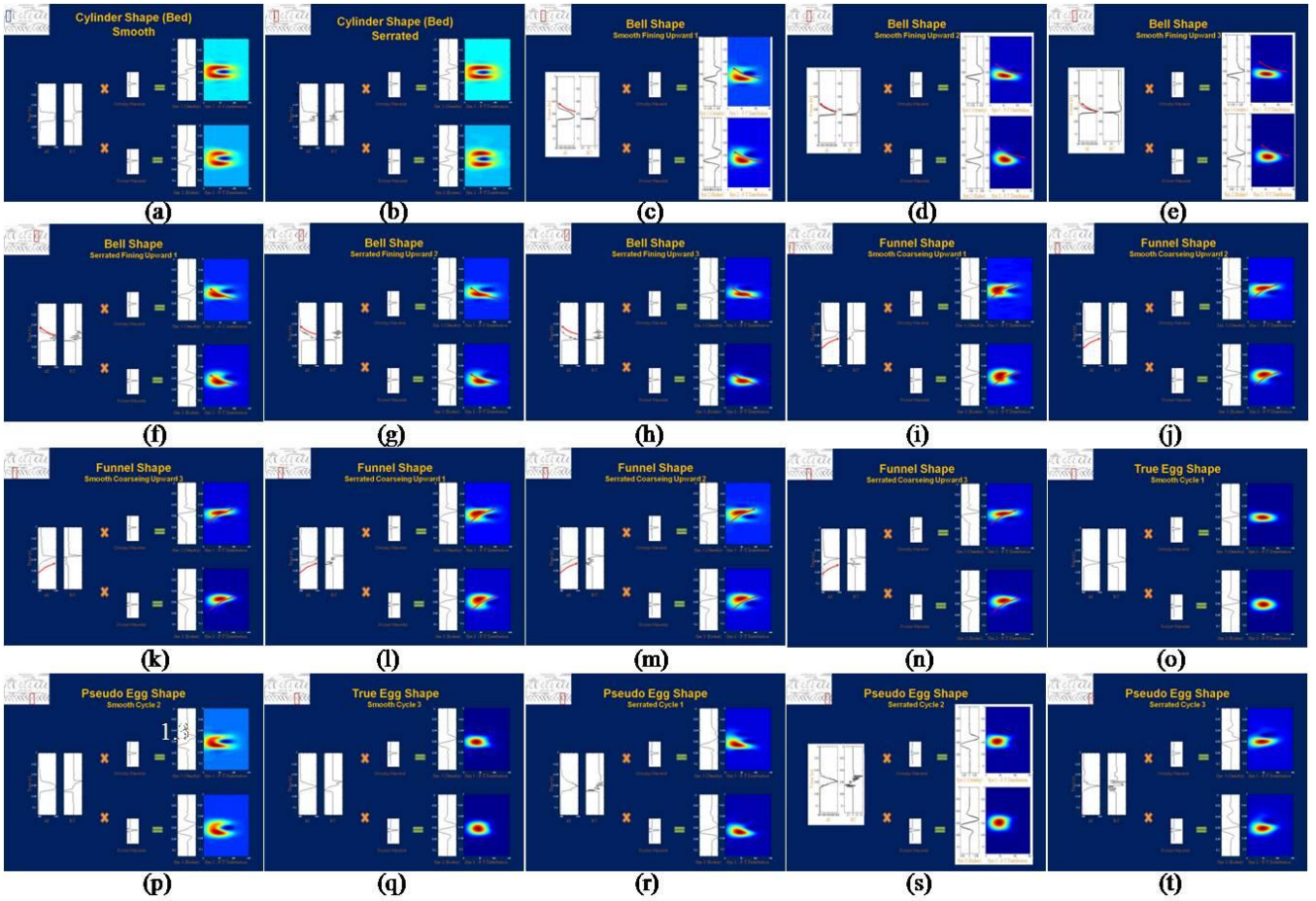

Figure 5-16. Acoustic impedance, synthetic, and time-frequency representation of the 20 stratigraphic models in Figure 5-15 from (a) to (t). Note that spectral shape reflects the stratigraphic patterns. (models generated by Alsahfy)

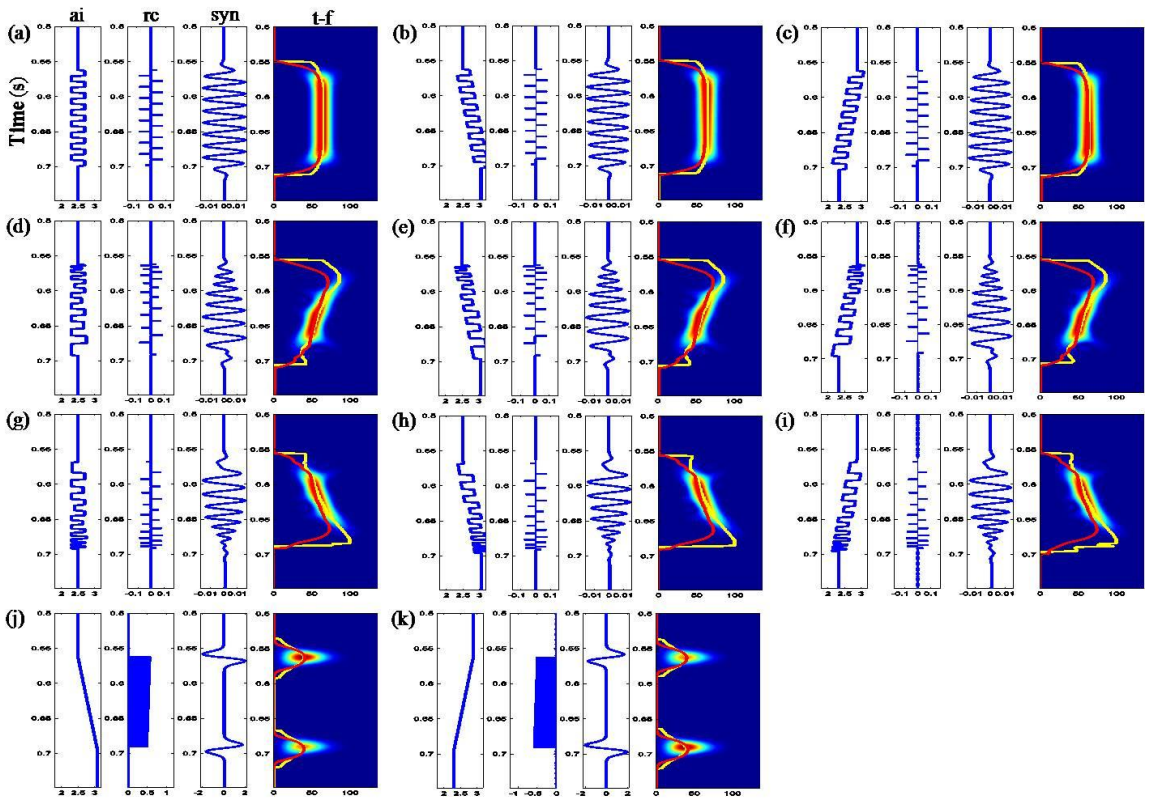

Figure 5-17. Sequence stratigraphic models with shale-sand interbeds (a)-(i) and linear velocity trend (j)-(k). For each model, acoustic impedance, reflection coefficient, synthetic, and time-frequency representation are displayed from left to right. Yellow and red curves indicate peak frequency and mean frequency respectively. We see that the pattern in time-frequency representation is majorly controlled by shale-sand interbeds rather than low frequency linear velocity change.

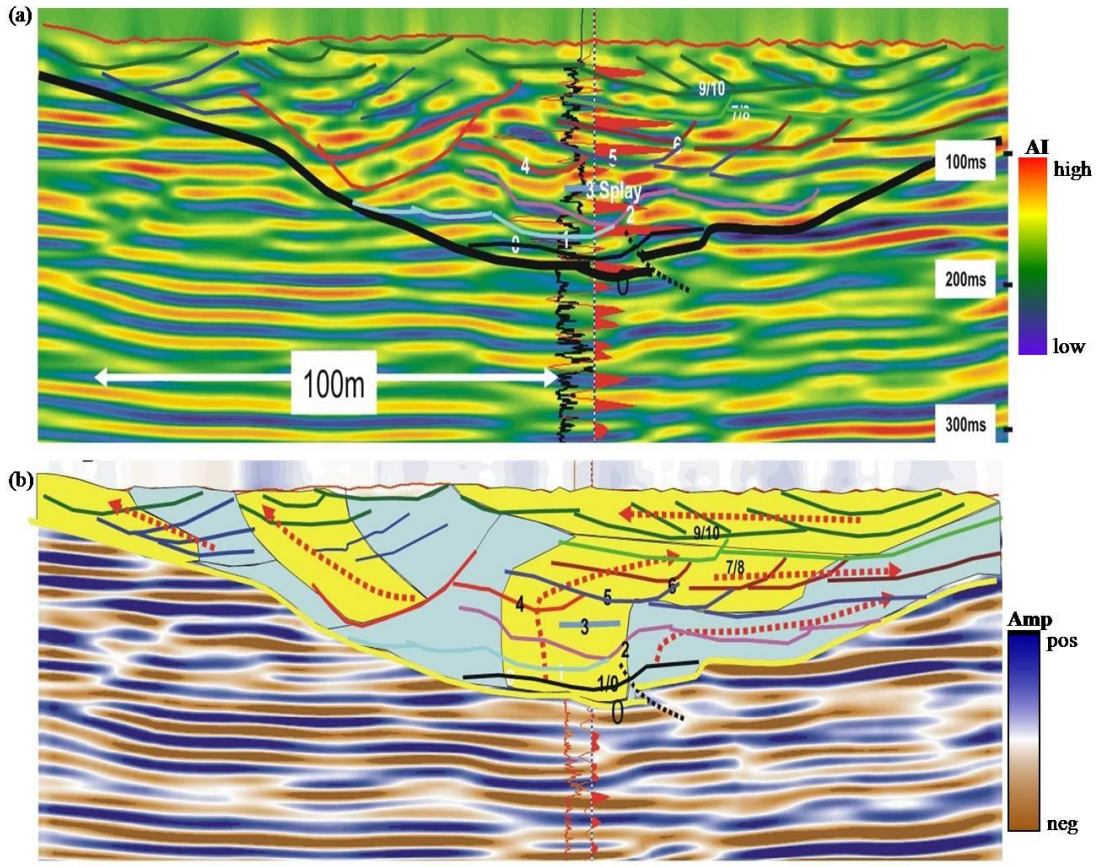

Figure 5-18. (a) Relative acoustic impedance section across Spine 1 and Gamma Ray log of well CSM #61. (b) Interpreted seismic section. Numbers represent channel sandstones. Yellow is channel sandstone and light blue is internal levee. Dotted arrows are gradational and lateral migration trends of channel sandstones.

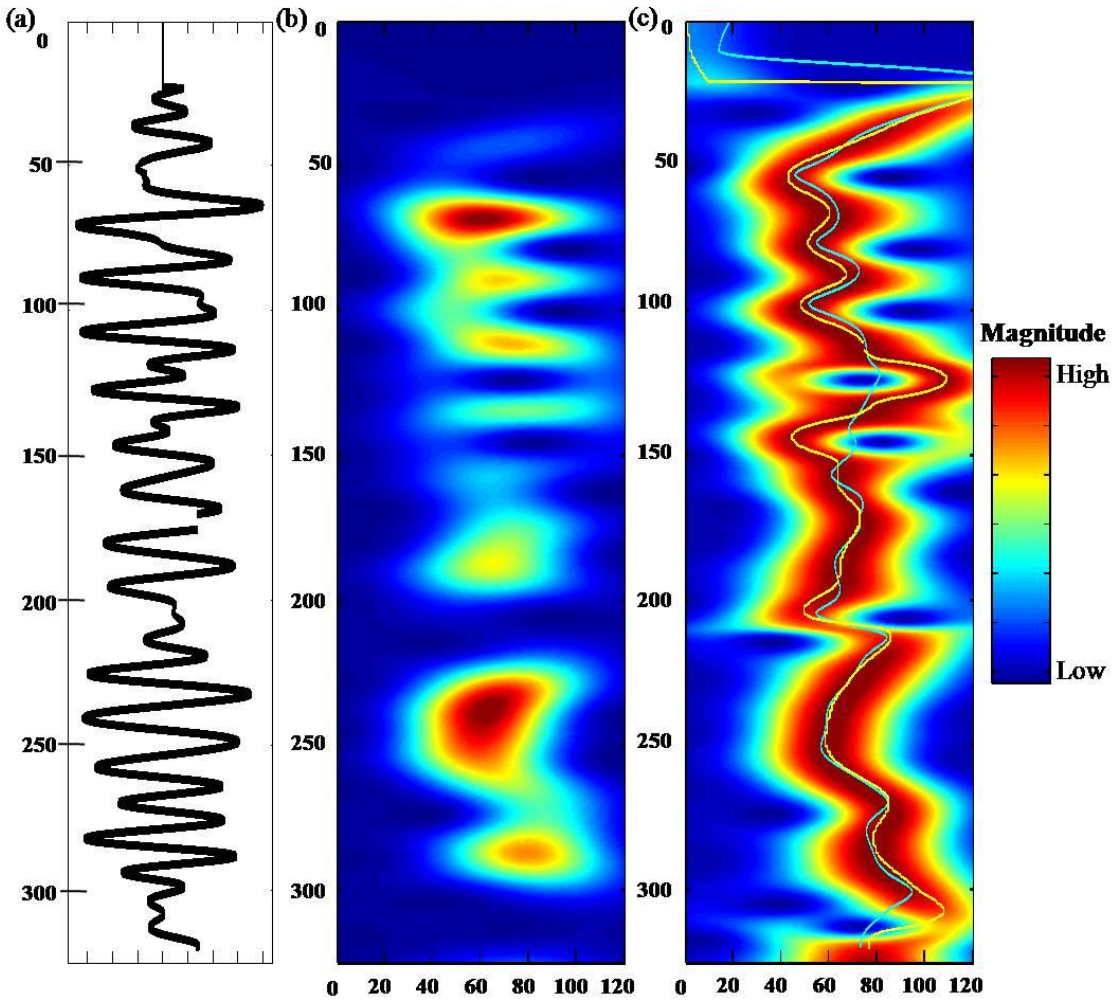

Figure 5-19. (a) Seismic trace from the location of the well, (b) spectral decomposition result, and (c) normalization image from (b). Yellow and cyan curves indicate peak frequency and mean frequency respectively.

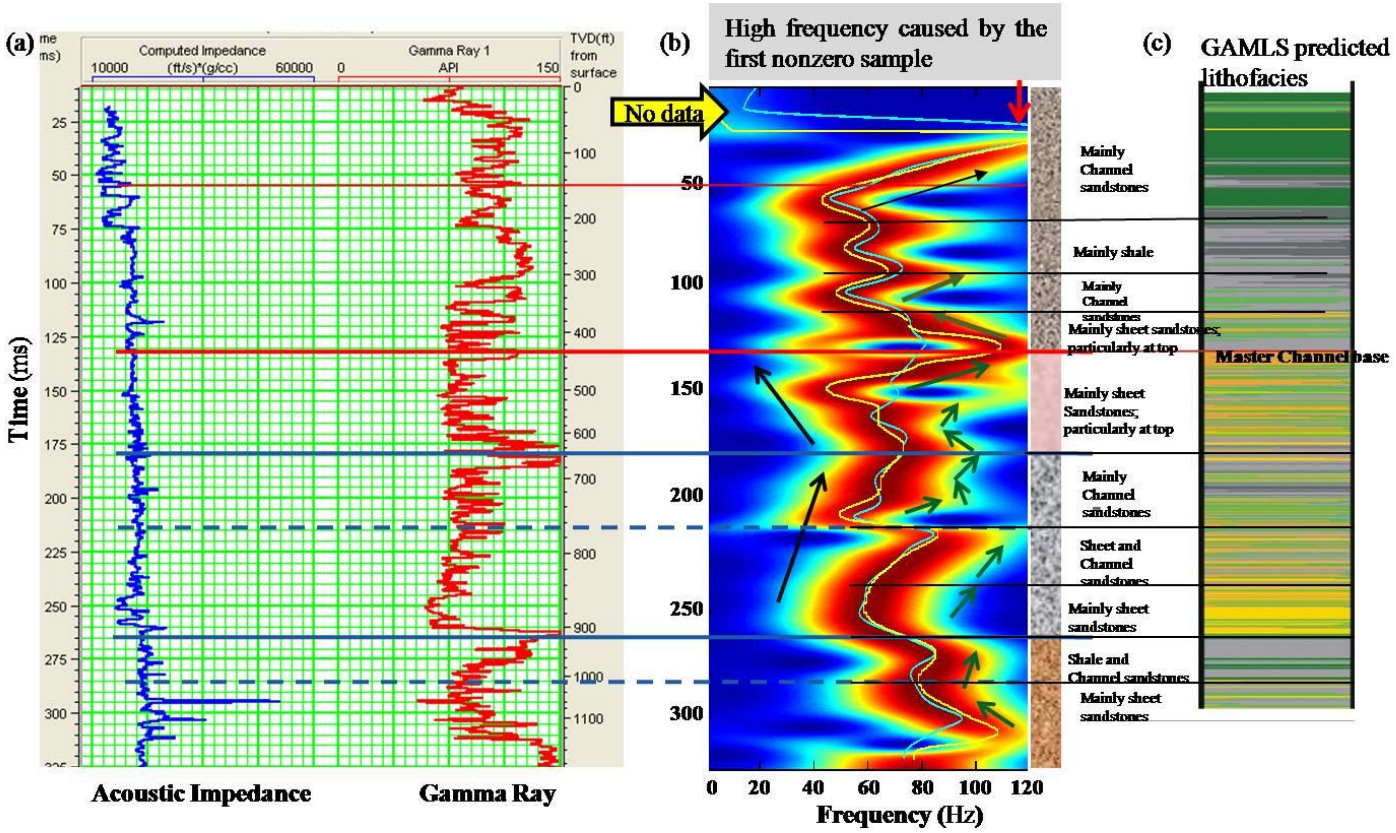

Figure 5-20. (a) Acoustic impedance and Gamma Ray (GR) logs, (b) sequence interpretation result using spectral decomposition, and (c) GAMLS predicted lithofacies. The black arrows, and dark green ones are interpreted results. Notice the good correlation between peak frequency, mean frequency and GR. Also notice that the interpreted stratigraphic sequences are verified by GAMLS predicted lithofacies.

References

Blumentritt, C. H., 2008, Highlight volumes: Reduce the burden in interpreting spectral decomposition data: The Leading Edge, **27**, 330-333.

Castagana, J. P., S. Sun, and R. W. Siegfried, 2003, Instantaneous spectral analysis: Detection of low-frequency shadows associated with hydrocarbons. The Leading Edge, **22**, 120-127.

Guo, H., K. J. Marfurt, and J. Liu, 2006, Principle component analysis of spectral components: 74th Annual International Meeting, SEG, Expanded Abstracts, 988-992.

Hart, B., 2008, Stratigraphically significant attributes: The Leading Edge, **27**, 320-324.

Li, H., W. Zhao, H., Cao, F. Yao, and L. Shao, 2006, Measures of scale based on the wavelet scalogram with application to seismic attenuation: Geophysics, **71**, 111-118.

Liu, J., 2006, Spectral decomposition and its application in mapping stratigraphy and hydrocarbons: Ph.D. thesis, University of Houston.

Liu, J., and K. J. Marfurt, 2005, Matching pursuit decomposition using Morlet wavelets: 75th Annual International Meeting, SEG, Expanded Abstracts, 786-789.

Liu, J., and K. J. Marfurt, 2007, Instantaneous spectral attributes to detect channels: Geophysics, **72**, 23–31.

Maklad, M. S., and J. K. Dirstein, 2007, Spectral detection of attenuation and lithology: CSPG CSEG Convention, 501-505.

Marfurt, K. J., and R. L. Kirlin, 2001, Narrow-band spectral analysis and thin-bed tuning: Geophysics, **66**, 1274-1283.

Matos, M. C., and R.S., Johann, 2007, Revealing geological features through seismic attributes extracted from the wavelet transform Teager-Kaiser energy: 77th Annual International Meeting, SEG, Expanded Abstracts, 1442-1446.

Partyka, G. A., J. Gridley, and J. Lopez, 1999, Interpretational applications of spectral decomposition in reservoir characterization: The leading Edge, **18**, 353-360.

Pearson, R. A., and B. S. Hart, 2004, Three-dimensional seismic attributes help define controls on reservoir development: Case study from the Red River Formation, Williston Basin: AAPG Memoir, **81**, 43-57.

Slatt, R. M., D. R. Pyles, J. Minken, A. J. Witton, S. K. Van Dyke, and R. A. Young, 2008, Scales of heterogeneity of an outcropping leveed-channel deepwater system, Cretaceous Dad Sabdstone Member, Lewis Shale, Wyoming: Atlas of deep-water outcrops, AAPG Studies in Geology, 56, 1-29.

Slatt, R. M., E. V. Eslinger, and K. Van Dyke, 2009, Acoustic and petrophysical properties of a clastic deepwater depositional system from lithofacies to archetectual element' scales: Geophysics, **74**, WA35-WA50.

Steeghs, P., and G. Drijkoningen, 2001, Seismic sequence analysis and attribute extraction using quadratic time-frequency representations: Geophysics, **66**, 1947-1959.

Suarez, Y., K. J. Marfurt, and M. Falk, 2008, seismic attribute-assisted interpretation of channel geometries and infill lithology: A case study of Anadarko Basin Red Fork channels: 78th Annual International Meeting, SEG, Expanded Abstracts, 963-967.

Tirado, S., 2004, Sand thickness estimation using spectral decomposition: MS Thesis, University of Oklahoma.

Zeng, H., and C. Kerans, 2003, Seismic frequency control on carbonate seismic stratigraphy: A case study of the Kingdom Abo sequence, west Texas: AAPG Bulletin, **87**, 273-293.

Zhang, K., K. J. Marfurt, and Y. Guo, 2008, Volumetric application of skewed spectra: 78th Annual International Meeting, SEG, Expanded Abstracts, 919-922.

Chapter 6: Conclusions

For reader's convenience, I summarize the conclusions of all Chapters:

Seismic azimuthal anisotropy analysis of post-hydraulic fracturing

I demonstrate that, the azimuthal anisotropic measures derived from model-based acoustic impedance provide insight into the induced fractures and stress field in the Barnett Shale. Acoustic impedance reduces the impact of seismic wavelet interference and thin-bed tuning effects, and broadens the spectrum through inclusion of frequency components from the wells, giving rise to improved vertical resolution within the Barnett Shale, providing results consistent with AVAz.

In the survey under study, the maximum horizontal stress is known to be northeast. The strike of anisotropy shows strong spatial variability but interesting "compartmentalization" with each compartment having the same strike of anisotropy. These compartments are strongly correlated to ridges and domes given by most positive principal curvature, implying that these structural highs either serve as fracture barrier or modify the local stress regime. Correlation of anisotropy measures to microseismic data suggests the existence of multiple azimuth directions in the fractured rocks, but fractures along a particular orientation still dominate.

Multi-linear regression or cluster analysis of anisotropy measures, curvature, and other effective attributes may yield a reliable characterization of induced-fractures and

by-passed pay, help us to understand the behavior of bashed and refractured vertical wells and better guide and stimulate horizontal wells.

Quantitative correlation of fluid flow to curvature lineaments

I develop a new workflow to quantitatively correlate the fracture-related curvature lineaments from different azimuths to the production data. This approach hypothesizes that, open natural fractures or closed fractures that are easily popped open by the hydraulic fracture program act as the dominant fluid conduits in the reservoir. Assuming one fracture composed of a set of point fluid injectors, I can predict the hypothesized fracture "fluid flow" from different azimuths through integration of the contribution from all point fluid injectors. Compared with the approach proposed by Nissen et al. (2009), the workflow avoids the intensive manual picking of the distance from the well to the nearest lineament. In addition, I consider the contribution of fluid flow from all rather than the nearest fracture lineaments around the well, which is more physically plausible.

I demonstrate that this workflow can be employed to investigate the fracture characteristics (open or sealed) by applying it to a carbonate Field in Kansas and a Woodford Shale survey in Arkoma Basin. I believe that such statistically significant correlations based on the workflow introduced in this paper can result in a more efficient drilling program.

Seismic attribute illumination of an igneous reservoir in China

Volcanic rocks in China, Argentina, and other parts of the world serve as hydrocarbon reservoirs. In other areas such volcanic features may be mistaken for carbonate buildups. It is my hope that by presenting images of an important producing volcanic reservoir in the context of seismic geomorphology, that our exploration colleagues can use it as a proven analogue. A prominent feature of the volcanic rocks is that they typically have strong amplitude in seismic response, such that amplitude-related attributes such as spectral magnitude and reflection strength provide effective means of mapping volcanics. Geometrical attributes including coherence, and curvature also provide convincing results by revealing conduits, the structure and texture of the surface of the igneous body, and also faults cutting into the igneous body. The next step is to evaluate the igneous reservoir properties measured in logs and analyze their correlation with seismic attributes.

Extension of spectral-decomposition into mapping stratigraphic patterns

I have demonstrated that statistical spectral attributes extracted from spectral-decomposition could be very useful to reveal subtle stratigraphic features. I find R-T Mean magnitude provides similar features to peak magnitude, but with better delineation of channels. By implementing based on percentile, R-T Mean magnitude, spectral slope, and spectral roughness provide a better representation of flattened spectra than standard deviation, skewness and kurtosis that are valid for nearly Gaussian spectra.

Spectral decomposition is sensitive to lateral and vertical stratigraphic heterogeneity. Using a suite of synthetic models and the real data acquired over an

outcrop originally deposited in deepwater suggests that peak frequency and mean frequency derived from the spectral decomposition volume are able to differentiate stratigraphic intervals with different vertical stacking arrangements. Spectral attributes extracted from spectral decomposition still suffers from wavelet interference effects between close-spaced reflections.

Seismic attributes have proven to be powerful in illuminating unconventional reservoirs. For unconventional reservoirs such as gas shale with poor matrix property in which induced or natural fractures provide key fluid conduits, geometric attributes like curvature and coherence and seismic measures based on azimuthal anisotropy analysis could be very instrumental to provide indications of those fractures. For those reservoirs with relatively good matrix property such as the volcanic reservoir under study, seismic attributes can assist us to map different architecture elements of the reservoir.

The future trends will require:

(1) combining two or more attributes by multi-attribute analysis, or cluster analysis, and powerful geobody visualization, allowing interpreters to yield a relatively reliable answer about the reservoir target.

(2) establishment of comprehensive workflow to correlate seismic attributes to ground truth mapped by drilling samples, core plugs, production, image logs, and microseismic in a quantitative fashion.